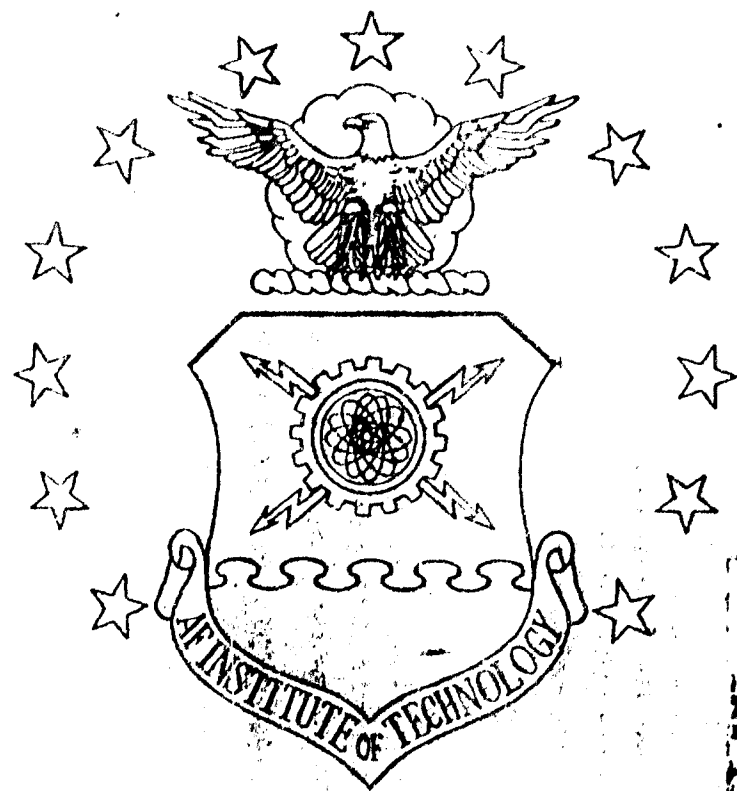


AFIC FILE COPY

(1)

AD-A230 544



INVESTIGATION OF DAMAGE MECHANISMS  
IN A CROSS-PLY METAL MATRIX  
COMPOSITE UNDER THERMO-MECHANICAL  
LOADING

THESIS

Joel J. Schubbe  
Captain, USAF

AFIT/GAE/ENY/90D-26

D

Best Available Copy

DEPARTMENT OF THE AIR FORCE  
AIR UNIVERSITY  
AIR FORCE INSTITUTE OF TECHNOLOGY

Wright-Patterson Air Force Base, Ohio

01 1 3 079

AFIT/GAE/ENY/90D-26

0

INVESTIGATION OF DAMAGE MECHANISMS  
IN A CROSS-PLY METAL MATRIX  
COMPOSITE UNDER THERMO-MECHANICAL  
LOADING

THESIS

Joel J. Schubbe  
Captain, USAF

AFIT/GAE/ENY/90D-26

DTIC  
ELECTE  
JAN 07 1991  
S B D

APPROVED FOR PUBLIC RELEASE; DISTRIBUTION UNLIMITED

AFIT/GAE/ENY/90D-26

**INVESTIGATION OF DAMAGE MECHANISMS  
IN A CROSS-PLY METAL MATRIX  
COMPOSITE UNDER THERMO-MECHANICAL  
LOADING**

**THESIS**

Presented to the Faculty of the School of Engineering  
of the Air Force Institute of Technology  
Air University  
In Partial Fulfillment of the  
Requirement for the Degree of  
Master of Science in Aeronautical Engineering

Joel J. Schubbe

Captain, USAF

December 1990

APPROVED FOR PUBLIC RELEASE; DISTRIBUTION UNLIMITED

### Preface

The primary purpose of this thesis was to further the characterization of a new metal matrix composite. This task could not have been accomplished without the help of a great many Scientists and Technicians. I would like to thank specifically Mr. Jay Anderson and the other technicians in the AFIT A-A Lab for their help with equipment modifications and supplies. I am also indebted to the WRDC Materials Laboratory for training in specimen preparation, examination, and photography (optical and SEM).

I would like to thank my thesis advisor, Dr. Shankar Mall, for all the help and advice he has provided throughout the duration of experimentation and analysis. Appreciation also goes out to Mr. Ted Fecke of the Propulsion Laboratory for sponsorship of the research endeavor.

Lastly, but most importantly, I would like to thank my wife Sherry and my son Jonathan for their patience and support during my 18 month "absence."

Joel J. Schubbe

Accession For	
NTIS GRA&I	<input checked="" type="checkbox"/>
DTIC TAB	<input type="checkbox"/>
Unannounced	<input type="checkbox"/>
Justification	
By _____	
Distribution/ _____	
Availability Codes	
Dist	Avail and/or special
A-1	



## Table of Contents

Preface . . . . .	ii
List of Figures . . . . .	v
List of Tables . . . . .	x
Abstract . . . . .	xi
I. Introduction . . . . .	1
A. Problem Definition . . . . .	1
II. Background . . . . .	9
A. Thermal and Thermo-Mechanical Fatigue of MMCs	9
B. Recent Advances - Metal Matrix Composite	
Testing . . . . .	13
C. METCAN - Metal Matrix Composite Analyzer . . .	18
III. Experimental Equipment/Procedure . . . . .	24
A. General Discussion . . . . .	24
B. Test Components . . . . .	25
i. Computer Control . . . . .	25
ii. Mechanical Components . . . . .	27
iii. Thermal Components . . . . .	29
iv. Strain Measurement Components . . . . .	37
v. Specimen and Specimen Preparation . . . .	39
IV. Results and Discussion . . . . .	52
A. Test Results Summary . . . . .	52
B. Thermal Strain and CTE Test . . . . .	58
C. Strain Measurements . . . . .	61
D. Young's Modulus Measurements . . . . .	71
E. Fracture Analysis . . . . .	76
V. Analysis . . . . .	99
A. Fatigue Life Governing Factors . . . . .	99
B. Cumulative Damage Models . . . . .	102
VI. Conclusions and Recommendations . . . . .	112
Appendix A - Constituent Microstress Data From METCAN .	115

<b>Appendix B - Stress/Temperature vs. Time Profiles . . .</b>	<b>135</b>
<b>Appendix C - Additional Data . . . . . . . . . . . . . . . . . .</b>	<b>138</b>
<b>Bibliography .</b>	<b>145</b>
<b>Vita .</b>	<b>148</b>

## List of Figures

	Page
Figure 1. Typical Flight Component Temp/Load Profiles	2
Figure 2. CTE Mismatch Representative Microstresses	4
Figure 3. Temperature/Load Profiles	11
Figure 4. Multi-Cell Model	19
Figure 5. Test System Block Diagram	26
Figure 6. Computer-controlled Test System	28
Figure 7. Mechanical Loading System	30
Figure 8. Thermal Control System	31
Figure 9. Air Line Schematic	34
Figure 10. PID Control System for Micricon 82300	36
Figure 11. Water Cooling System	38
Figure 12. Strain Measurement System	40
Figure 13. Water Injection vs. Diamond Machining	44
Figure 14. Uncycled Specimen Edge	45
Figure 15. Replica Photos of Specimen after Thermal Cycles	46
Figure 16. Edge Damage Schematic (After Preparation before Tf)	47
Figure 17. MMC Specimen	48
Figure 18. Experimental Test Matrix	53

<b>Figure 19. Tensile Test Stress-Strain Curves . . . . .</b>	<b>54</b>
<b>Figure 20. IP and OP Fatigue Life (0.02 Hz - 149-427°C) . . . . .</b>	<b>57</b>
<b>Figure 21. Edge Damage Summary . . . . .</b>	<b>62</b>
<b>Figure 22. Strain Stabilization for 441 MPa In-Phase Test . . . . .</b>	<b>63</b>
<b>Figure 23. Strain Stabilization 441 MPa Out-of-Phase Test . . . . .</b>	<b>64</b>
<b>Figure 24. Strain Data for 367 MPa Out-of-Phase Test . . . . .</b>	<b>67</b>
<b>Figure 25. Strain Data for 441 MPa In-Phase Test . . . . .</b>	<b>68</b>
<b>Figure 26. Strain Data for 441 MPa Out-of-Phase Test . . . . .</b>	<b>69</b>
<b>Figure 27. Strain Data for 612 MPa In-Phase Test . . . . .</b>	<b>70</b>
<b>Figure 28. Strain Data for 612 MPa Out-of-Phase Test . . . . .</b>	<b>71</b>
<b>Figure 29. Modulus Data for 367 MPa In-Phase Test . . . . .</b>	<b>75</b>
<b>Figure 30. Modulus Data for 367 MPa Out-of-Phase Test . . . . .</b>	<b>76</b>
<b>Figure 31. Modulus Data for 441 MPa In-Phase Test . . . . .</b>	<b>77</b>
<b>Figure 32. Modulus Data for 441 MPa Out-of-Phase Test . . . . .</b>	<b>78</b>
<b>Figure 33. Modulus Data for 612 MPa In-Phase Test . . . . .</b>	<b>79</b>
<b>Figure 34. Modulus Data for 612 MPa Out-of-Phase Test . . . . .</b>	<b>80</b>
<b>Figure 35. SEM Sectioning Schematic . . . . .</b>	<b>81</b>
<b>Figure 36. Reaction Zone Sizing . . . . .</b>	<b>82</b>
<b>Figure 37. Reaction Zone at 180 Cycles . . . . .</b>	<b>83</b>
<b>Figure 38. Reaction Zone at 28,900 Cycles . . . . .</b>	<b>84</b>
<b>Figure 39. Interface Crack Deflection . . . . .</b>	<b>85</b>
<b>Figure 40. High Load Test Reaction Zone Without Crack . . . . .</b>	<b>86</b>
<b>Figure 41. High Load Test Reaction Zone With Incoming Crack . . . . .</b>	<b>87</b>

Figure 42. Low Load Test Reaction Zone - Incoming Crack	88
Figure 43. Medium Load Test Reaction Zone With Incoming Crack	89
Figure 44. Fracture Surface Spectrum	90
Figure 45. Fracture Surfaces - 367 MPa I-P (TOP):367 MPa O-P (BOTTOM)	91
Figure 46. Fracture Surfaces - 441 MPa I-P (TOP):441 MPa O-P (BOTTOM)	92
Figure 47. Fracture Surfaces - 612 MPa I-P (TOP):612 MPa O-P (BOTTOM)	93
Figure 48. Transverse Cracking - Sectioned Specimen	95
Figure 49. Close-up of Transverse Crack Initiation at Interface	96
Figure 50. Fatigue Crack Growth from 90 <sup>0</sup> Ply	97
Figure 51. Summary of Crack Analysis	98
Figure 52. Fatigue Life Curves - Maximum Applied Stress	99
Figure 53. Fatigue Life Curves - Maximum 90 <sup>0</sup> Matrix Stress	100
Figure 54. Fatigue Life Curves - Maximum 0 <sup>0</sup> Fiber Stress	102
Figure 55. Classical Damage Growth Curve	105
Figure 56. Fatigue Damage Curves Using True $E_0$	106
Figure 57. MMC Damage Trend	107
Figure 58. Damage vs. Remaining Life after W-H Phase	109
Figure 59. Maximum Stress 248 MPa - In-Phase / 0-degree Ply	119
Figure 60. Maximum Stress 248 MPa - In-Phase / 90-degree Ply	120
Figure 61. Maximum Stress 367 MPa - In-Phase / 0-degree Ply	121

Figure 62. Maximum Stress 367 MPa - In-Phase / 90-degree Ply	122
Figure 63. Maximum Stress 441 MPa - In-Phase / 0-degree Ply	123
Figure 64. Maximum Stress 441 MPa - In-Phase / 90-degree Ply	124
Figure 65. Maximum Stress 612 MPa - In-Phase / 0-degree Ply	125
Figure 66. Maximum Stress 612 MPa - In-Phase / 90-degree Ply	126
Figure 67. Maximum Stress 293 MPa - Out-of-Phase / 0-degree Ply	127
Figure 68. Maximum Stress 293 MPa - Out-of-Phase / 90-degree Ply	128
Figure 69. Maximum Stress 367 MPa - Out-of-Phase / 0-degree Ply	129
Figure 70. Maximum Stress 367 MPa - Out-of-Phase / 90-degree Ply	130
Figure 71. Maximum Stress 441 MPa - Out-of-Phase / 0-degree Ply	131
Figure 72. Maximum Stress 441 MPa - Out-of-Phase / 90-degree Ply	132
Figure 73. Maximum Stress 612 MPa - Out-of-Phase / 0-degree Ply	133
Figure 74. Maximum Stress 612 MPa - Out-of-Phase / 90-degree Ply	134
Figure 75. In-Phase Profile Example	136
Figure 76. Out-of-Phase Profile Example	137
Figure 77. 50% IP and 60% OP Tests - Modulus Data	139
Figure 78. 441 MPa I-P Test Strain Progression	140
Figure 79. 612 MPa I-P Test Strain Progression	141

Figure 80. 367 MPa O-P Test Strain Progression . . . .	142
Figure 81. 441 MPa O-P Test Strain Progression . . . .	143
Figure 82. 612 MPa O-P Test Strain Progression . . . .	144

List of Tables

Table I. Material Properties of Fiber and Matrix . . .	41
Table II. Initial Modulus Measurements . . . . .	56
Table III. Failure Strain Summary - Total Strains . .	65
Table IV. Failure Strain Summary - Mechanical Strains . . . . .	66

Abstract

Metal matrix composites (MMCs) are rapidly becoming strong candidates for high temperature and high stiffness structural applications such as the Advanced Tactical Fighter (ATF). The development of fiber-reinforced metal alloys with improved strength-to-weight ratios make these materials critical to advanced aerospace vehicle design. Along with these needs comes the need to study and characterize the properties of these materials. This study focused on the development of test methodology and analysis of data from a computer-controlled test system and the acquisition of data from in-phase and out-of-phase thermomechanical loading conditions.

This study systematically investigated the failure modes and associated damage in a cross-ply,  $[0/90]_{2s}$  SCS<sub>6</sub>/Ti-15-3 metal matrix composite under thermomechanical fatigue. Nine fatigue tests were performed; one cyclic thermal test, four in-phase (I-P), and four out-of-phase (O-P) thermomechanical fatigue (TMF) experiments. Initiation and progression of fatigue damage are recorded and correlated to changes in Young's Modulus of the composite material.

Experimental results show an internal stabilization of reaction zone size but degradation and separation from

constituent materials under extended cyclic thermal loading. Under combined thermal/mechanical loading conditions, different forms of damage occurred. The most critical one was transverse cracks initiating in the 90° plies, growing and coalescing from fiber/matrix interfaces internal to the specimen, progressing outward through 0° plies before failure.

Maximum mechanical strain at failure was determined to be approximately  $\epsilon_u = 0.0075$  mm/mm. A correlation was made relating maximum matrix stress to failure life resulting in a fatigue threshold limit of 280 MPa. This limit is independent of frequency, temperature, or phasing conditions. Also, a maximum fiber stress of 1700 MPa, dependent on temperature, was related to ultimate tensile strength under static load.

An attempt was made to correlate the degradation in Young's Modulus with the applied cycles from different TMF tests. This correlation showed that the damage parameter  $D = (1 - E/E_0)$  reaches a certain maximum value before failure.

Further, a micromechanic analysis was performed to determine modes of damage progression. Time and stress level were both found to be governing factors in low-cycle TMF tests.

INVESTIGATION OF DAMAGE MECHANISMS IN A CROSS-PLY METAL  
MATRIX COMPOSITE UNDER THERMO-MECHANICAL LOADING

I. Introduction

A. Problem Definition

Metal Matrix and Intermetallic Matrix Composites (MMCs and IMCs) are currently being developed and tested for high-temperature and high-stiffness aerospace applications. (16:2) Vehicles under consideration for potential use of these materials are the Advanced Tactical Fighter (ATF) and the National Aerospace Plane (NASP). (16:1) An advantage of these composites is their superior strength and stiffness-to-density ratios as compared to monolithic materials.

Aerospace structures and engines required to achieve high supersonic and hypersonic flight speeds will experience a variety of temperatures and loading conditions. Materials in such a structure, whether an engine component, leading edge surfaces, or control surfaces, must be able to withstand the high stresses associated with monotonic and cyclic thermo-mechanical loading. (12:1)

Leading edge surfaces of the NASP are expected to experience temperatures exceeding  $1100^{\circ}\text{C}$  ( $2000^{\circ}\text{F}$ ), and therefore materials used in these structural components must maintain load bearing capability under extreme conditions.

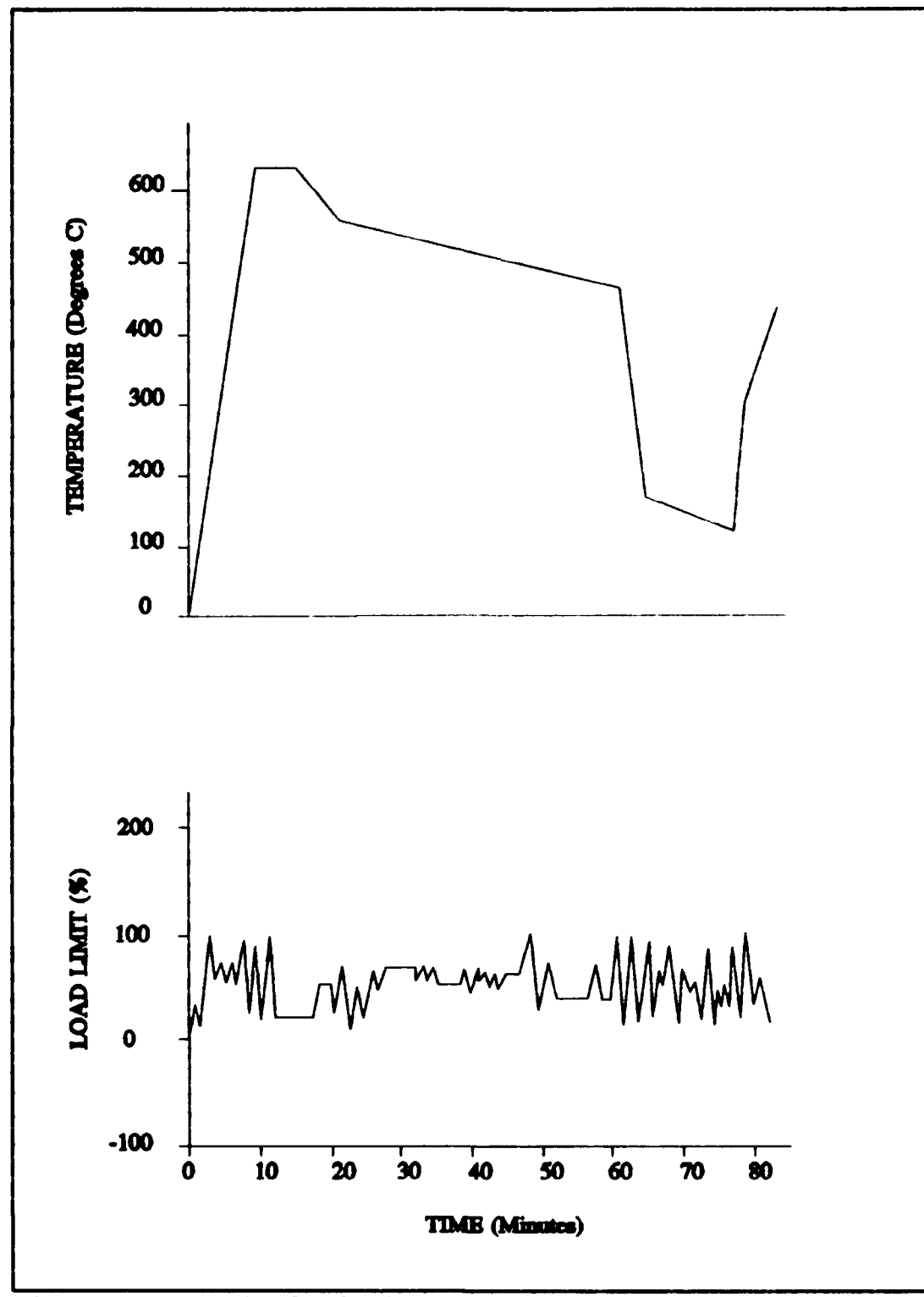


Figure 1. Typical Flight Component Temp/Load Profiles

(16:1) Figure 1 shows such an example of temperature and load profile history for an aircraft engine turbine disk.

Both continuous fiber and discontinuously reinforced metal matrix composites are being developed by the Department of Defense (DOD), each for its own distinct, specific properties. Continuous fiber reinforcement is expected to maintain sufficient strength and stiffness properties and limit creep at elevated temperatures. Also, the other obvious advantage of the metal matrix composite in aircraft use is its toughness and resistance to foreign object impact. (6:3)

The superior level of performance desired in high temperature materials is achieved through the use of high strength ceramic fibers and low density matrix materials. (4:1) Although the monotonic material properties of these materials can be predicted reasonably well using various computational codes and traditional rule of mixtures formulations, fatigue properties can not be predicted easily. Fatigue properties of MMCs are dependent on several factors. Fatigue damage modes and failure prediction through analytical methods is difficult. (8:2) Therefore, characterization of these materials' properties under various conditions of fatigue is limited to experimental investigation.

The composite materials combine materials with widely differing physical properties. (4:2) In MMC, although both materials have relatively low coefficients of thermal

expansion, there is a large differential between these coefficients, causing the matrix to expand or contract at a different rate, with temperature change, than the reinforcing fibers. For example, this differential causes the matrix of the material in this study to contract around the fibers during manufacturing cooldown or weaken interfaces and possibly debond at higher temperatures. Figure 2 shows these microstresses due to CTE mismatch. This requires a special consideration in MMC that is not found in the conventional polymer-based composites.

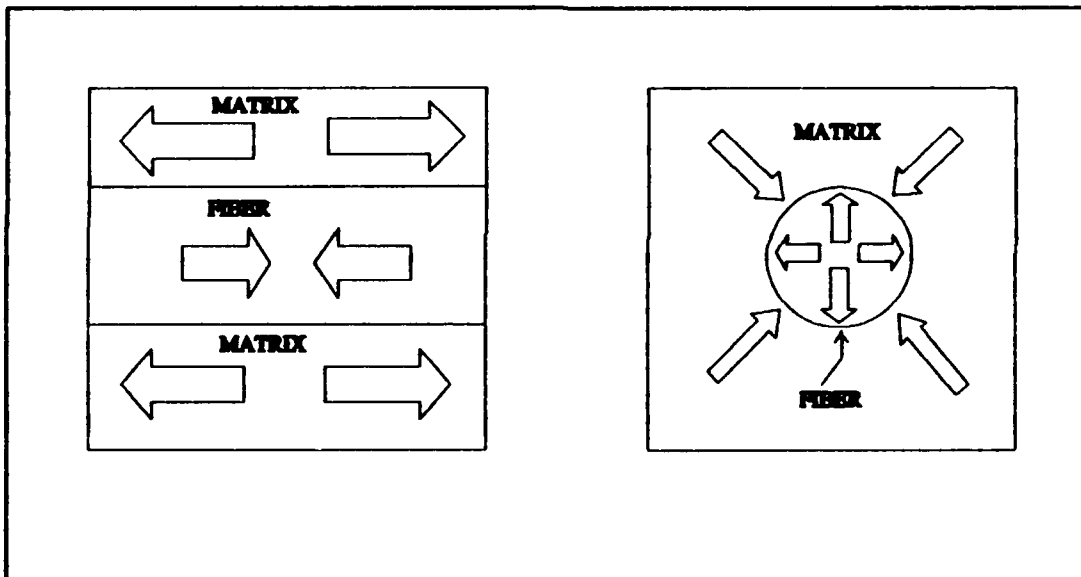


Figure 2. CTE Mismatch Representative Microstresses

A titanium-based alloy reinforced with continuous silicon carbide fibers, which exhibits a high strength-to-weight ratio and good thermal resistance, is a good model material to study the basic features of MMCs. (6:3) Experimental test results

with this material should be considered representative of the results expected from advanced titanium-based metal matrix composites. The particular interest in this study is a cross-ply [0/90]<sub>2S</sub> laminate of SCS<sub>6</sub>/Ti-15-3. Ti-15-3 is a short designator for Ti-15V-3Cr-3Al-3Sn, a  $\beta$ -Titanium alloy. This matrix material is reinforced with continuous silicon carbide fibers designated SCS<sub>6</sub>. This material system has potential for applications up to 700°C (1300°F), although without protective coatings, oxidation effects could limit its use.

(6:3)

To properly characterize a material's use for structural components, one must assess its properties accurately across the spectrum of its expected environments. Among the most harsh environments is the high temperature regime. Thermal effects, by themselves, are known to cause significant degradation in most MMCs. (17:90) SCS<sub>6</sub>/Ti-15-3 seems to be unique in that the mechanical response of uniaxial specimens subjected to thermal fatigue only (300-550°C) does not show any degradation on the macroscopic level. (8:11) Tensile tests performed by Gabb on uniaxial specimens at elevated temperatures (300 and 550°C) show fiber pullout as the primary failure mode with the fibers separating cleanly from the matrix at the interfacial layer. (8:12)

Several unique damage modes for MMCs have been reviewed by Johnson (15). These have been found to be dependent on the

relative properties of the specific matrix, fiber, and interface. For soft matrix composites such as B/Al, fatigue cracks develop in the matrix first. B/Ti systems develop cracking in the fibers first indicating lower fiber fatigue resistance. If the fiber-matrix interface is weaker than either of the other components, cracks can initiate in the interface and propagate to either constituent. If both the matrix and the fiber have similar properties, a crack may grow through both at the same rate ("self-similar" cracking). (8:2) as in the case of SiC/Ti which was in contrast to silicon carbide/aluminum. Johnson et al (16:40) reported degradation of material properties in a silicon carbide/titanium fatigue test at ambient conditions resulting from fiber matrix separation. Apparently, the additional strength of the titanium-based matrix over the aluminum causes the material to reach much higher stresses before matrix yielding. Therefore, the weaker fiber matrix interface was the failure point.

The interface or reaction zone in the Ti composite is developed by the combination of the high reactivity of titanium and the carbon-rich coating on the fibers during the manufacturing process. Because of this, interfacial properties are extremely difficult to predict and change throughout a fatigue test. (17:89) It is important to

properly characterize the failure mechanisms of this interface if we are to improve the performance of MMCs.

As it was mentioned earlier, extensive testing has been performed on SCS<sub>6</sub>/Ti-15-3 composite at room temperature by Johnson (16:2). This study showed that the 0° plies were controlling fatigue life in the angle-ply system. The authors developed a model based on stress in the 0-degree fibers. Gayda et al (9:2) studied the fatigue behavior of unidirectional SCS<sub>6</sub>/Ti-15-3 composites at elevated temperatures. This study showed that on a stress-range basis the isothermal fatigue life (at 300°C and 550°C) was higher than the matrix alloy, the reverse was true when fatigue life was compared on a strain-range basis. The authors concluded fatigue life was not matrix dominated but was governed by interface characteristics. In a subsequent study, isothermal, in-phase, out-of-phase, and load-controlled bithermal TMF experiments were performed on the same unidirectional composite between 300°C and 550°C. Both in-phase and out-of-phase fatigue lives were found to be shorter than fatigue life at isothermal temperatures. On a strain-range basis, in-phase and out-of-phase fatigue lives fell on the same curve indicating no differences. Again, the behavior was attributed to the fiber-matrix interface (18:9).

Each composite material as well as laminate lay-up usually may have different overall material characteristics.

No study has been reported to characterize the cross-ply laminate of MMC under TMF conditions. Therefore, there is a need to characterize other lay-ups such as the cross-ply laminate.

The first part of this effort was to acquire and improve the existing test mechanism capable of thermal cycling to perform a systematic study of the SiC/Ti cross-ply laminate under TMF conditions. Additions to the existing system used by P.G. Ermer (6:24) included a computer code developed by Mr. George Hartman of the University of Dayton Research Institute for control and phase synchronization of loading and thermal test conditions and for data acquisition. A modified air cooling arrangement and a floating free-end extensometer for strain measurements were also added. The study was then undertaken to perform systematically material tests for a  $[0/90]_{2S}$  SCS<sub>6</sub>/Ti-15-3 MMC under in-phase and out-of-phase thermomechanical load conditions. Strains and Young's Modulus measurements were recorded for analysis and specimens were examined during testing using replica techniques. Fractography and sectioning of the failed specimens after testing for SEM analysis provided examination of the reaction zones and fracture surfaces.

## II. Background

### A. Thermal and Thermo-Mechanical Fatigue of MMCs

Cyclic loading conditions, whether thermal or mechanical, can initiate cracks in a material through plastic deformation. Although nominal stresses in the material could be below the elastic limit, stress concentrations due to voids, inclusions, or in the case of MMCs, fiber/matrix interfaces may cause stresses to be above yield. Under tension-tension load conditions these plastic deformations provide the mechanism for fatigue cracking through residual compressive forces during the unload portion of the load cycle. (3:57-59) Under thermal loading conditions it has been shown that the differential of CTEs for material components can cause similar stress concentrations and possibly fatigue damage through degradation of the interface zones between fiber and matrix.

Investigators of thermal and mechanical fatigue of MMCs have found these materials to be less adaptable to crack growth measurement techniques and have been more concerned with when, how, where, and why damage initiates and how damage progression can be characterized. For basic research on thermo-mechanical fatigue, two major test components are required. First, there must be a mechanical holder/loading mechanism and second, a temperature control system. The temperature or load fatigue profiles can be executed in many

ways to include sinusoidal, triangular, square or combination waveforms. (6:7) Figure 3 shows in-phase and out-of-phase triangular profiles used in this study.

Four basic methods have been used to heat specimens for thermal testing: (1) fluidized beds, (2) radiation, (3) resistance heating, and (4) radio frequency induction. (6:9)

The hot fluidized bed technique is good for heating and cooling specimens at a high rate by immersing them alternately in hot and cold fluid beds. (6:9) This technique would be difficult, though, to simply adapt to thermomechanical testing where a loading apparatus must be accommodated at the same time.

Radiative heating lamps have also been used by investigators. Heil (11:20,23) used four quartz lamps to perform cyclic tests between  $427^{\circ}\text{C}$  ( $800^{\circ}\text{F}$ ) to  $634^{\circ}\text{C}$  ( $1200^{\circ}\text{F}$ ). A control system using compressed cooling air and welded type-K thermocouples for feedback were used in this setup.

Two methods of resistance heating have been applied to thermal heating techniques. The first uses a molybdenum rod coiled around cylindrical specimens, heating them to  $1785^{\circ}\text{C}$  ( $3272^{\circ}\text{F}$ ). (6:9-10) The second method passes high current directly through the specimen at heating rates of up to  $24^{\circ}\text{C}$  ( $100^{\circ}\text{F}$ ) per second and temperatures cycled  $79^{\circ}\text{C}$  ( $200^{\circ}\text{F}$ ) to  $523^{\circ}\text{C}$  ( $1000^{\circ}\text{F}$ ). Radio frequency techniques have been used for thermomechanical (TMF) testing of superalloys. (6:10)

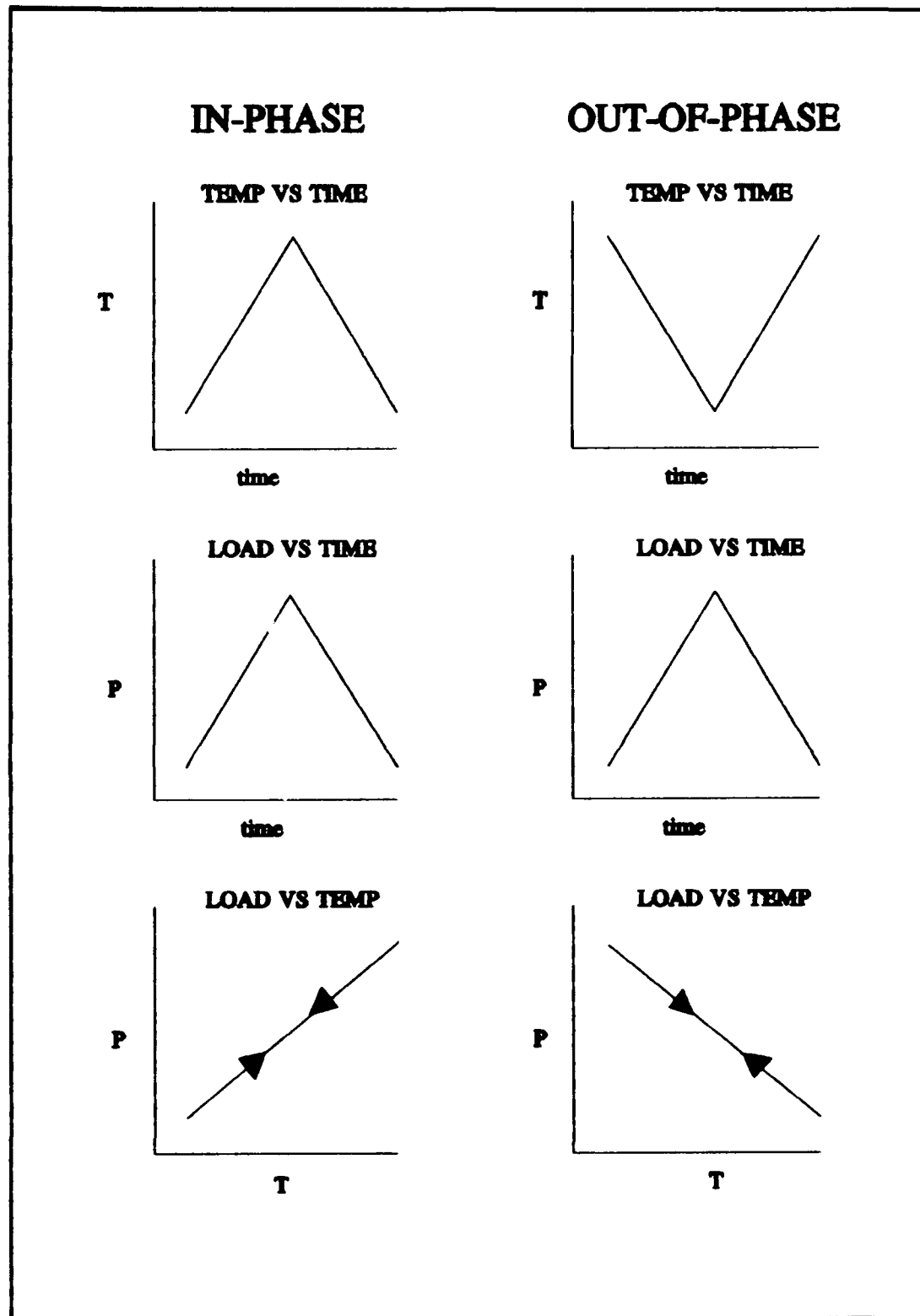


**Figure 3. Temperature/Load Profiles**

The method applied for the approach to TMF testing in this study was to use radiative lamp heaters. The quartz lamps, combined with compressed air cooling and thermocouples welded to the specimens provide adequate temperature control for the thermal aspect of these tests.

High temperature strain measurements have been accomplished through several techniques: (1) laser extensometer (10:24-26), (2) high temperature extensometers (6:10). Majumdar and Newaz (18:5) used a strain gauge type extensometer modified to include ceramic probes to isolate the extensometer's components from the heated area.

One of the most difficult problems in TMF testing to overcome is the synchronization of temperature and load phase angles. Whether the test being conducted is in-Phase (IP) or out-of-Phase (OP), the phasing angle is critical to the results. Under load controlled tests the fatigue lives for IP and OP tests differ greatly and continuous updates of the phase angle must be performed by the test mechanism. Improper phasing of the tests can cause distorted hysteresis loops and make analysis of the test data difficult (4:3). Castelli and Ellis developed specialized control software to control these subtle phase shifts. By prematurely reversing the temperature-command so temperature response would reverse simultaneously with mechanical load, adequate control of phasing was achieved. The method used in the MATE263 (19)

software from UDRI incorporates "mechanical load hold" to adjust for phase differences. Because of the faster load command response time, load is held or advanced to the appropriate level in the cycle to allow the temperature waveform time to synchronize without any shift in existing thermal gradient conditions.

#### B. Recent Advances - Metal Matrix Composite Testing

Extensive testing of static strengths and mechanical properties have been conducted using the SCS<sub>6</sub>/Ti-15-3 composite. Johnson et al (16:7) tested five different lay-ups at room temperature for static and fatigue properties. Laminates with off-axis plies were found to suffer fiber/matrix interface failures at stress levels as low as 20 ksi affecting the properties of the laminates. This stress level was well below the constituent matrix properties. Fatigue tests were conducted to failure at varied stress levels. It was found that the stress in the zero degree fiber could be used to correlate fatigue lives under ambient conditions in those laminates containing 0° fibers.

Ermer (6:59) tested uniaxial specimens for property degradation due to thermal fatigue cycling and found no significant degradation in ambient properties. It was noted, however, that the interface zones of the specimens had

enlarged and were radially cracked, showing a marked change in interface properties over the course of 16,000+ cycles.

Gabb, et. al. (8:8-10) conducted several static, isothermal, and nonisothermal tests on uniaxial specimens. It was concluded that mechanical response of the composite did not vary with specimen geometry. Reduced section and rectangular specimens showed the same response. Specimens were heat-treated at 593°C for 24 hours prior to testing. Tensile tests of 0° and 90° specimens at 300°C and 550°C showed fracture strains of 0.85-1.0% and 1.4-1.65% respectively. The 0° tests also showed strains were predominantly elastic with inelastic strains of only 0.1%. Transverse specimen tests showed more inelasticity and significantly reduced strength. In isothermal fatigue tests, some measurable inelastic yielding was measured during the first cycle of testing but this inelastic strain became negligible with continued cycles. These tests showed a relatively constant modulus for two-thirds of specimen life with modulus then decreasing to failure. Cyclic mean strain also increased during the first 100-200 cycles and did not show a stress dependence. Nonisothermal fatigue tests were also nominally elastic and the elastic modulus remained relatively constant for the first two-thirds of life. Cyclic in-phase tests showed initial mean strain increase, though smaller in magnitude, as in the 550°C (1022°F) isothermal tests, but out-of-phase tests showed no

consistent initial mean strain increase. The nonisothermal tests conducted in this study were pseudo-in-phase tests with each cycle accomplished by increasing temperature to a maximum value and holding until a full stress cycle was imposed, then decreasing the temperature back to its minimum value. For out-of-phase tests the stress cycle was superimposed at a minimum temperature hold. Fatigue damage noted by Gabb et al was demonstrated in isothermal specimens as cracks initiating at the fiber/matrix interface throughout the specimen cross section and then growing and coalescing over short distances before failure. Self-similar cracking was not a predominant damage mechanism. In nonisothermal tests, cracks initiated at the surfaces or at near-surface fiber/matrix interfaces and grew long distances through the specimen. The nonisothermal cycling caused great interface damage.

Load-controlled thermo-mechanical fatigue (TMF) and isothermal fatigue (IF) tests were conducted by Majumdar and Newaz (18:7) on angle-ply lay-ups of the SCS<sub>6</sub>/Ti material. TMF tests were conducted over the temperature range of 315-650°C (600-1200°F) and IF tests at 650°C (1200°C). TMF life was found to be significantly shorter than IF life on a stress range basis. Transverse microcracking was found to be a damage mechanism in both the IF and TMF specimens. These cracks originated from the fiber/matrix interface or reaction zone. In the TMF specimens the transverse cracking was

localized in the fracture surface area and there was additional longitudinal inter-ply delamination near and away from the fracture surface. Majumdar and Newaz noted in their study that the matrix alloy is slightly metastable and the  $\alpha$ -phase precipitates with high temperature aging. This aging tends to slightly increase room temperature modulus and strengths, but effects of subsequent overaging were not adequately characterized. The effect of aging on room temperature properties for  $[0/\pm 45/90]_S$  lay-up was small.

Castelli, et. al. (4:12-18) tested uniaxial specimens under IF, and TMF (in and out-of-phase) conditions. Specimens were heat treated at  $700^{\circ}\text{C}$  for a 24 hour period but it should be noted that the authors believed the matrix to be still slightly metastable. IF tests were conducted with a 10 cycle/minute frequency at  $427^{\circ}\text{C}$  ( $800^{\circ}\text{F}$ ) and TMF tests were 3 minute cycles on a temperature range of  $93-538^{\circ}\text{C}$  ( $200-1000^{\circ}\text{F}$ ). Each type of test had distinct failure modes. Isothermal tests revealed extensive matrix cracking with fiber damage throughout the specimen. In-phase conditions showed extensive fiber cracking throughout the cross-section with minimal matrix damage. Out-of-phase tests showed extensive matrix damage with minimal fiber cracking. In general, all failed specimens exhibited flat failure surface due to fatigue cracking, random fiber pullout, and areas of ductile matrix

failure. Higher stressed specimens showed increased fiber pull-out and ductile fracture failure areas.

In summary, the following general trends were observed from the above mentioned studies:

- a) Specimen geometry has little to do with mechanical properties, in fact reduced section composites tend to fail more readily where gauge length meets curvature.
- b) Most specimens experience inelastic yielding during first cycle of testing, stabilizing to a constant elastic cycle with few additional cycles.
- c) In isothermal tests, specimens showed a rapid mean cyclic strain increase over the first 100-200 cycles, without dependence on stress level. In-phase testing showed similar but smaller magnitude trends. Out-of-phase tests did not respond with any consistent strain increase trend in this interval.
- d) For heat-treated specimens (24 hour treatment period) modulus remained relatively constant for 2/3 of specimen life.
- e) TMF life was consistently shorter than IF life for angle-ply lay-ups under load-controlled tests. Strength for angle and transverse lay-ups is significantly reduced - well below that of the

matrix material strength - probably due to matrix/fiber debond at interfaces.

f) Transverse microcracking is the predominant damage mechanism in all cases. The origin of these cracks varies with lay-up and thermal/load conditions. Fracture surfaces exhibit flat fatigue regions with scattered fiber pull-out and ductile matrix failure areas.

#### C. METCAN - Metal Matrix Composite Analyzer

METCAN (METal Matrix Composite Analyzer) is a FORTRAN language computer code designed to perform linear and non-linear analysis of fiber-reinforced metal matrix composites. The program was developed at the NASA Lewis Research Center and is primarily focused for use in providing material properties compatible with large structural analysis programs such as MSC/NASTRAN. The code outputs data in standard formats and as an example, the program is set up to write laminate material property cards in the correct format for use in MSC/NASTRAN. METCAN uses a multi-cell model (MCM) composed of a unique set of micromechanics equations developed by Hopkins and Chamis (14) for use in analysis of high temperature metal matrix composites. The equations for the model are closed form expressions derived to give equivalent pseudo homogeneous properties for a unidirectional fiber

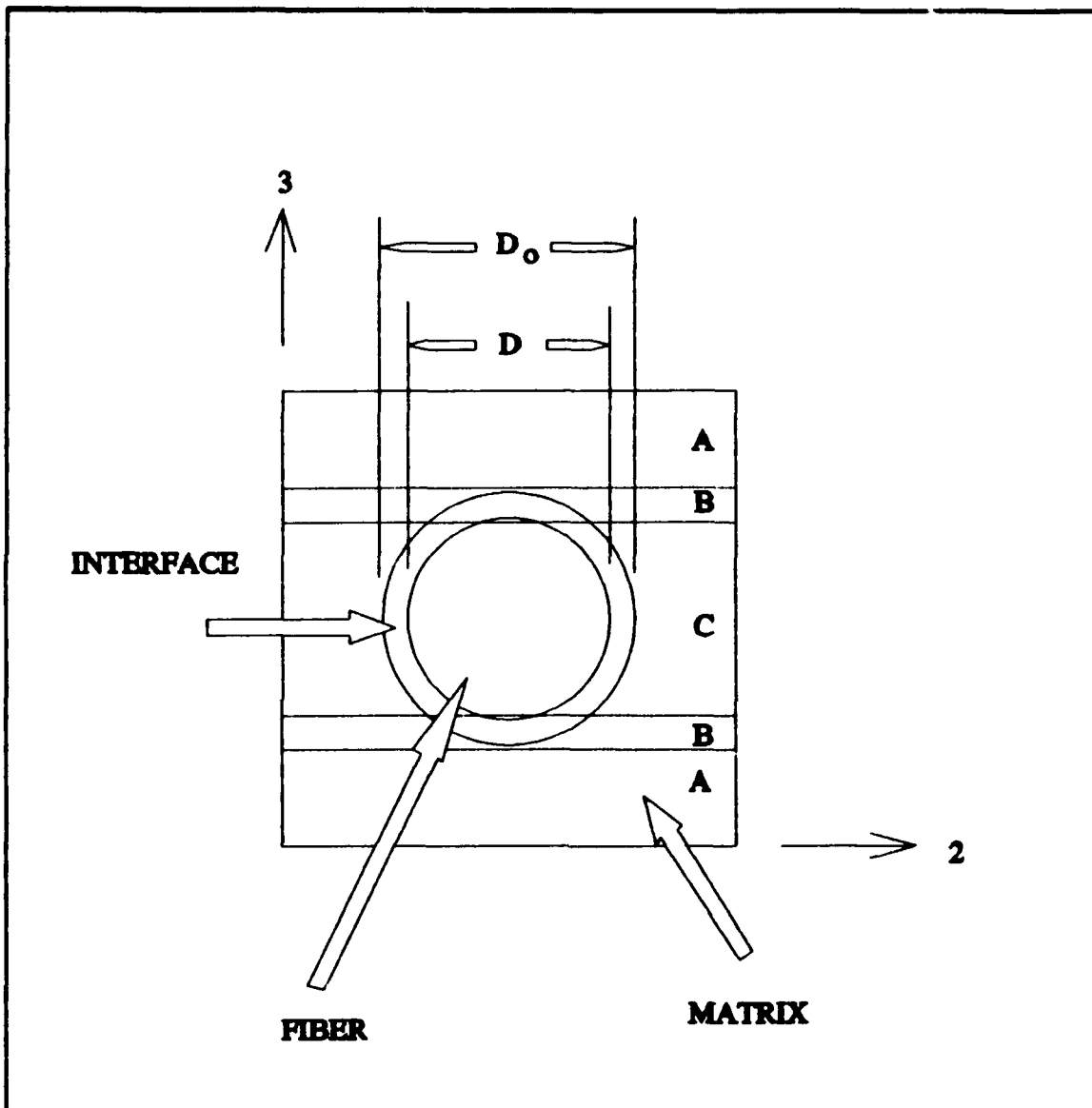


Figure 4. Multi-Cell Model

reinforced ply. The MCM has been adapted for use in METCAN by (20) Murphy and Hopkins. These properties are then, in turn, used in various orientations to predict, in general, laminate properties by METCAN. In the process, the program calculates component parameters to include microstresses for fiber, matrix, and if desired, the interface region of the MMC.

General principles of displacement, compatibility, and force equations were used in the formulation of the MCM. The structure of the uniaxial composite ply is approximated by the unit cell model, as shown in Figure 4. This unit cell model is broken into three distinct subregions to characterize the through-the-thickness nonuniformity of structure and constituent material properties.  $D$  is defined as the fiber diameter and  $D_0$  is the diameter of the fiber with interface thickness. The set of micromechanics equations used in the MCM are derived for the transversely isotropic case (isotropic in the  $X_2$ - $X_3$  plane) under the assumption of isotropic or at least transversely isotropic constituent materials.

A complete set of the micromechanics equations are summarized in Reference 14. The equations encompass expressions for ply equivalent mechanical properties, ply equivalent thermal properties, ply in-plane uniaxial strengths, and thermomechanical constituent stresses. Example equations for longitudinal properties are as follows:

#### Ply Mechanical Properties (Longitudinal Modulus)

$$E_{111} = v_m E_{m11} + v_f \left( \left( 1 - \left( \frac{D}{D_0} \right)^2 \right) E_{d11} + \left( \frac{D}{D_0} \right)^2 E_{f11} \right) \quad (1)$$

Ply Thermal Properties (Longitudinal Coefficient of Thermal Expansion)

$$\alpha_{111} = v_m \left( \frac{E_{m11}}{E_{l11}} \right) \alpha_{m11} + v_f \left( \left( 1 - \left( \frac{D}{D_0} \right)^2 \right) \left( \frac{E_{d11}}{E_{l11}} \right) \alpha_{d11} + \left( \frac{D}{D_0} \right)^2 \left( \frac{E_{f11}}{E_{l11}} \right) \alpha_{f11} \right) \quad (2)$$

Constituent Stresses (Longitudinal Fiber and Matrix)

$$\begin{aligned} \sigma_{f11} &= \left( \frac{\sigma_{111}}{E_{l11}} + \delta T (\alpha_{111} - \alpha_{f11}) \right) E_{f11} \\ \sigma_{m11} &= \left( \frac{\sigma_{111}}{E_{l11}} + \delta T (\alpha_{111} - \alpha_{m11}) \right) E_{m11} \end{aligned} \quad (3)$$

Subscripts f, m, d, and l denote fiber, matrix, interface, and lamina properties respectively. E,  $\alpha$ , and v are the modulus, coefficient of thermal expansion (CTE), and fiber volume ratio.  $\delta T$  defines the temperature change.

Thermoviscoplastic nonlinear constitutive relationships (TVP-NCR) are also used in METCAN. The relationships were formulated for use with METCAN by Chamis and Hopkins (14). The equations consist of the product of several terms with unknown exponents which are determined from available experimental data or estimated from anticipated behavior of a particular term. A general form of the TVP-NCR is as follows:

## Thermoviscoplastic Nonlinear Constitutive Relationship

$$\frac{P}{P_0} = \left( \frac{T_F - T}{T_F - T_0} \right)^n \left( \frac{S_F - \sigma}{S_F - \sigma_0} \right)^m \left( \frac{\dot{S}_F - \dot{\sigma}_0}{\dot{S}_F - \dot{\sigma}} \right)^l \left( \frac{T_F - T}{T_F - T_0} \right)^k \dots \\ \dots \left( \frac{N_{MF} - N_M}{N_{MF} - N_{M0}} \right)^q \left( \frac{N_{TF} - N_T}{N_{TF} - N_{T0}} \right)^r \left( \frac{t_F - t}{t_F - t_0} \right)^s \quad (4)$$

Where the following variables are defined as:

- P property of interest
- $P_0$  corresponding property at reference
- T current temperature
- $T_0$  reference temperature where  $P_0$  is determined
- $N_M$  number of mechanical cycles
- $N_T$  number of temperature cycles
- $S_F$  fracture stress determined at  $T_0$  conditions
- $\sigma_0$  reference stress where  $P_0$  is determined
- $\sigma$  current stress state

and the subscripts F, 0, M, T, denote the final or characteristic property, reference, mechanical, or thermal, respectively. Dotted terms denote the time rate of change in the variable. Exponents n, m, l, k, q, r, and s, as mentioned earlier, are determined from observed or expected behavior. Each respective term in the relation relates to a different property effect. Respective to the above exponents, the terms in their order of appearance relate temperature, stress,

stress rate, temperature rate, mechanical cycles, thermal cycles, and time.

Although METCAN can be used to analyze a material under a variety of thermomechanical conditions, the program was used for this study to predict the constituent microstresses in the matrix and fiber of the cross-ply laminate SCS<sub>6</sub>/Ti-15-3 under given test conditions with given initial material characteristics and fabrication conditions.

For analysis with METCAN, properties in the existing property databank were initially used. Modifications to these properties to compensate for measured parameters from our tests (i.e. modulus, CTE) were then iterated until a reasonable match with ambient Young's Modulus was reached. This meant decreasing the matrix modulus property to a value of 62 GPa (9.0 MSI) to achieve a 138 GPa (20 MSI) composite longitudinal modulus with the [0/90]<sub>2S</sub> layup. Fiber volume ratio ( $V_f$ ) was determined through fiber cross-sectional measurements in photographs to be .386. For factory cooldown at manufacturing, an initial stress-free condition was assumed at 1000<sup>0</sup>C (1832<sup>0</sup>F) cooling to 21<sup>0</sup>C (70<sup>0</sup>F) ambient conditions.

### III. Experimental Equipment/Procedure

The general test set-up used for this study is comprised of several major components, to include: a 20 kip Material Testing Systems (MTS) hydraulic test stand, MTS Microconsole, Micricon thermal control unit, MTS high temperature extensometer, Wavetek waveform generator, and a Zenith 248 personal computer with data acquisition capability. See Figure 5 for diagram of overall test set-up.

#### A. General Discussion

Specimens were held for testing by the MTS test stand in high-temperature (water-cooled) hydraulic grips. Load control during testing was accomplished through the MTS Microconsole receiving waveform commands from the MATE263 (19) test software channelled through the Wavetek waveform generator. Thermal conditions for the tests were achieved using two quartz lamp heaters controlled by the Micricon control unit receiving feedback through thermocouples attached to the specimen in the heated zone. The micricon unit receives its waveform commands directly from the MATE263 program in the form of programmed input. MATE263 also provides periodic phasing updates to the Microconsole and the Micricon units to ensure proper phase margins are maintained throughout the TMF tests.

Strains were recorded through periodic data acquisition cycles (DACs) at user-defined intervals by MATE263. Each DAC monitors strains, stresses, temperatures, and time during its execution. In turn, MATE recorded these values in a loop storage file and recorded maximum and minimum strain, cycle number, max load, actual load ratio, and sample number in a log data file which recorded the history of the test. All components used in the test set-up will be described in detail in the next section.

#### B. Test Components

i. Computer Control. The computer system used for overall control of the test was a Zenith 248 personal computer. A National Instruments IEEE-488 interface board was installed to provide the interface between the computer and the various control and data acquisition components during testing. See Figure 6 for a block diagram of the computer control system. MATE263 is a computer control software system specifically designed by Mr. George Hartman of the University of Dayton Research Institute for thermo-mechanical fatigue testing. Parameters such as specimen size and shape, material characteristics, requested phase angle, max stress, max and min temperatures, and system specific parameters such as maximum load range and extensometer range input by the user enable the program to be user-tailored for specific test

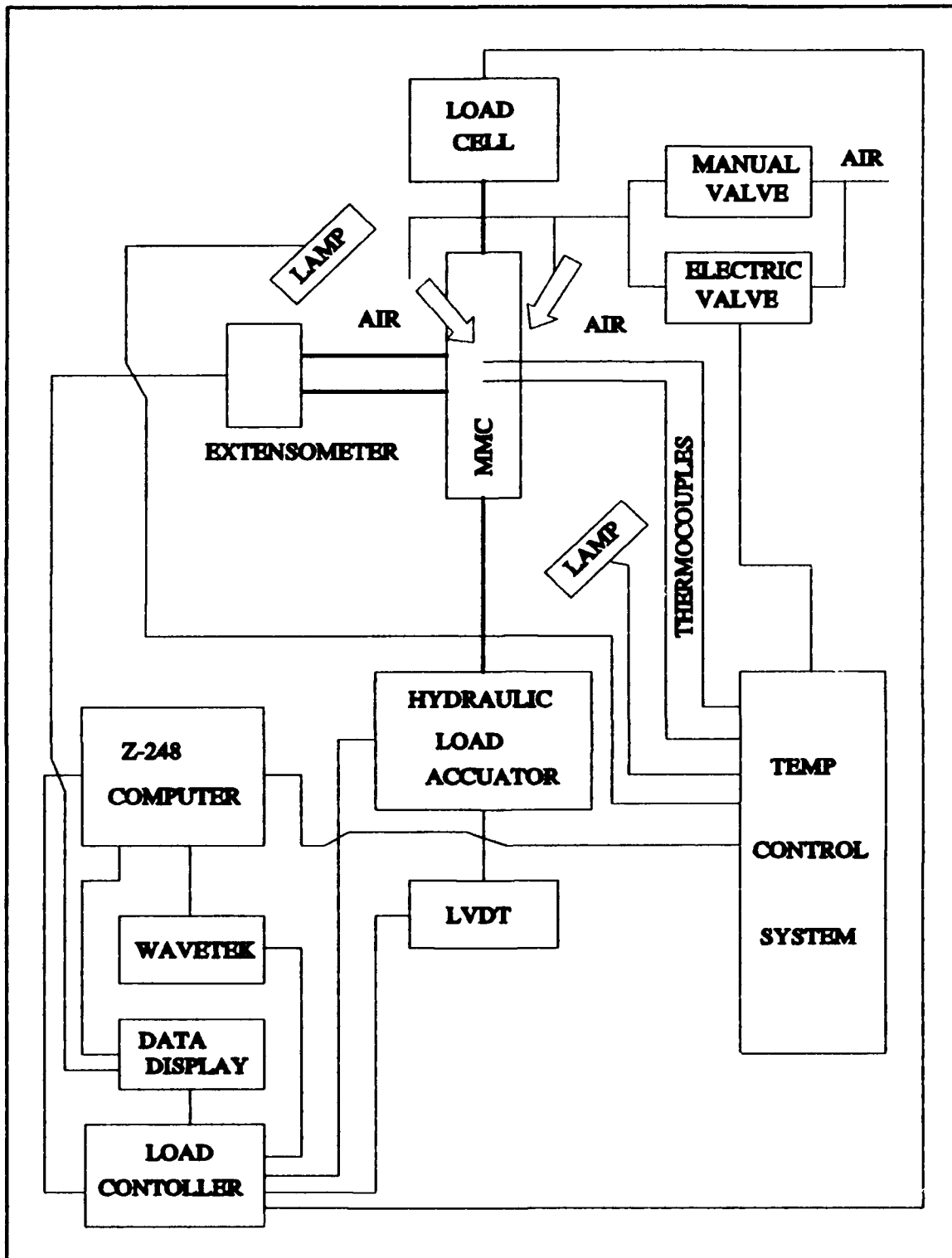


Figure 5. Test System Block Diagram

requirements. The program simultaneously monitors temperature, load, and displacement readings from the various components of the system and calculates stress and strain using the given specimen parameters such as cross-sectional area and gauge length. During each DAC, the program checks the phase angle between selected points in the load and temperature waveforms and makes an adjustment to the correct phase if there has been any drift. The program accomplishes the task by using a "load-hold" or "load-advance" at the appropriate time in the cycle. This allows the temperature profile to remain unchanged and since the load control response from the hydraulic actuator is much faster than the temperature system, this prevents erratic temperature gradients in the specimen.

ii. Mechanical Components. A block diagram of the mechanical loading system is shown in Figure 7. A 22 kip MTS model 810 servohydraulic stand supports the load application of the tests. This stand is equipped with water-cooled high temperature hydraulic wedge grips and is controlled by the MTS microconsole model 458.20. The stainless steel grip surfaces are cooled using forced distilled water from a central cooling pump also used for lamp cooling (discussed later). The MTS microconsole was calibrated prior to initial tests and all tests were completed using the 4000 lb maximum load range to minimize low load system drift (noise) while having full

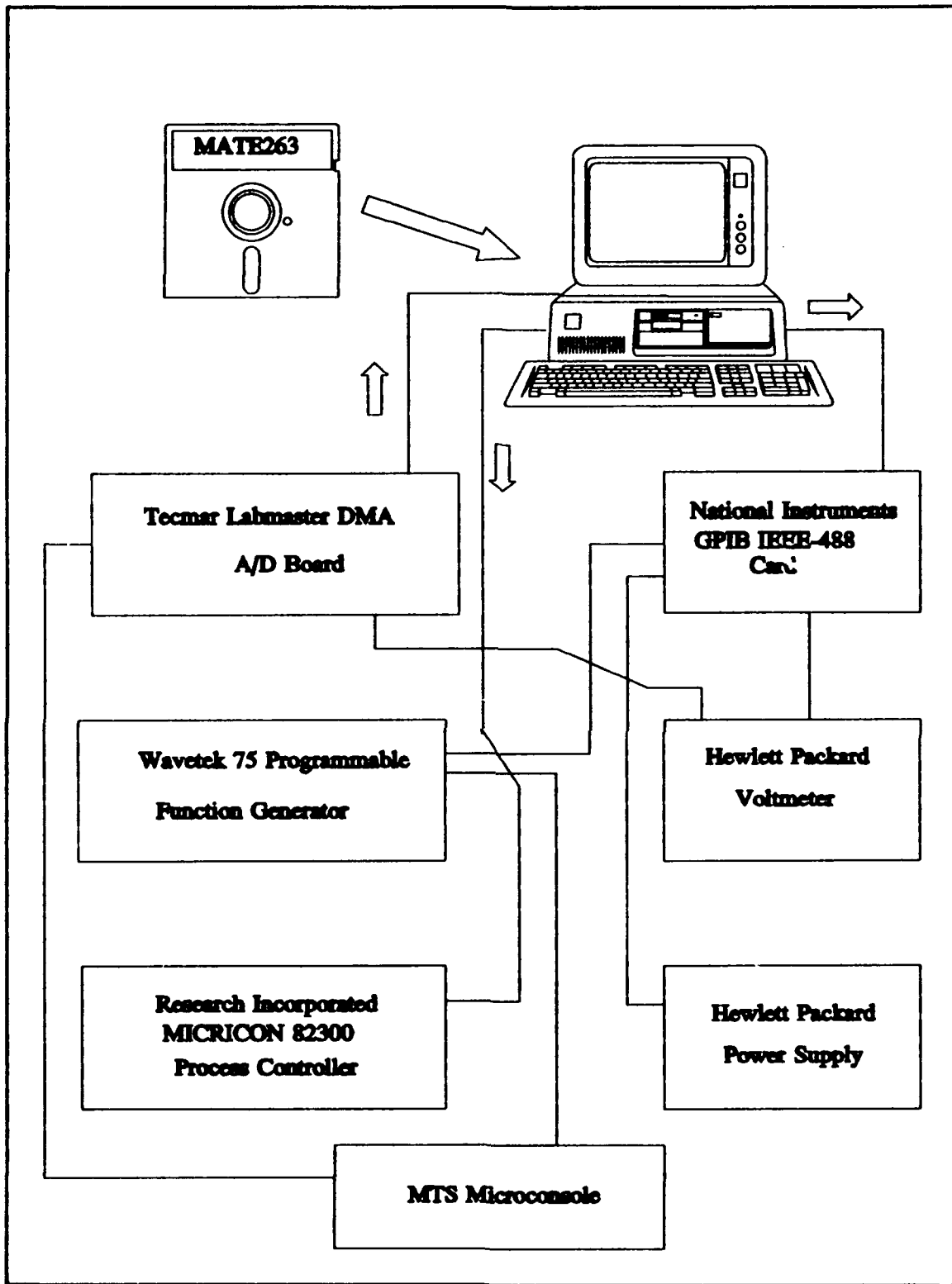


Figure 6. Computer-controlled Test System

capability without changing load range for anticipated maximum load requirements under each of the planned load conditions. Commands for load control of the test are received at the Microconsole from the Wavetek waveform generator under direction of the central MATE program. Voltages or engineering parameters can be read directly from the data display by the user and are also monitored by the program during testing. One safety feature added to allow active observation of the test and protect the observer from the intense light radiated from the lamps was a tinted plexiglas safety shield mounted through a rod and knuckle arrangement to the test stand (6:29).

iii. Thermal Components. Thermal control of the test system is accomplished from the Micricon 823 process control system (equipped with 2 channels). Other major components of the heating/cooling system include:

- Two quartz lamp heaters
- Manual and process controlled air cooling system
- Zenith 248 Computer
- Cooling water system (lamp coolant)

A block diagram of the thermal control system is shown in Figure 8. The specimens were heated using two quartz lamp heaters. These parabolic strip type heaters use 1000 watt

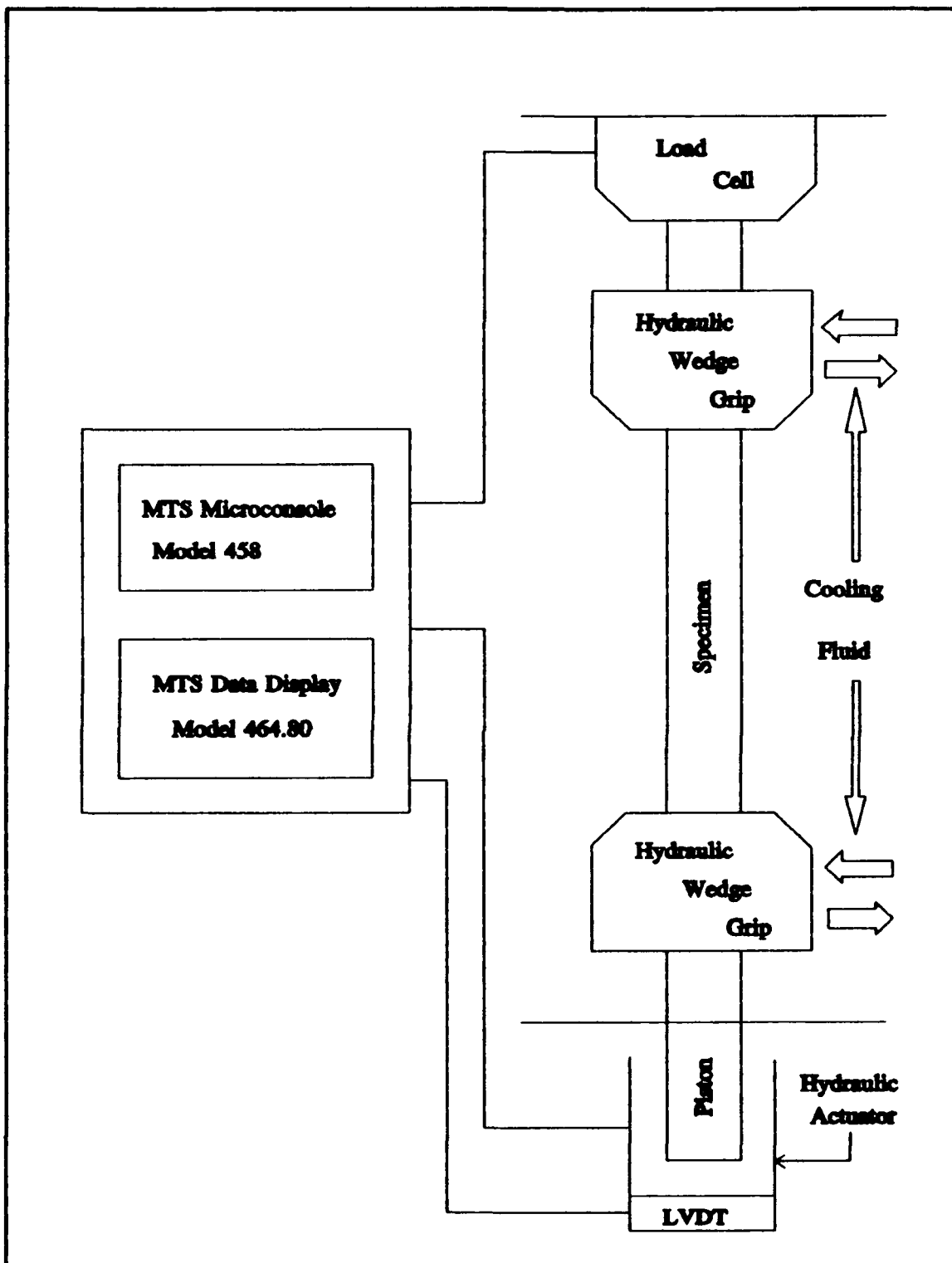


Figure 7. Mechanical Loading System

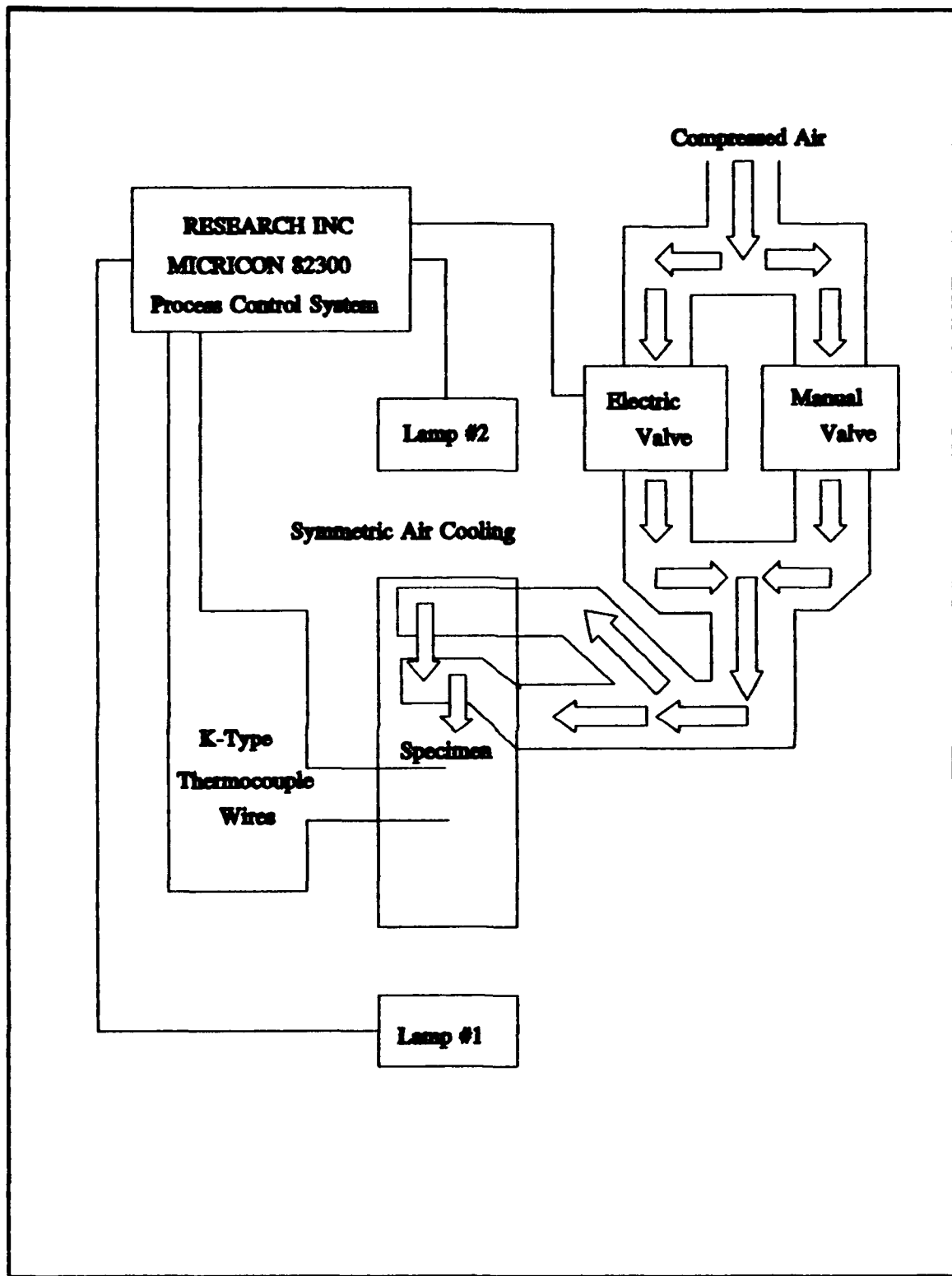


Figure 8. Thermal Control System

tungsten-filament quartz lamps that reflect radiant energy from the reflective parabolic surface onto the specimen. This radiant energy is then absorbed by the specimen and converted directly to heat energy. One major advantage of this type of heating method is that the radiant energy passes quickly through the air without heating it, allowing most of the energy to be transmitted to the specimen. Although the specimens should be non-reflective to absorb maximum energy, the energy transmitted for these tests was sufficient to generate a  $149^{\circ}\text{C}$  ( $300^{\circ}\text{F}$ ) to  $427^{\circ}\text{C}$  ( $800^{\circ}\text{F}$ ) triangular temperature profile. Appendix B shows example In-Phase and Out-of-Phase profiles from actual data.

Lamp heaters were mounted to the main stand of the MTS machine through a rod and knuckle arrangement. The adjustable mounts provided the ability to adjust easily the lamps' positions and angles relative to the specimen as well as enable the user to swing the lamps out from the test to allow ready access to the specimen for replica tests, observations, or to access thermocouple mounting locations. Once the lamps are in an optimal location for uniform heating of the gauge length the adjustment screws can be tightened to prevent any disturbance of the lamps during testing.

One lamp was positioned on each side of the specimen and was positioned horizontally to heat the gauge length section. The gauge length of the specimen had overlap of the lamp

heating and therefore both lamps were heating the same area of the specimen. Initially a probe thermocouple was mounted to the specimen in varying locations to monitor within and outside the heated section of the specimen. This testing showed less than a 5% variation of temperature within the gauge length and a sharp drop of temperature in excess of 30% at 1 mm outside the length.

Due to the low conductivity of heat (or electricity) through the titanium alloy, little energy was actually passed outside the gauge length section and this was quickly dissipated by the cooling air flow on the specimen. Initially this air flow was generated using an apparatus similar to the one used by Ermer (6). The apparatus used a singular copper tube formed into a u-shape and perforated to provide cooling air jets to the specimen. These jets were directed to have one side of the specimen cooled from above and the other one from below the gauge length directly opposing the lamp positions. It was found that although the temperature variation between the two sides of the specimen were within 2% of each other, using this method with a 12.7 mm (0.5 in) gauge length left the top end of the gauge length 5-10% warmer than the bottom end of the length. This may have been due to two factors. The second set of jets in series for a singular tube has a reduced air flow as compared to the first and there also was some conduction of heat upward in the vertical specimen.

A new air arrangement was used with the air supply being split to provide two independently adjustable cooling jets in parallel. The flow was used to symmetrically cool both sides of the specimen with a downward airflow, this arrangement reduced the variation in the gauge section to within 5% and provided a more localized heated zone.

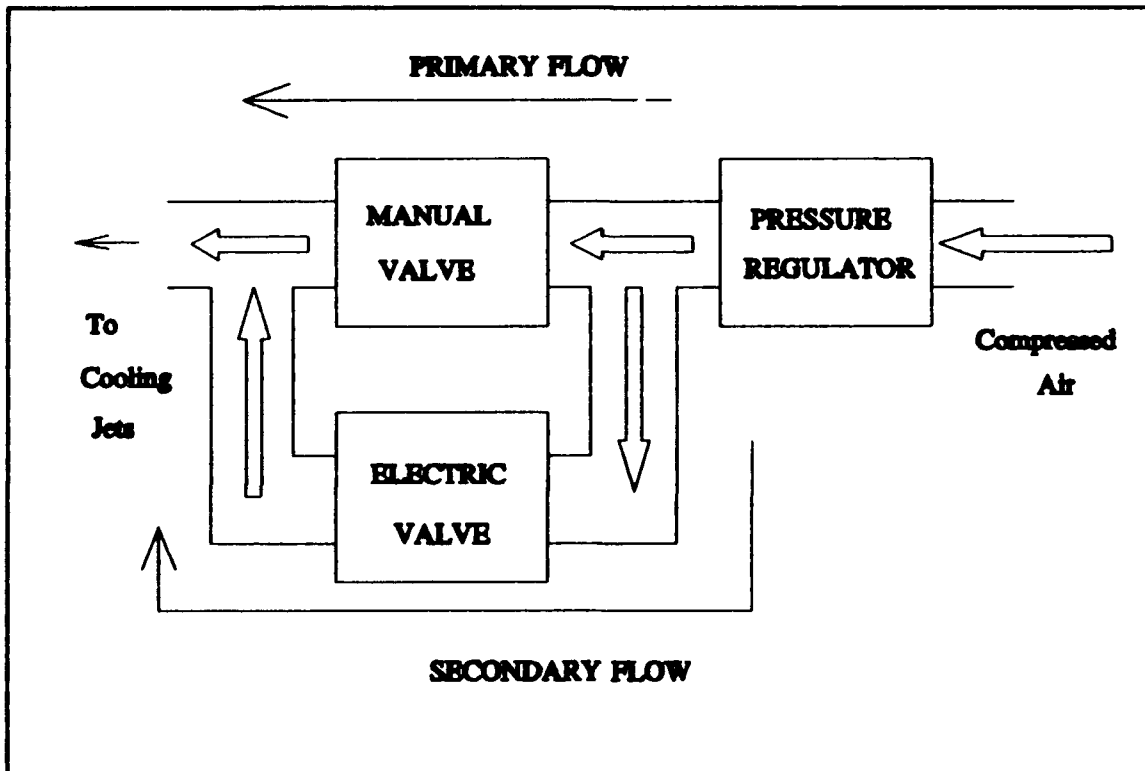


Figure 9. Air Line Schematic

The air supply for the cooling of the specimen was divided into three lines. See Figure 9 for the air line schematic. The first was a bleed line to the extensometer cooling vent. The second was a manual valve to control bleed air directly to the specimen. This low level air flow was necessary to achieve an even heating slope in the profile.

The third line was in parallel with the manual valve line and was connected to an electrical servovalve controlled by the Micricon control unit. This servovalve opens during the cooling portion of the profile to rapidly cool the specimen. This rapid cooling line was essential to achieving a 48 second triangular profile of 149-427°C (300-800°F).

A Micricon 82300 process control system was used to power the heating lamps and two Chromel-Alumel (type-K) thermocouples were welded to the specimen to provide temperature feedback information. A third thermocouple was used in various locations during preliminary testing and on test specimens to check heated area and unheated area temperature variations during tests. The Micricon uses three-mode (proportional (gain), integral (reset), and derivative (rate)) PID control. PID control of the Micricon is shown in Figure 10. The proportional mode of operation is alternately called gain. Gain is a multiplication term K expressing how the output from the controller will vary with respect to a change in the error signal. The optimal gain setting for the profiles desired in these tests was found to be 30.0-35.0, depending on the age and condition of the tungsten-filament lamps used in each test. Setting the gains too high causes large oscillations in the lamp output, drastically reducing an already shortened cyclic life of the lamps.

The integral mode, or reset, is used to correct steady state error (offset) by adding or subtracting from the output to correct for "droop" in the waveform caused by the proportional term. This reset value was set at 25.0 repeats per minute to correct for the offset in maximum (peak) temperature.

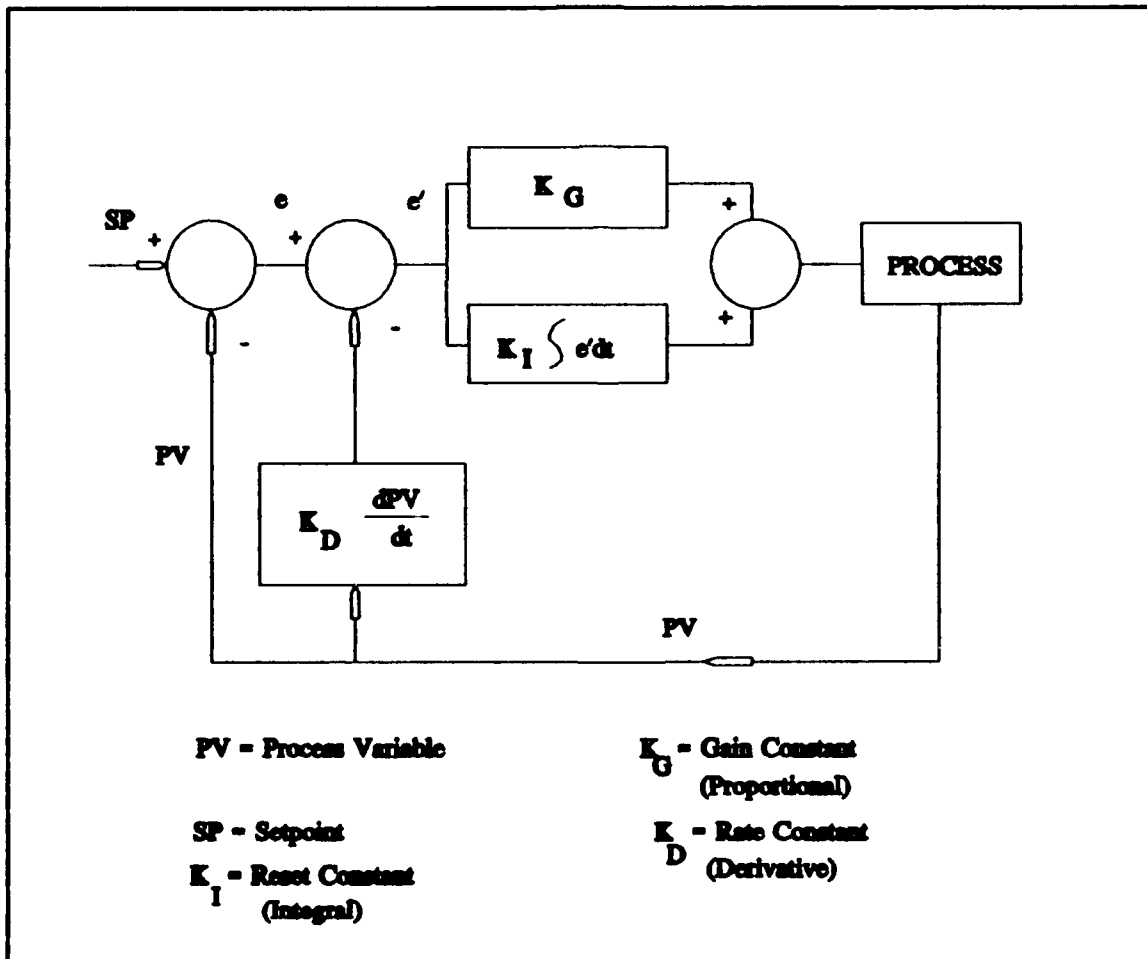


Figure 10. PID Control System for Micricon 82300

The derivative factor, or rate term, adjusts for the time lag in the system. This value can be adjusted from 0.0 to 8.5 minutes. Due to the length of the profiles proportional to any short lag in the system and the compensation by MATE263 for any phase lags, a rate value of 0.0 was used.

Temperature values were monitored directly from the Micricon through a direct link to the RS-232 port of the Z-248 Computer and were written to data files or used for correcting phase by the MATE program.

The final component of the thermal system consists of the water cooling system. Components of the test system require this water to prevent damage to instrumentation and equipment. The quartz lamps and hydraulic specimen grips used refrigerated distilled water pumped through them to prevent damage to the aluminum lamp cases and the load cell, respectively. A water conditioner cools the water after it has circulated through all the components and returns it to a holding tank. Figure 11 shows the water cooling system. A protective relay system has been installed in the holding tank to shut down the Micricon unit, and in turn the lamps, in case the water level drops below a safe level. The relay uses a cork float attached to a microswitch that closes under the float's weight when the water level drops.

iv. Strain Measurement Components. The strain measurement system is shown in Figure 12. A high temperature

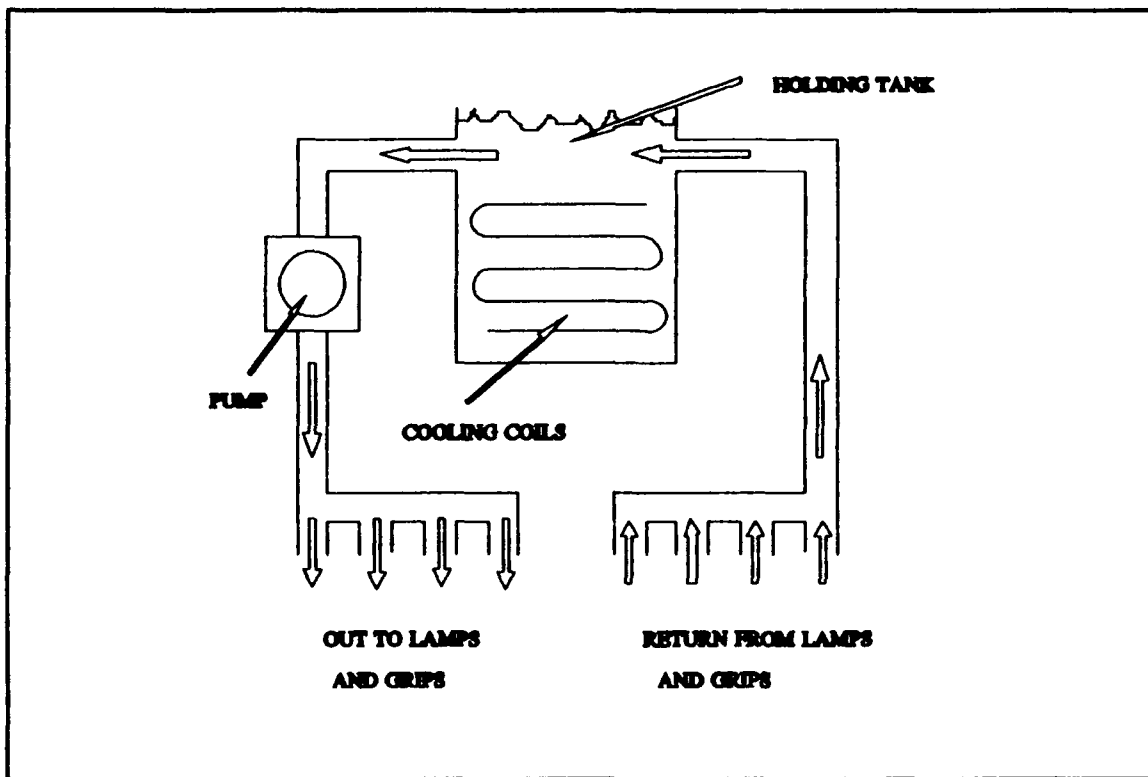


Figure 11. Water Cooling System

MTS extensometer was used to take displacement readings during the tests. This displacement reading is in the form of voltages in a linear  $+\text{-} 10.0$  Volts range. The total range of displacement possible in this voltage range was 2.54 mm in the 12.7 mm gauge length. The extensometer was equipped with conical tip quartz rods and was mounted in a specially designed holder mounted to the MTS main stand supports. This holding mechanism applies lateral pressure to hold the extensometer to the specimen while allowing the extensometer to "float" freely in the other degrees of freedom. The holder is also equipped with a baffled air cooling system to allow the extensometer protection from the high temperature test.

Actual displacements cause movement in the quartz rods which are connected to a metallic element in the extensometer equipped with strain gauges configured in a balanced Wheatstone bridge circuit. The displacement of the rods causes a voltage differential proportional to the displacements. This voltage reading can then be read manually on the data display or MTS microconsole. The MATE263 program is given a calibration factor for the extensometer from an MTS calibration device and actual gauge length prior to testing and therefore can read the voltages from the data display and convert these voltages to strain readings.

v. Specimen and Specimen Preparation. The specimen material used in this study was a  $[0/90]_{2s}$   $SCS_6/Ti-15-3$  metal matrix composite laminate. Ti-15-3 is a shortened designation for Ti-15V-3Cr-3Al-35N, a rather new metastable beta strip alloy. The laminate is formed using an isostatic hot-press of Ti-15-3 foils between layers of continuous silicon carbide fibers ( $SCS_6$ ) with a diameter of 0.136 mm (0.0054 in). The 330 mm X 330 mm (13 in X 13 in) 8-ply plates of material were manufactured by AVCC Specialty Metals, Textron Corporation. Thickness of the plates was 1.692 mm (0.0666 in) and had an average fiber volume ratio of 0.386 obtained by the area method using photomicrography of the sectioned specimens. Material properties for the individual fiber and matrix materials are given in Table I. (18:15)

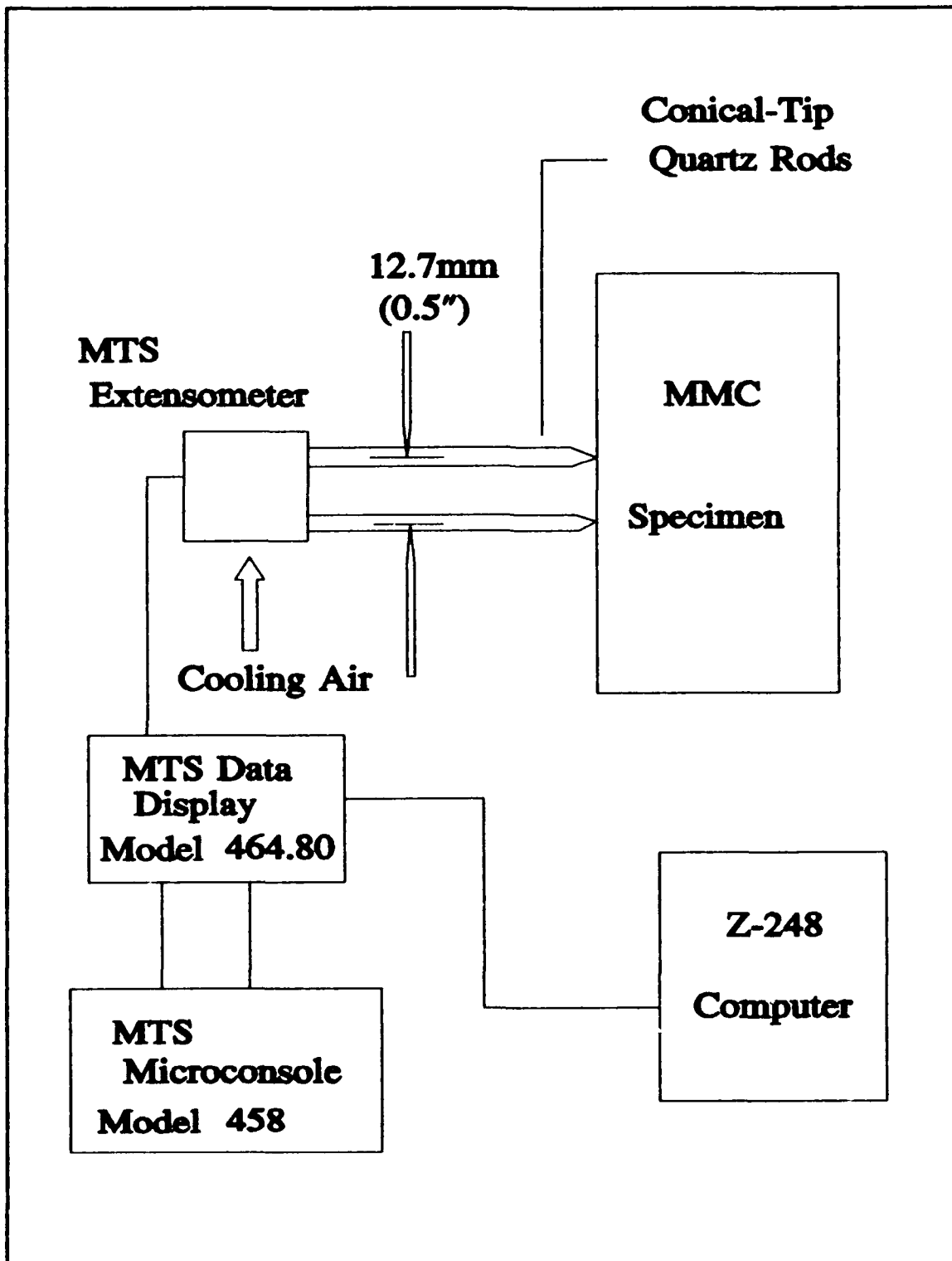


Figure 12. Strain Measurement System

The panels received from Textron were cut into 12.7mm (0.5 inch) by 165 mm (6.5 inch) rectangular specimens using a high pressure water injection system with a garnet abrasive (six specimens) or a diamond cut-off wheel (3 specimens). These cuts are diagrammatically shown in Figure 13. The only machining damage difference noted in the cuts was a slight tapering of the edges in the water injection case. Due to the fact that all specimens had to be ground on the edges to

Table I. Material Properties of Fiber and Matrix

	FIBER	MATRIX
Density (g/mm <sup>3</sup> ) (lb/in <sup>3</sup> )	3.045 x 10 <sup>-3</sup> 0.110	4.761 x 10 <sup>-3</sup> 0.172
Young's Modulus (GPa) (MSI)	400.00 58.00	62.07 9.00
CTE (mm/mm/ <sup>0</sup> C) (in/in/ <sup>0</sup> F)	4.9 x 10 <sup>-5</sup> 2.7 x 10 <sup>-6</sup>	9.7 x 10 <sup>-5</sup> 5.4 x 10 <sup>-6</sup>
Poisson's Ratio	0.250	0.350
UTS (MPa) (KSI)	3448.2 500.0	896.6 130.0

reduce irregularities, neither method was found to be initially more damaging to the materials. Because of the initial taper of the injection cut specimens, more time was required in grinding to reduce the tapered edges to a rectangular cross-section. The end result, through optical microscope examination, proved to be the same for each of the specimens. Specimen faces were left in the as-fabricated condition. The specimen edges were ground using successively finer grits of silicon carbide and then diamond slurry on a Maximet grinding platen. It was found that little grinding left the surface with minimal damage (discussed later) but was an insufficient surface to provide damage information through the replica technique. On the other hand, overpolishing made the surface too smooth to provide contrast, in replicas, between the fiber and matrix. The specimens were, therefore, polished using a 450 grit silicon carbide powder followed by 45, 15, and 3 micron diamond slurry to provide the optimal surface to serve both purposes. Photos in Figure 14 show optical photographs of the specimen after grinding but before testing. The quality of results by replica technique, described in detail in Chapter IV, was the guide to a properly polished specimen surface. Figure 15 shows photographs of replicas taken after thermal cycling showing thermal cycle edge crack damage. (A full summary of replica results is shown in Chapter IV.) Figure 16 shows an edge damage

schematic of the specimens following preliminary machining. Since optical photomicroscopy requires a highly polished specimen for best observations, the usual procedure is to section a small piece of a specimen and mount this piece in a hard thermoplastic for polishing and examination. Polishing specimens prior to testing did not allow for small polishing areas. Due to the size of the specimens and the difficulty in handling the specimen during polishing, the surfaces prior to testing were less than ideal, but sufficient for preliminary examination. In Figure 14, scratches can be noted in the matrix between fibers. This is caused by the softer matrix material being ground away faster than the surrounding fibers by the diamond slurry. The harder fibers cause a channeling effect with the slurry around their surfaces and the diamonds reduce the matrix material. These scratches are an inconvenience but observations of any damage occurring during tests was easily discernable despite the scratches in both optical photos of the specimens directly and replica observations.

Baseline damage in the specimens consisted of two main forms. First was the  $0^\circ$  fibers which may not have been perfectly parallel to the cut surfaces. These fibers show as a tapered point on the edge of the specimen and are a primary point of thermal edge damage initiation. Internal examination of the specimens later showed no propagation of these

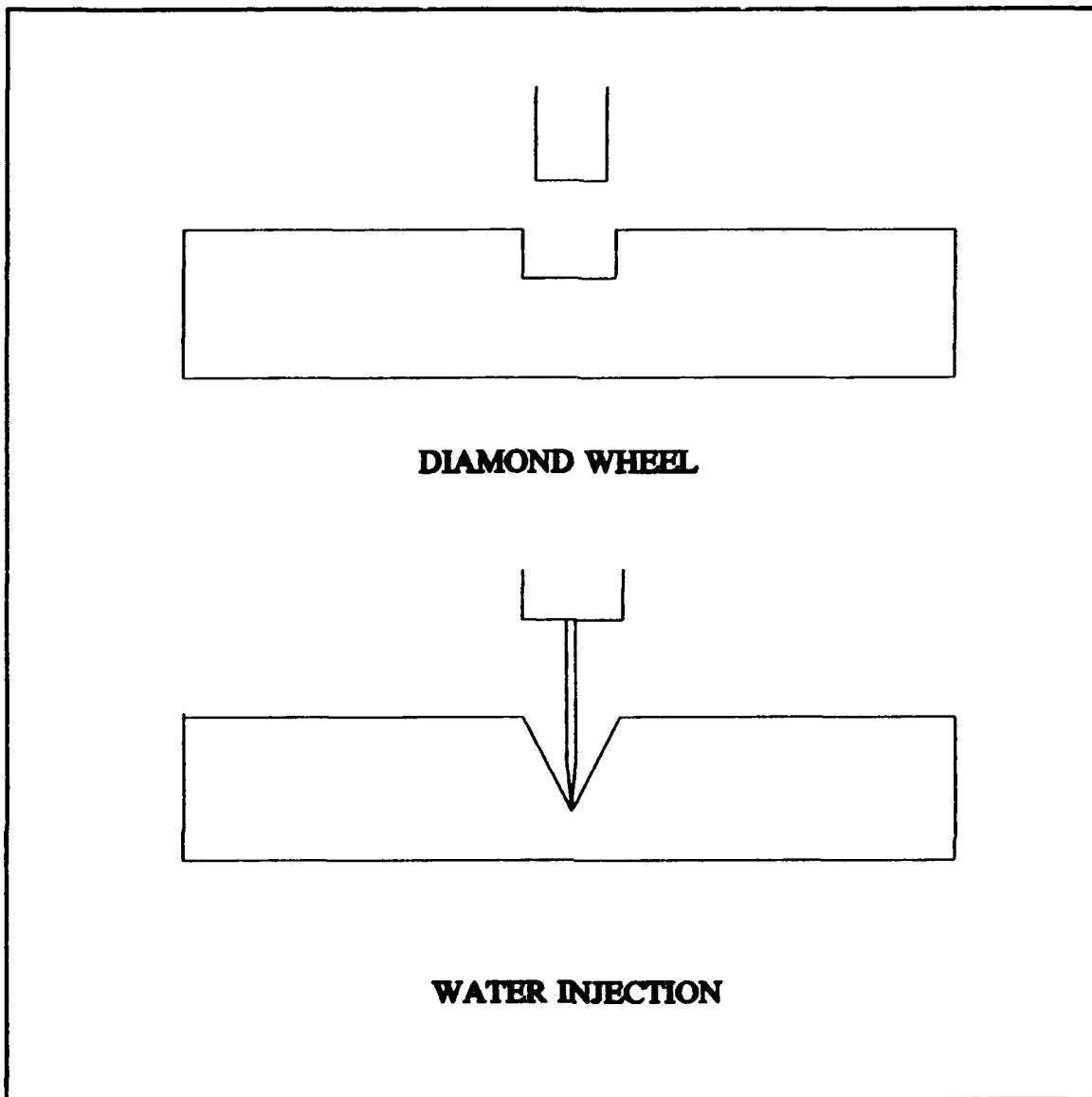


Figure 13. Water Injection vs. Diamond Machining

thermally generated cracks toward the inside of the specimen and therefore this type of thermal edge crack can be assumed to be confined to the edges. Second,  $0^\circ$  fibers were pulled out or broken during the cutting process leaving a cross-section of the fiber or a groove where the fiber originated. No significant damage other than as-fabricated uneven spacing

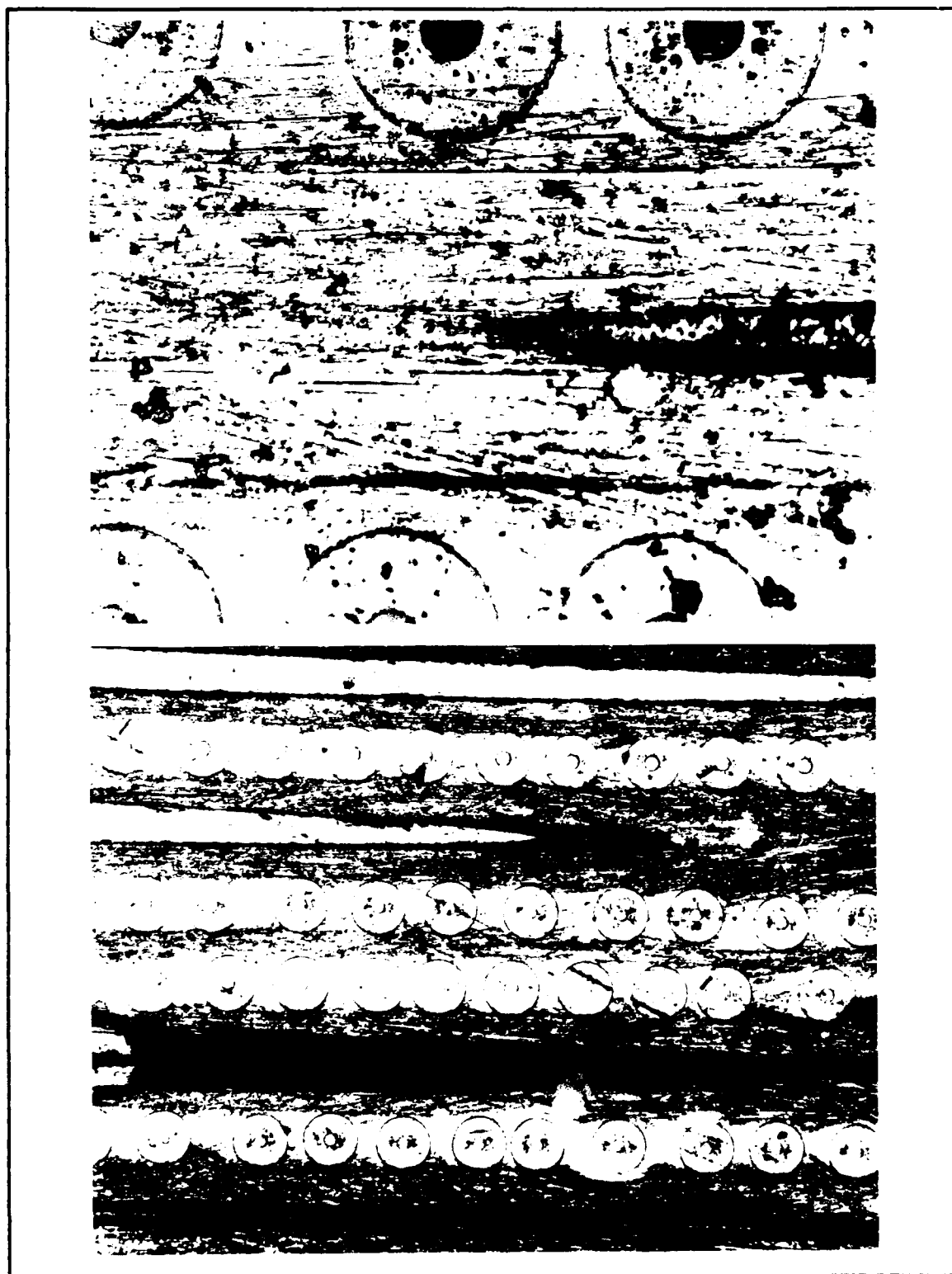


Figure 14. Uncycled Specimen Edge

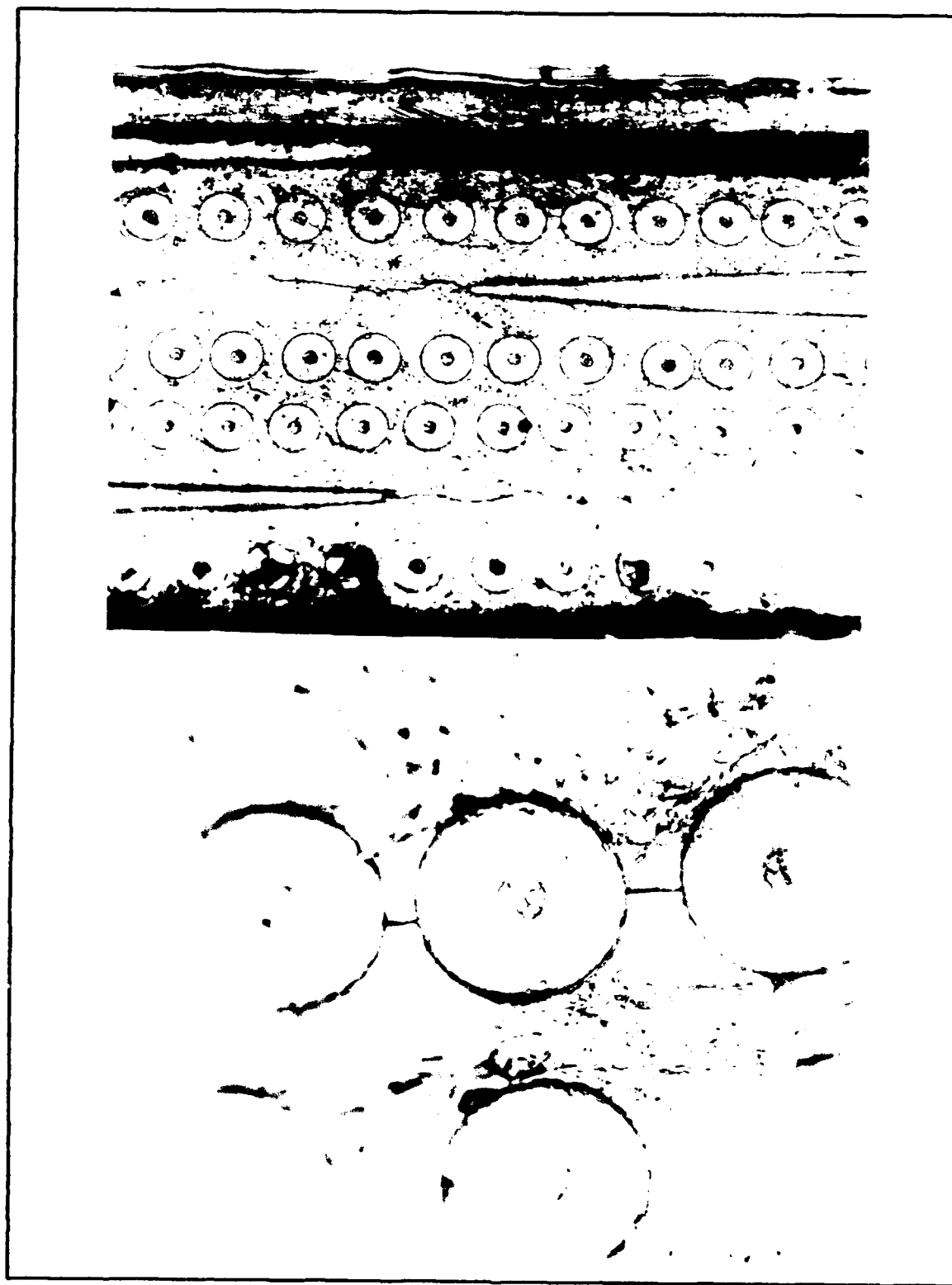


Figure 15. Replica Photos of Specimen after Thermal Cycles

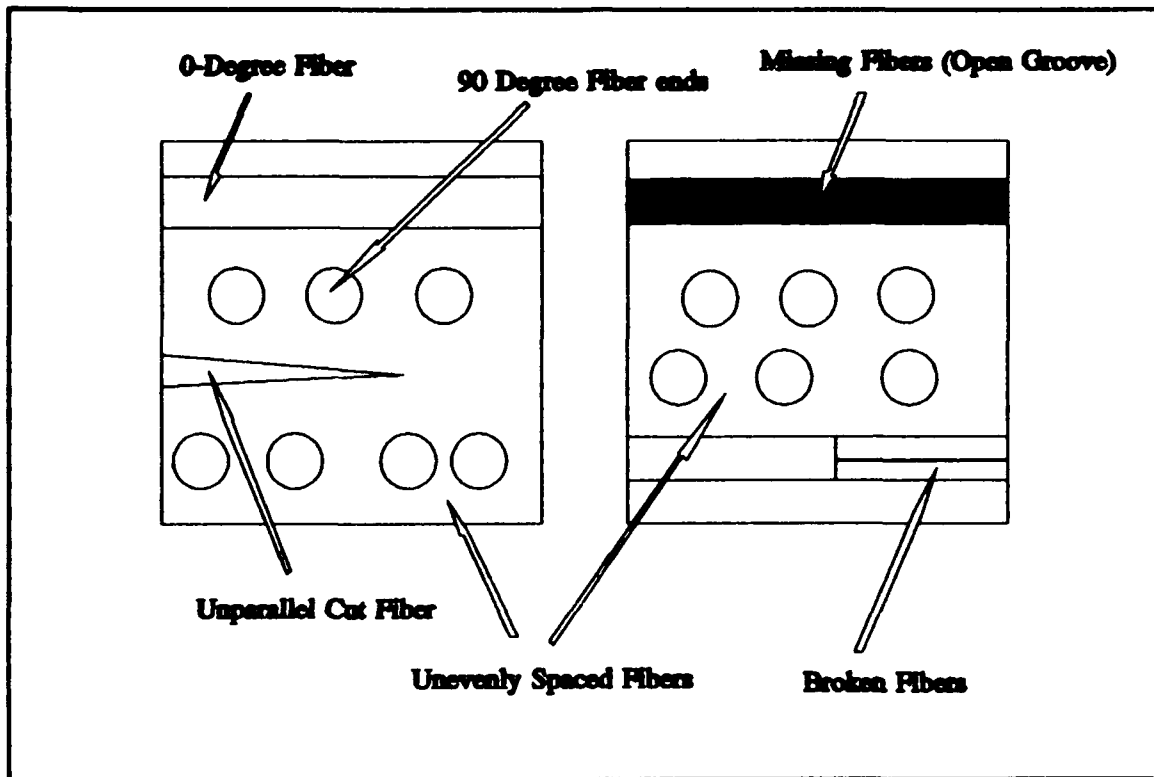


Figure 16. Edge Damage Schematic (After Preparation before TF)

between fibers was found in the  $90^{\circ}$  ply after grinding. Refer to Figure 14 illustrating the laminate surface after grinding. Figure 16 shows the schematic of the typical edge flaws found after polishing the specimens. A specimen diagram is given in Figure 17 showing dimensions and thermocouple locations.

The properties for fiber and matrix given in Table I were used in conjunction with a fiber volume ratio ( $V_f$ ) of 0.4 and ply thickness of 0.2302 mm (.008 in) (18:15) to provide an initial estimate of first ply failure (FPF) for the specimens. For the estimate, fiber modulus was assumed to be relatively constant throughout the temperature range used in the tests.

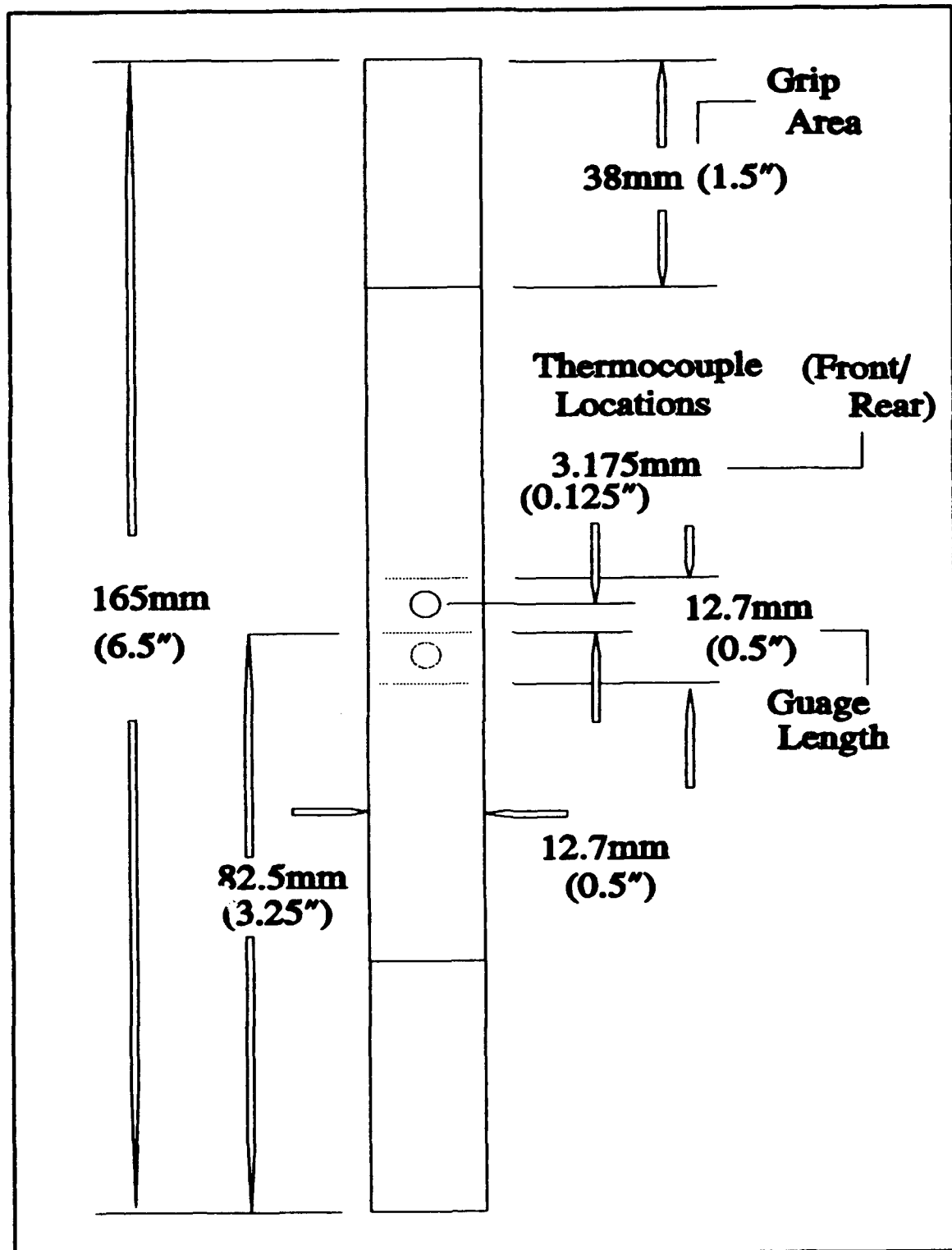


Figure 17. MMC Specimen

A matrix modulus was used which gave a longitudinal modulus  $E_{11}$  which matched closely the initial ambient modulus observed in the thermal fatigue experiment. Bonding between the matrix and fiber was assumed perfect and any analysis to be performed up to FPF was assumed linear.

SDRC-IDEAS (34), a finite element model builder and analysis code was used to generate a simple rectangular grid model of the laminated specimen. Properties in Table I and those given in this paragraph were used by the program to compute ply and, in turn, laminate properties to be used by MSC/NASTRAN (25) in computing individual ply stresses. The method employed by IDEAS is simply rule-of-mixtures calculations for individual lamina and basic laminate theory for combining these lamina in laminate form.

SDRC-IDEAS is capable of generating input data output files which are directly compatible with MSC/NASTRAN codes. The linear analysis module (more specifically solution 24 (SOL24) with an RFALTER statement RF24D79) of MSC/NASTRAN was used to compute individual ply stresses for the laminate. A unit load was applied to the specimen model and the resultant stress distribution in the plies was determined. A 379 MPa (55 KSI) stress was shown by Johnson (16:16) to cause failure in a  $[90]_8$  lay-up specimen. This value was used as a FPF stress criteria by incrementing the applied unit load and calculating the resultant  $90^\circ$  ply stress until this threshold

was reached. The final FPF value estimate was 490 MPa (71 KSI) applied stress. This stress level was then used in planning load levels for the subsequent fatigue tests.

The MMC specimen was then mounted in the MTS stand and the thermocouples were welded in the gauge length. The extensometer mount was adjusted such that the extensometer was pressed against the edge of the specimen at a gauge length of 12.7 mm. (The extensometer is zeroed at 12.7 mm prior to affixing it to the specimen using micrometer measurements. The extensometer is then adjusted on the specimen to be as close as possible to this zero voltage. Any offset voltage was then recorded.) The extensometer was then allowed to settle on the specimen and when displacement voltage settled to a constant voltage readings of actual gauge length and offset strain voltage were taken from the MTS microconsole display. This offset is then conveyed to the MATE program when the user is prompted for actual gauge length. The offset voltage was recorded and is used when reducing the final strain readings for analysis. The lamps were then adjusted to heat the proper areas of the specimen.

After these adjustments, a manual modulus test was conducted on each of the specimens just prior to testing. This was accomplished by incrementally increasing load level and taking displacement voltage readings from the microconsole.

At this point the MATE program was initiated and specimen data (measurements, requested load level, load ratio, profile characteristics, etc.) are conveyed to the program. The program starts thermal cycles first and allows the thermal cycles to stabilize and allows the user to make fine adjustments with the lamps. At this point (3 to 6 cycles) the user initiates the mechanical loading cycle. The specimen was cycled at the designated load, stopping at 250, 500, 1000, 1500, 2000, 2500, 3000, and each subsequent 1000 cycles to examine the specimen by replica.

The replica technique involved putting the test system on hold, cooling the specimen to ambient conditions, and without disturbing the specimen or extensometer, the forward lamp was swung out and the specimen is soaked with a coat of acetone. Before the acetone can evaporate, a thin sheet of acetate paper is pressed to the surface of the specimen and an impression of the surface is left in the transparent paper. These impressions can then be observed under the microscope to determine damage without removing the test specimen from the test machinery. It was found to be advantageous to apply a small load to the specimen to open existing cracks and make them more visible in the replicas.

#### IV. Results and Discussion

##### A. Test Results Summary

Nine tests were conducted on the  $[0/90]_{2S}$  SCS<sub>6</sub>/Ti-15-3 composite using the thermomechanical fatigue (TMF) system. A single test under each condition was performed due to scarcity of the material. The test matrix is shown in Figure 18. The system proved capable of maintaining a consistent test temperature range of  $149^{\circ}\text{C}$ - $427^{\circ}\text{C}$  ( $300^{\circ}\text{F}$ - $800^{\circ}\text{F}$ ) for all tests and all in-phase (I-P) and out-of-phase (O-P) tests were conducted at a load ratio (R) of 0.1.

The first experiment measured thermal strains and coefficient of thermal expansion (CTE) for the material under thermal cycling. These parameters were later used for test data reduction in distinguishing mechanical strains from total strains. The specimen cycled under thermal-only conditions showed no signs of property degradation up to 10,000 cycles and maintained a constant CTE after initial strain stabilization. In fact, during a subsequent residual strength test, the specimen demonstrated a higher modulus (9.3% higher), more linear stress-strain curve and a higher ultimate tensile strength (12.5% higher) than ambient or  $427^{\circ}\text{C}$  tensile tests on uncycled specimens. Figure 19 shows the results of these tests. This topic will be discussed in the strain measurement section of this chapter. Four tests were

## TEST MATRIX

	MAXIMUM STRESS in MPa (KSI)					
	0	244 (35)	293 (43)	367 (54)	441 (63)	612 (88)
Thermal-Only (No Load)	X					
In-Phase		X		X *	X *	X *
Out-of-Phase			X	X *	X *	X *

**X \* - TESTS COMPLETED TO FAILURE**

(All tests performed under applied Tension-Tension conditions, R=0.1, f=0.02 Hz,  
149-427 degrees C)

**Figure 18. Experimental Test Matrix**

conducted under in-phase (IP) and four under out-of-phase (OP) TMF conditions.

Using the predicted first-ply failure strength calculated by MSC/NASTRAN (see Specimen Preparation section Chapter III),

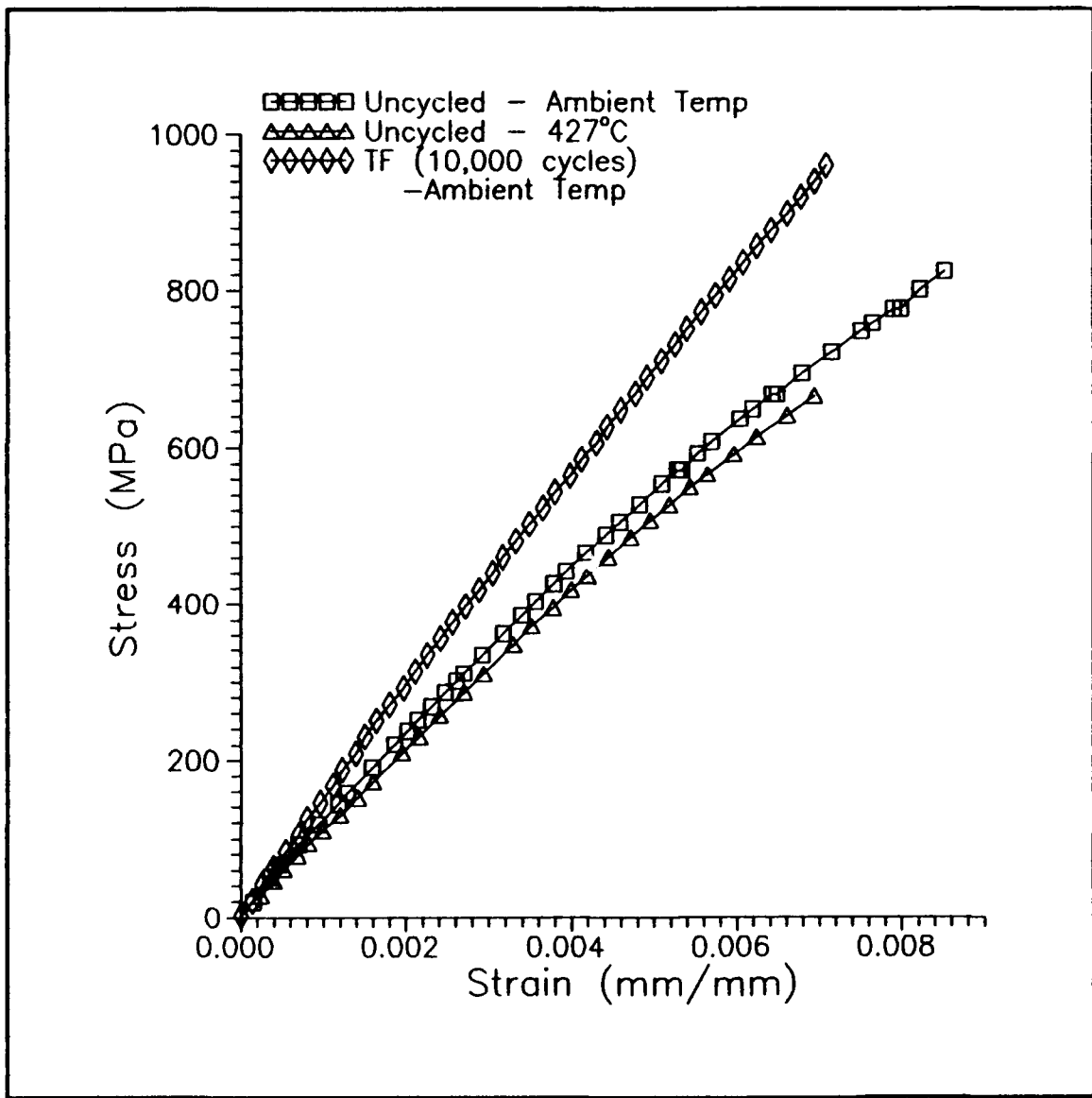


Figure 19. Tensile Test Stress-Strain Curves

a first stress level of in-phase testing was selected to be equal to 50% of the predicted first-ply failure strength, 490 MPa (71 KSI). (Tensile tests performed later on this batch of material showed 550 MPa (80 KSI) to be the knee (i.e. point of nonlinearity) in the stress strain curve at ambient conditions and 450 MPa (65 KSI) at 427°C (800°F), indicating yielding or

PPF. Up to 10,000 cycles there was no edge damage other than longitudinal cracking due to thermal cycling, the test was stopped and the specimen was saved for later use. After conclusion of the remaining tests, this specimen was again tested. A few transverse cracks were observed, but there was no further major damage or failure up to 30,000 cycles. Three remaining in-phase tests were conducted at 75%, 90%, and 125% of the predicted FPF strength. These specimens failed at 28,900, 3069, and 180 cycles, respectively. Four subsequent out-of phase tests were conducted at 125%, 90%, 75%, and 60% FPF strength. The first three tests failed at 775, 3875, and 5534 cycles, while the last one did not fail up to 30,000 cycles. This last test suffered much more edge damage than the 50% in-phase test and it can be assumed that this test (with enough time) would eventually fail. Most of the discussion of this study will center on the six specimens which failed within a reasonable period. The other two had to be stopped due to the time constraints associated with this master's thesis. (Note: 30,000 cycles = approx. 3 weeks test time). Figure 20 shows the resulting S-N curves (maximum applied stress vs # cycles at failure).

Prior to the testing of each specimen, the Young's Modulus was measured. This test was conducted by manually incrementing load to a limit of approximately 20% of FPF (100 MPa) and strain was recorded at each level to provide stress-

**Table II. Initial Modulus Measurements**

Applied Stress	Phase	Initial Modulus
75% - 367 MPa	In-Phase	134.37 GPa
75% - 367 MPa	Out-of-Phase	132.00 GPa
90% - 441 MPa	In-Phase	130.27 GPa
90% - 441 MPa	Out-of-Phase	139.50 GPa
125% - 612 MPa	In-Phase	136.34 GPa
125% - 612 MPa	Out-of-Phase	131.72 GPa

strain curves. Young's Modulus was then measured from the slope of a linear curve fit to these curves. An average initial modulus for the six failed specimens was 134.03 GPa (19.43 MSI). See Table II for a compilation of these modulus measurements. Ambient modulus was also measured whenever the tests were put on hold by the computer software at user-selected intervals to take replicas of the specimen surface. This procedure was to double-check the instantaneous modulus calculated from strain measurements taken by the computer software. Similar to Johnson's (16:7) observations, the first cycle of each specimen showed a nonlinearity in the loading slope. This slope with few additional cycles became linear, but with a slightly decreased modulus (3-4%). It is believed this initial loading caused a relaxation of residual stresses developed during manufacturing. All in-phase specimens,

during tests, showed a linear applied stress vs. mechanical strain curve after a few cycles, which was about 6 to 12. Out-of-phase specimens demonstrated an open hysteresis strain loop which was heavily dependent on phase conditions and applied stress magnitude.

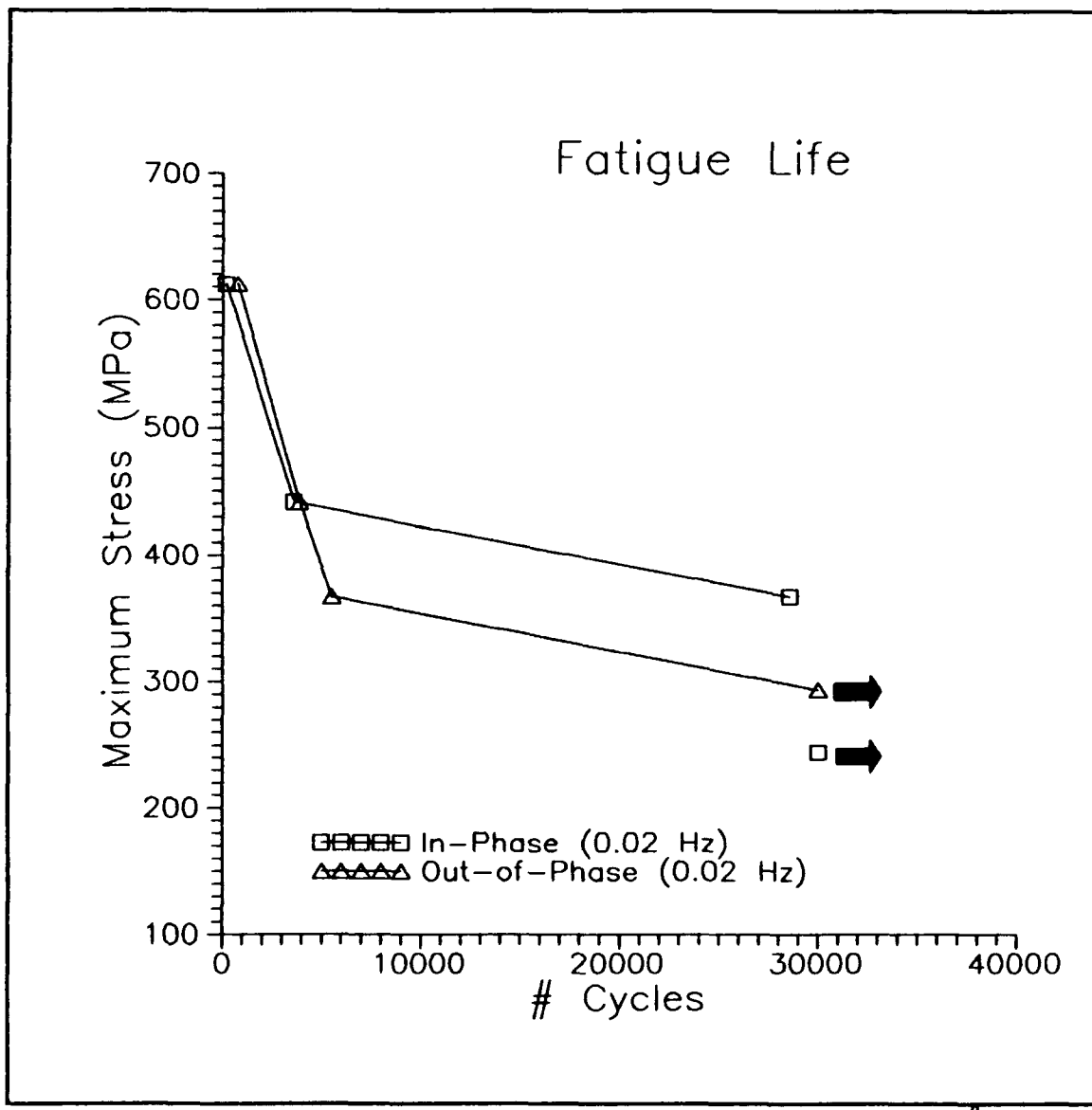


Figure 20. IP and OP Fatigue Life (0.02 Hz - 149-427°C)

## B. Thermal Strain and CTE Test

To provide for thermal-only (no load) test conditions, the MATE263 program was used to command a  $149^{\circ}\text{C}$ - $427^{\circ}\text{C}$  ( $300^{\circ}\text{F}$ - $800^{\circ}\text{F}$ ) temperature profile from the Micricon unit. Since the extensometer is laterally loaded against the edge of the specimen, the specimen must be gripped by the test stand at both top and bottom. But, because the specimen must be free to expand and contract under the thermal load, the bottom grip actuator control had to be able to maintain a constant load condition on the specimen. Optimally desired conditions would have been zero load control. The MATE program, though, controls load and temperature cycles through phase conditions and must sense peak load and temperature to properly control profiles for testing. Therefore, a minimal load with  $R=0.9$  was used instead of no load. This load condition at no time exceeded 3% of a predicted first ply failure criteria predicted through MSC/NASTRAN using Johnson's ambient experimental data and basic laminate theory.

An initial load level of 50 MPa, which was 0.1 of predicted first ply failure was applied to a stainless steel specimen and incrementally decreased to determine when the noise level in the 4000 lb load card for the MTS Microconsole would prevent the MATE program from accurately finding peak load and temperatures. It was determined that a 135 N (30 lb) at  $R=0.9$  load level on a similar sized specimen was sufficient

for this purpose and this corresponded to a stress level of 6.2 MPa or 900 psi (1.2% FPF).

This first specimen, subjected to thermal cycling only, showed a slight increase in mean strain over approximately the first 20 cycles and then remained at a constant level for the remainder of the test. This was typical in each of the low load tests (tests below predicted FPF). Strain range ( $\Delta\epsilon_t$  - delta thermal strain) also remained constant for the test indicating a constant CTE for the material during the first 10000 cycles of testing. Average maximum strains of .002676 mm/mm and average minimum strains of .000839 mm/mm were recorded and then used throughout this study to calculate CTE and, in turn, thermal strains encountered in each of the tests. Strain results from testing gave a calculated CTE value of  $6.608 \times 10^{-6}$  mm/mm/ $^{\circ}$ C ( $3.674 \times 10^{-6}$  in/in/ $^{\circ}$ F). METCAN predictions gave a value of  $6.442 \times 10^{-6}$  mm/mm/ $^{\circ}$ C ( $3.582 \times 10^{-6}$  in/in/ $^{\circ}$ F) - a difference of 2.5%.

For reduction of resulting mechanical and thermal strains from total strains in the tests, a linear sum relationship of thermal and mechanical strains to total strain was assumed for in-phase and out-of-phase tests. Therefore, to calculate modulus for any given cycle (assuming linear stress-mechanical strain curves) can be computed from the following strain relationship:

$$\epsilon_T = \epsilon_t + \epsilon_m \quad (5)$$

In the case of in-phase testing, the  $\Delta\epsilon_t$  is subtracted from total strain ( $\Delta\epsilon_T$ ) to determine mechanical strain ( $\Delta\epsilon_m$ ). For out-of-phase tests the  $\Delta\epsilon_t$  must be added back to  $\Delta\epsilon_T$  to determine  $\Delta\epsilon_m$  due to the cancellation effect in the out-of-phase cycle. The Young's Modulus can then be computed by the following basic relation:

$$E = \frac{\Delta\sigma_{\text{applied}}}{\Delta\epsilon_{\text{mechanical}}} \quad (6)$$

Edge damage noted for the thermal-only fatigue (TF) specimen consisted of longitudinal cracking from cut 0° fiber tips in the 0° plies at around 1500 cycles and cracks between 90° fiber ends parallel to the specimen length at 3500 cycles. This longitudinal edge damage was confined to the edge of the specimen, while in TMF tests transverse edge cracking was an indicator of internal damage which will be discussed later in Section E. of this chapter. Internal transverse cracks initiated at fiber-matrix interfaces and progressed outward through the 90° ply matrix to the surface of the edge, and even on the face, of the specimens with increased time. See

Figure 21 for a schematic of edge damage initiation modes and the corresponding cycle number for all tested specimens.

Initial changes in mean strain can probably be attributed simply to a stabilization of the thermal and residual stress gradients in the specimen upon test startup and settling to a constant value before it reaches a stable value. See Figures 22 and 23 for examples of this strain increase in low-load in-phase tests.

### C. Strain Measurements

Table III gives a summary of maximum failure strains (total strains) for the six tests taken to failure. Table IV summarizes maximum mechanical strains (total strain less thermal strains) for the six tests taken to failure.

Strains for the 75% FPF IP/OP and 90% FPF IP tests displayed four distinct trends. Firstly, for about 20 cycles, there was strain stabilization as shown in Figures 22 and 23. Second, these tests exhibited a creep-rachetting effect over approximately the next 1000 cycles which had a relatively rapid mean strain increase. This effect may be due to the relatively long 48 second cycles used for the in-phase tests. This slow loading with peak load at peak temperature may be causing a creeping effect, but the characteristic is exhibited at low loads by the O-P tests also. Note the dramatic trend shown for the 75% FPF O-P test in Figure 24. This increase in

## EDGE DAMAGE INITIATION SUMMARY

Replicas were taken at 250, 500, 1000, 1500, 2000, and each subs. 1000 cycles)

TF	~ 1500	~ 3500	N/O	N/O
I-P 244 MPa (35 KSI)	~ 250	~ 250	~ 250	N/O
I-P 367 MPa (54 KSI)	~ 250	~ 250	~ 250	~ 9000
I-P 441 MPa (63 KSI)	~ 250	~ 250	~ 250	~ 3000
I-P 612 MPa (88 KSI)	~ 140	~ 140	~ 140	N/O
O-P 293 MPa (43 KSI)	~ 500	~ 1000	~ 1000	~ 1000
O-P 367 MPa (54 KSI)	~ 500	~ 1000	~ 1000	~ 1000
O-P 441 MPa (63 KSI)	~ 500	~ 1000	~ 1000	~ 500
O-P 612 MPa (88 KSI)	N/O	N/O	~ 500	~ 500

N/O - NOT OBSERVED DURING TEST

Figure 21. Edge Damage Summary

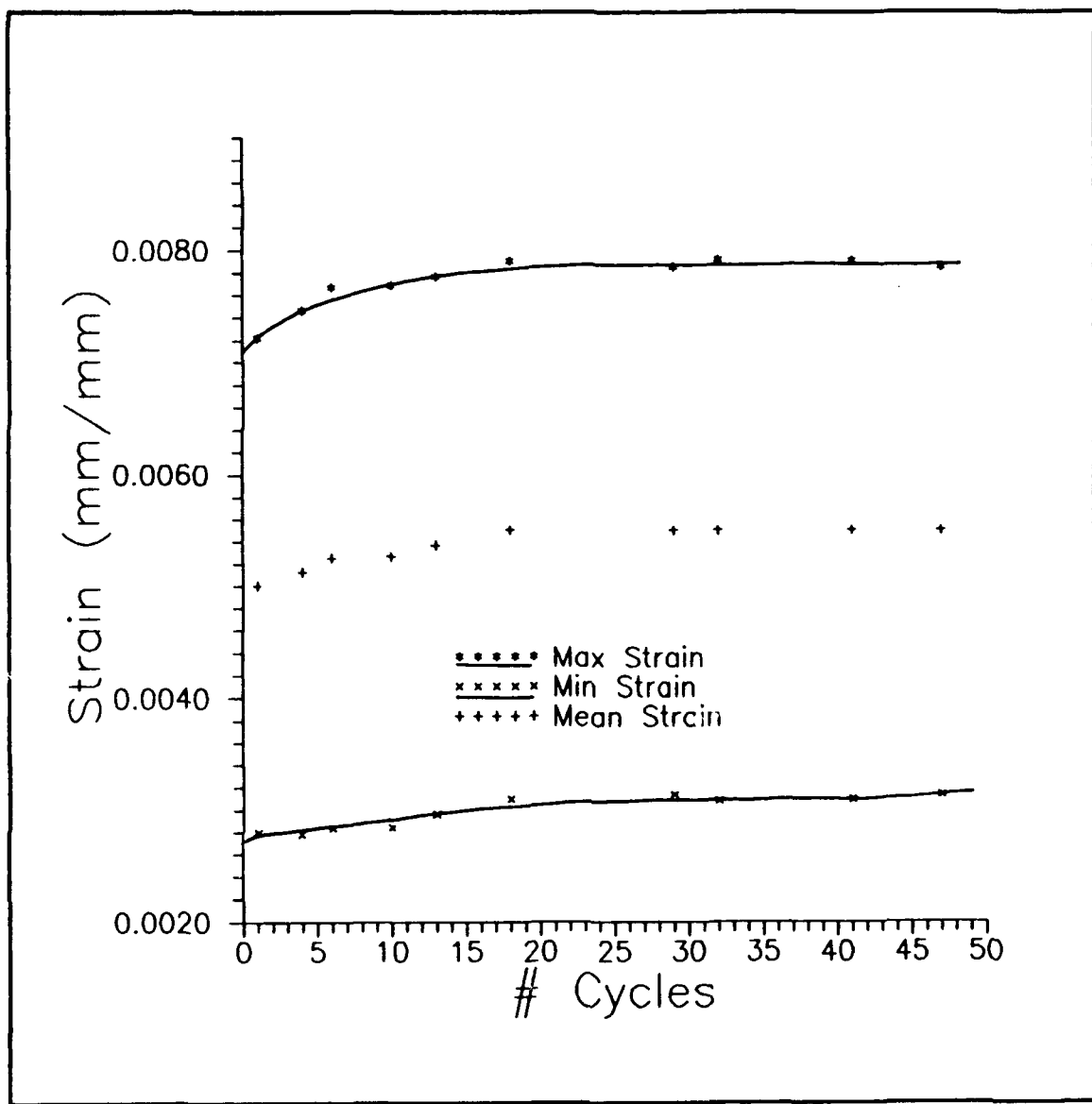


Figure 22. Strain Stabilization for 441 MPa In-Phase Test

strain may be due to an initial form of damage or a stress relaxation of the composite material due to load alone. Thirdly, the tests' strain rate levels or slowed per cycle, and steadily increased until rapidly climbing to failure strain near the last two percent of life. See Figures 25 and 24 for strain plots of the 90% FPF I-P and 75% FPF O-P tests.

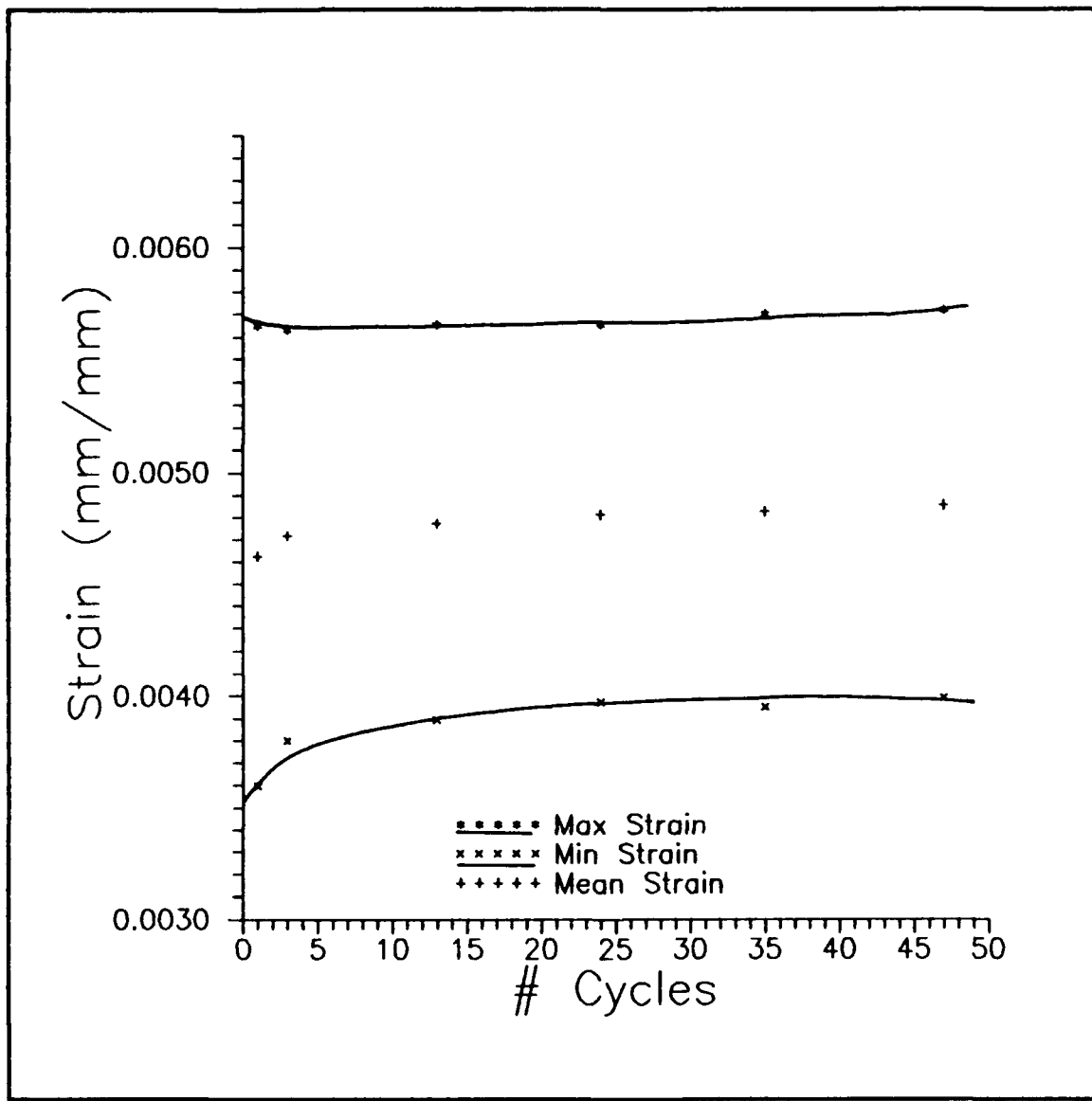


Figure 23. Strain Stabilization 441 MPa Out-of-Phase Test

The 90% FPF O-P (Figure 26) and 125% FPF I-P/O-P (Figures 27 and 28) tests exhibit a more definitive increase to failure throughout the tests. These higher load test curves show a dramatic initial increase in strain (first several cycles) followed by a relatively steady increase in strain to failure with no dramatic changes in strain rate progression. The

**Table III. Failure Strain Summary - Total Strains**

TEST	# Cycles to Failure (N <sub>f</sub> )	Max <sup>2</sup> Strain @ Failure (mm/mm)*
367 MPa I-P	28,900	.008590
441 MPa I-P	3,069	.012046
612 MPa I-P	180	.010069
<u>Average</u>		.010235
367 MPa O-P	5,534	.008201
441 MPa O-P	3,875	.007532
612 MPa O-P	775	.008625
<u>Average</u>		.008119

\* Maximum Strains Reported Are For 0.98N<sub>f</sub>

higher load tests showed a strain increase trend over the first phase of life but instead of slowing to a steady strain rate for the greater part of life, the tests display a steady increase to failure with no dramatic strain increases immediately before failure. Representative stress-strain hysteresis loop data is shown in Appendix C.

Failure maximum strains for the I-P tests tend to average around 1.0% while O-P tests exhibited average failure maximum strains almost 20% lower at 0.8%. It might be surmised at this point that the I-P tests were undergoing more plastic deformation prior to failure than were the O-P tests. This in turn could mean matrix, or fiber-matrix slippage,

**Table IV. Failure Strain Summary - Mechanical Strains**

TEST	# Cycles to Failure (N <sub>f</sub> )	Max <sup>a</sup> Strain @ Failure (mm/mm)*
367 MPa I-P	28,900	.005914
441 MPa I-P	3,069	.009370
612 MPa I-P	180	.007393
		<u>Average .007559</u>
367 MPa O-P	5,534	.007362
441 MPa O-P	3,875	.006693
612 MPa O-P	775	.007786
		<u>Average .007280</u>

\* Maximum Strains Reported Are For 0.98N<sub>f</sub>

demonstrating higher ductility, could be the damage mechanisms for these tests. The O-P tests, in general, exhibited much less plastic behavior and showed a brittle type of final failure strain rate (i.e. no rapid increase in strain near final failure.) This may tend to show progressive matrix material failure throughout the majority of fatigue life for the specimens and fiber domination during final damage progression and failure. After removing thermal strains from total strain at failure, it was found that average mechanical strains at failure for both in-phase and out-of-phase tests were within 5% of one another. This showed that the higher total strain values at failure for in-phase tests were

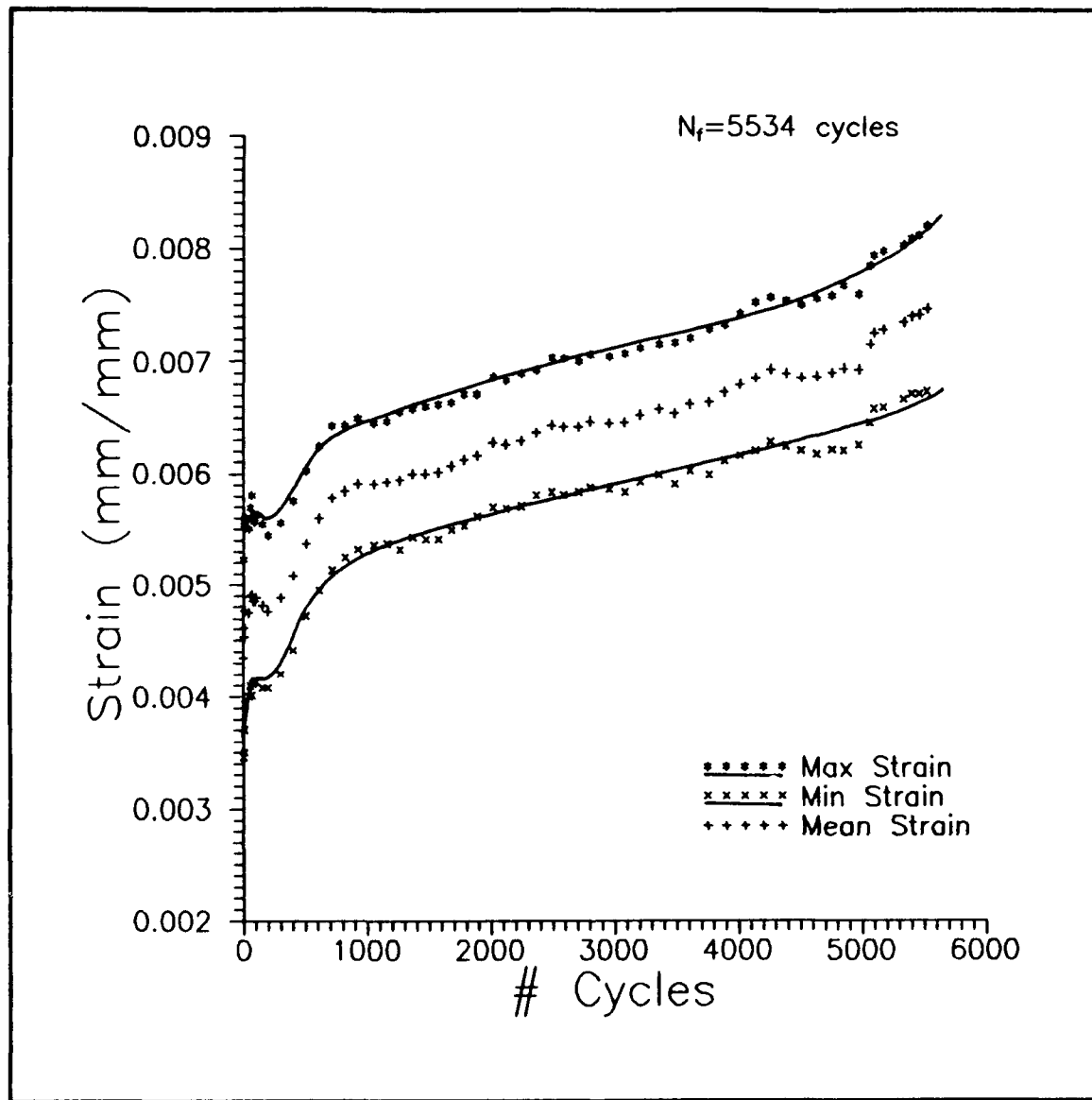


**Figure 24.** Strain Data for 367 MPa Out-of-Phase Test

probably due to higher thermal strains at peak load and not necessarily to higher plastic deformation. This association demonstrated a maximum strain parameter for failure of the composite of approximately  $\epsilon_u = 0.0075$ .

One problem was encountered during testing concerning strain measurements. Early in the testing sequence (75% FPF

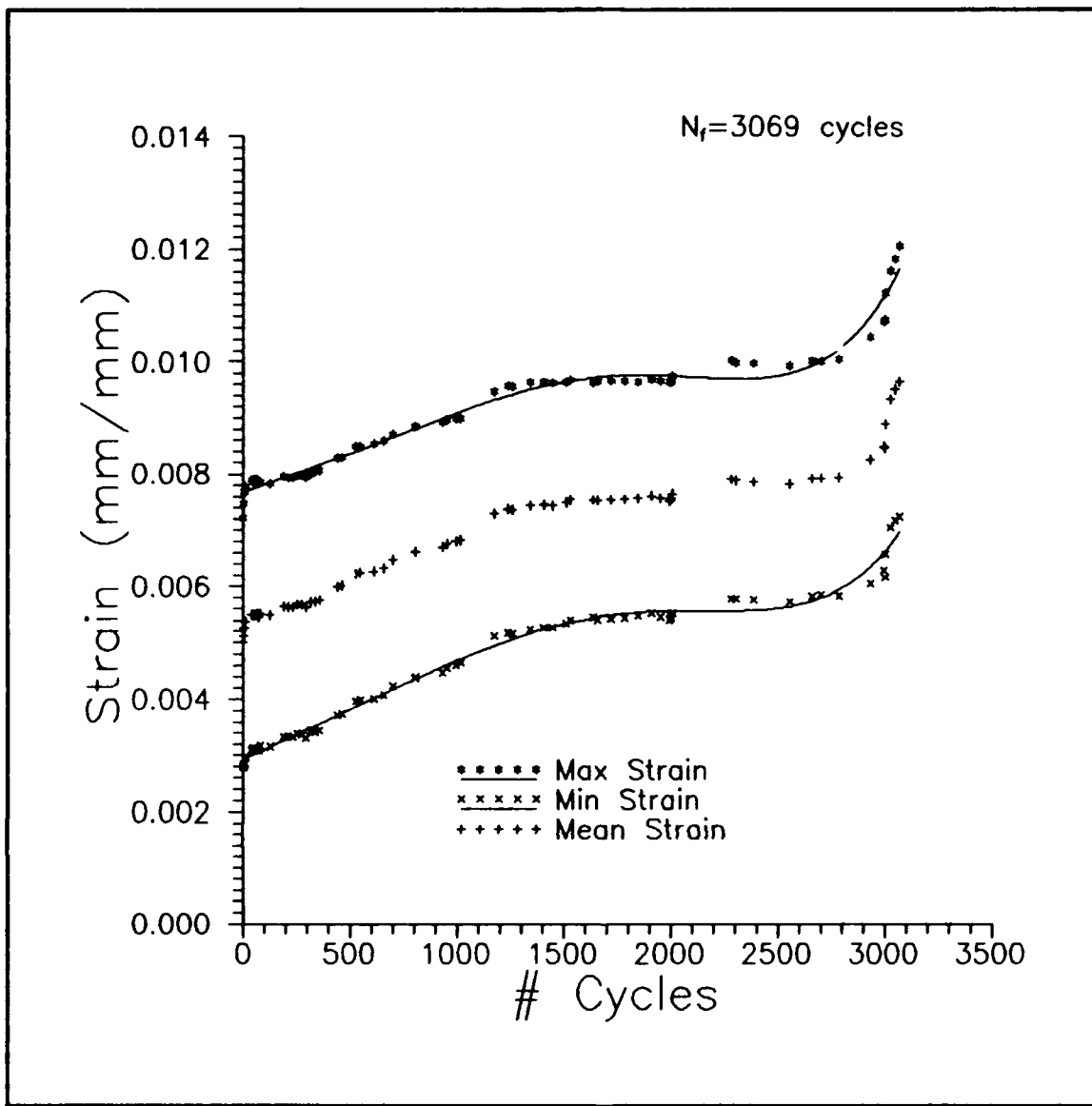


Figure 25. Strain Data for 441 MPa In-Phase Test

I-P) a strain drift at low loads was noted. This drift was cyclic in nature and made one complete cycle each day. It was concluded through monitoring room temperature that the drift was coinciding with night and day temperatures when the room temperature control allowed variations in excess of  $5^{\circ}$  C. The specimen temperature was not varying with room temperature and

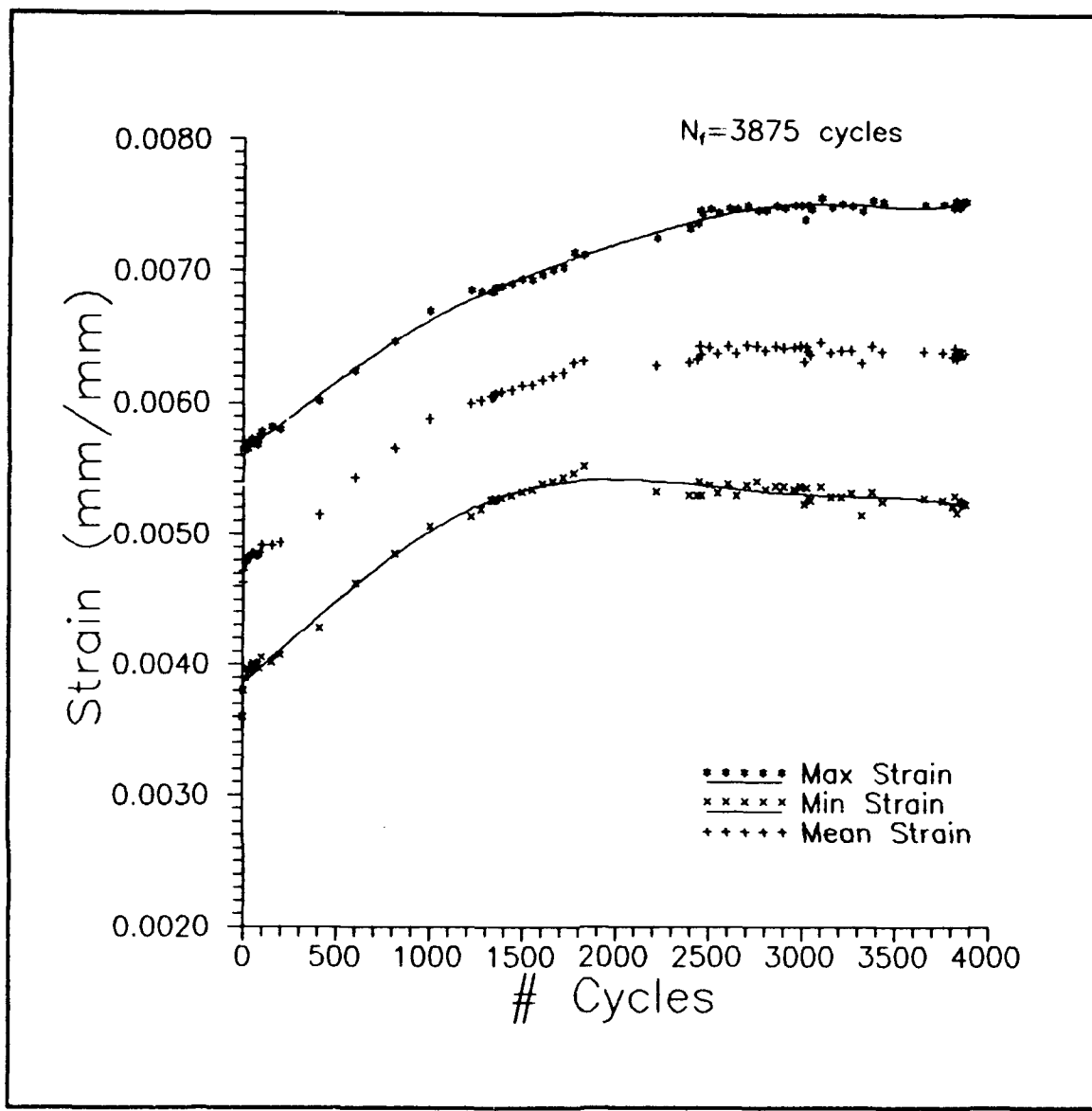


Figure 26. Strain Data for 441 MPa Out-of-Phase Test

manufacturer's specifications on all equipment guaranteed against such small deviations in temperature. Grips and lamps were cooled with temperature-controlled water. The only component unmonitored for temperature was the high temperature extensometer. Air being used to cool the extensometer came from compressed house air and temperature varied from day to

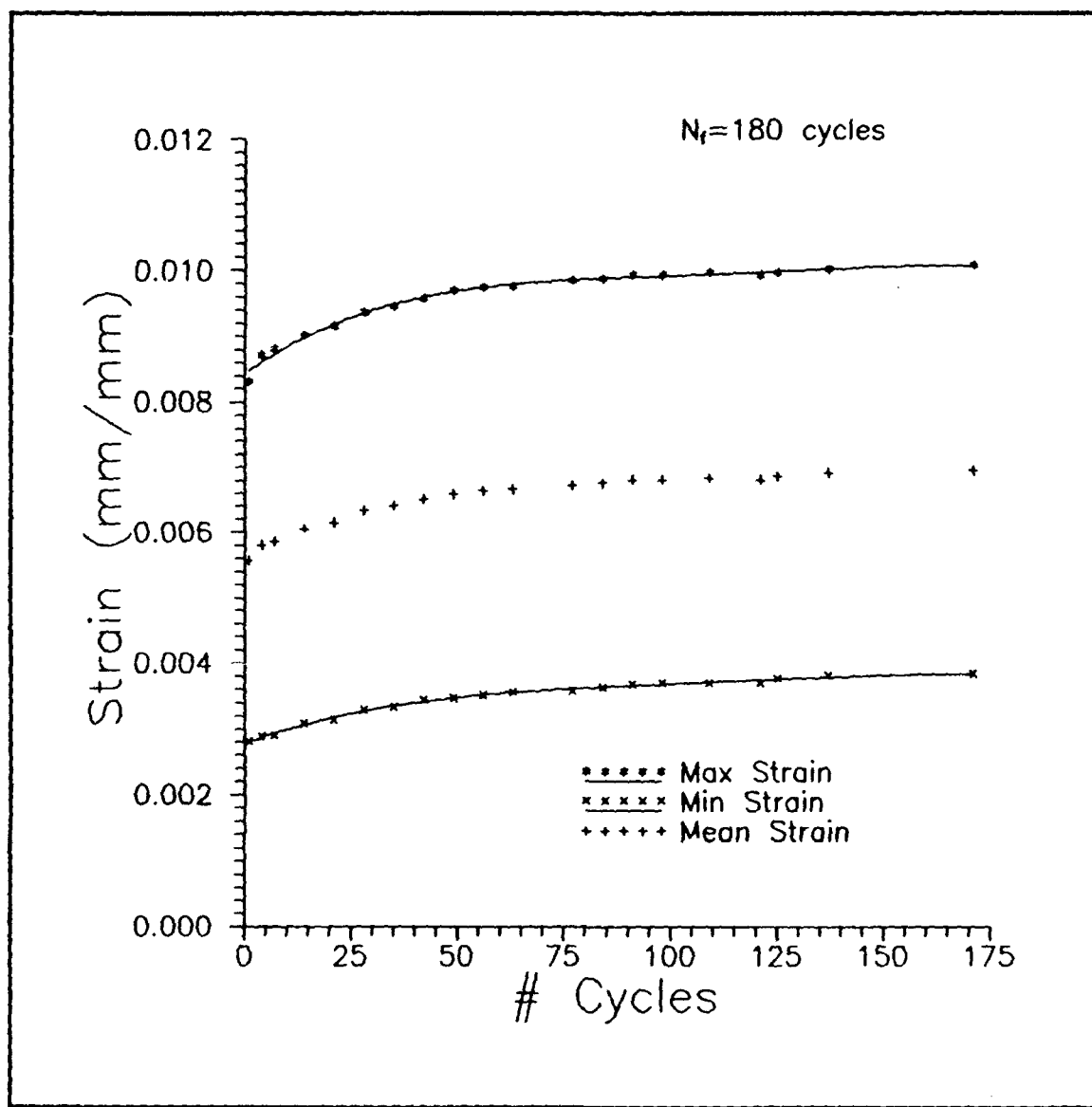


Figure 27. Strain Data for 612 MPa In-Phase Test

night unless building air conditioning was functioning properly. The problem made absolute strain measurements from this one low load test unusable, but due to the relative very low frequency of the drift in comparison to a single test cycle time,  $\Delta\epsilon_f$  measurements for each individual cycle recorded were considered accurate. The problem was alleviated

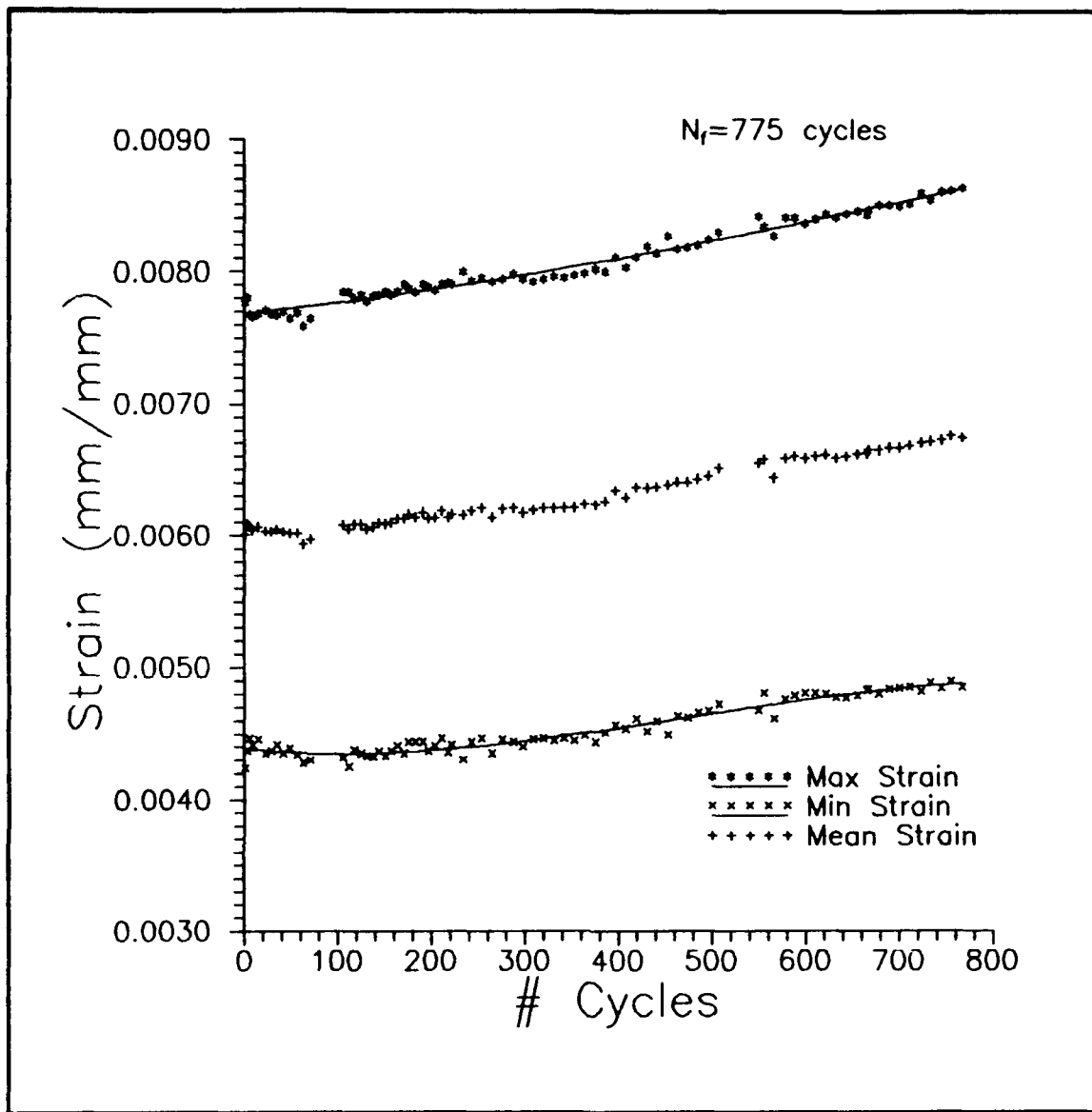


Figure 28. Strain Data for 612 MPa Out-of-Phase Test

when air conditioning systems were operating properly.

#### D. Young's Modulus Measurements

Instantaneous Young's Modulus during a test were calculated from the measured maximum and minimum total strains, maximum and minimum thermal strains from the TF test,

and measured maximum load with load ratio. The total strains were converted to maximum and minimum mechanical strains through equation 5. This change in strain can be used with the actual measured stress level, load ratio, and equation 6 to calculate a linear stress-strain curve slope. This assumption is only valid if the actual applied stress to mechanical strain curve is linear. As it was mentioned earlier, after the first few cycles, the TMF loading curve for I-P fatigue testing became almost linear and this assumption was used. For O-P tests the TMF applied loading curve displays an open hysteresis loop due to effective cancellation of thermal and mechanical strains. In this case, it is assumed the mechanical loading curve (i.e. without thermal effects) is approximately linear and mechanical strains can be determined by adding the change in thermal strain to the change in total strain. Even in the case of a slightly non-linear curve, the maximum and minimum strains will give an effective modulus which will decrease as plasticity or fatigue cracking increases. At failure this modulus value goes to zero as the maximum strain goes to infinity.

The four tests conducted at loads below the predicted FPF strength showed a peculiar phenomenon of modulus change. These tests showed a minor modulus drop in the first few cycles, followed by a rapid steady modulus increase and then decrease over the next 2000-5000 cycles of the tests, followed

by a continual slower decrease in modulus to failure. This change in modulus can be attributed to several effects. These all cause some form of material hardening. Plastic strain hardening or "cold-working" was a possible cause. Alloys exhibit a marked increase in modulus and Brinell Hardness during cold-work. This increase in hardness is due to an elongation of the grains and is dependent on the stresses applied to the material as well as the temperature at which they are applied. The cold-work phenomenon may be a possible factor in these tests due to the load and temperature conditions experienced by the matrix during testing. Age hardening is another method of increasing the young's modulus of a material. Some materials can be aged at room temperature or slightly elevated temperatures to increase hardness. The time of initiation and the final magnitude of the increase or decrease of modulus is dependent on the temperature at which the material is held and the length of time at that temperature. (1:269-279) The increase is followed by a decrease in hardness with continued work and this decrease is assumed to be accompanied by cracking and damage to the material giving the effect of decreasing age-hardening (A-H), but the damage is probably accumulating to offset a stable or semi-stable hardness parameter.

Because the specimens were used in the as-fabricated condition and no heat treatment was used, we can expect some

variation in modulus due to aging during the test period accompanied by other damage progression. The number of cycles in which the modulus increased was in the range of 1000 to 3000 cycles or 0.5-2.0 days of testing time, depending on stress level. Knowing that the age/work-hardening mode is present in our calculations of the modulus parameter, we can now attempt to isolate the contribution of various components in this modulus variation. Initially, there was a small drop in modulus, this phase can be called a "softening" phase and lasted up to about 20 cycles. This phase includes such effects as initial damage, thermal gradient settling, initial creep, relaxation of residual stresses, etc. The second phase in the modulus change is the previously described age-hardening phase. The third phase is damage progression. In this third phase damage dominates and, due to this factor, modulus continues to decrease till failure. In each phase we are assuming a dominant factor, i.e. softening (S), age-hardening (A-H), Damage. These factors are assumed to work independently, although we know all factors may be existent and interacting with each other throughout the test, but the distinct trend of only one factor dominates during a particular phase. For instance, damage may occur throughout the A-H phase offsetting some of the total modulus increase that would have been seen had there been no damage, but the trend of the increase and the timing of the phase remain the

same.

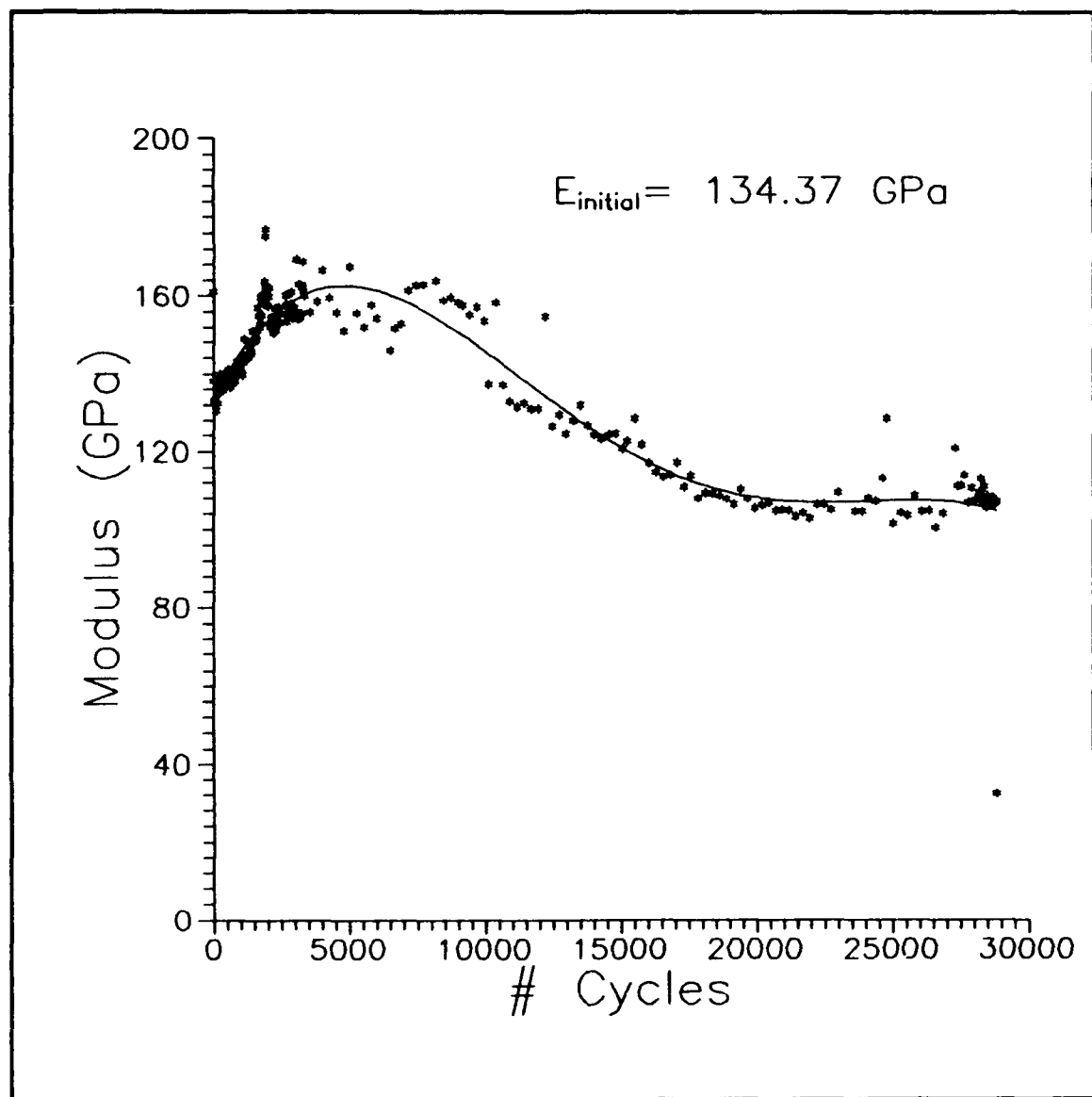


Figure 29. Modulus Data for 367 MPa In-Phase Test

In the case of the high load tests (i.e. at loads higher than FPF strength) such as in 125% FPF I-P/O-P, damage progression is expected to dominate throughout the test and no age-hardening, due to initial damage during the first cycle. See Figures 29 to 34 for calculated instantaneous modulus data

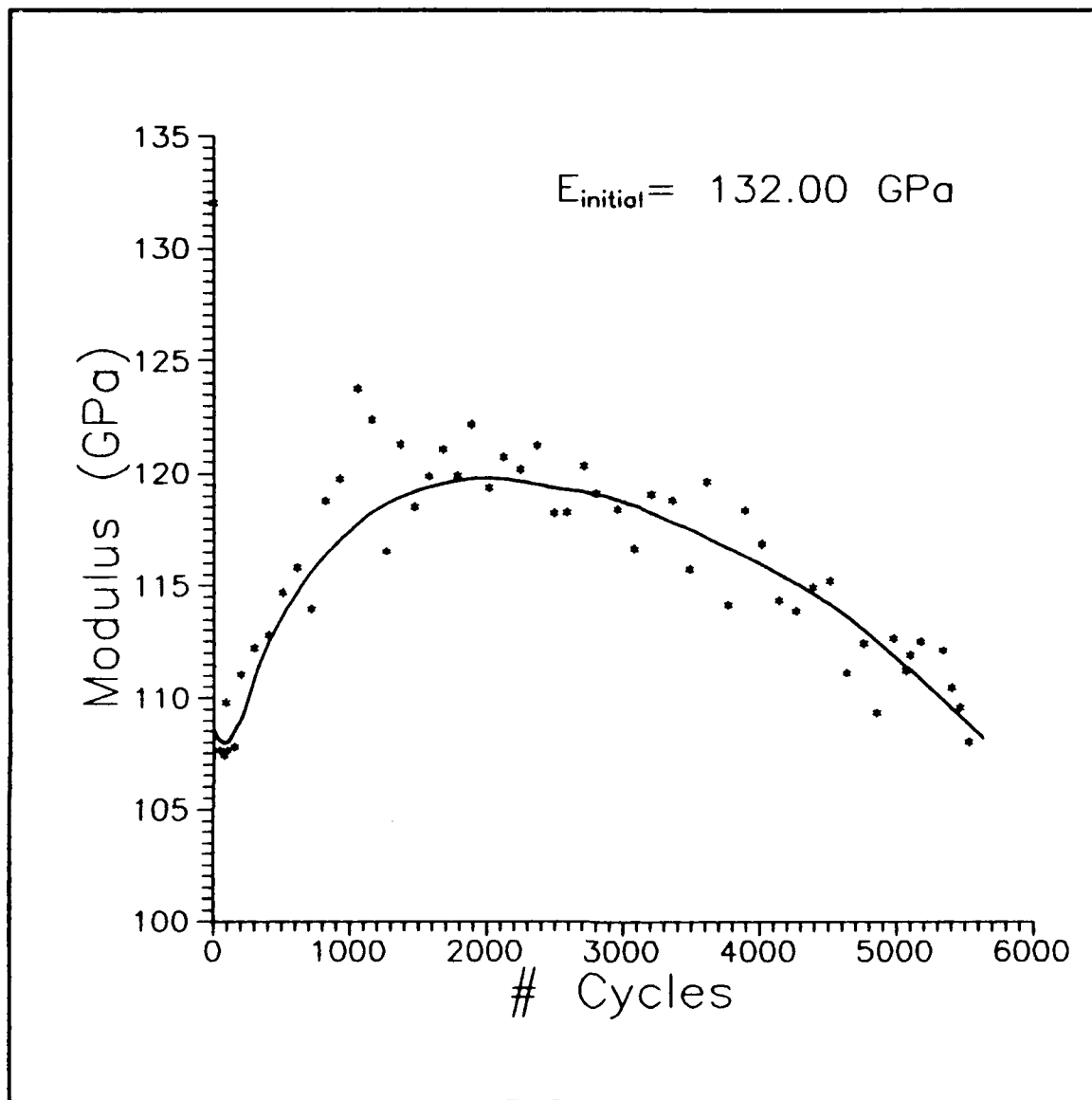


Figure 30. Modulus Data for 367 MPa Out-of-Phase Test

from the six tests. Additional modulus data is shown in Appendix C for the 50% FPF I-P and 60% FPF O-P tests.

#### E. Fracture Analysis

Two techniques were used for examination of crack damage and fracture during these tests. The first one was

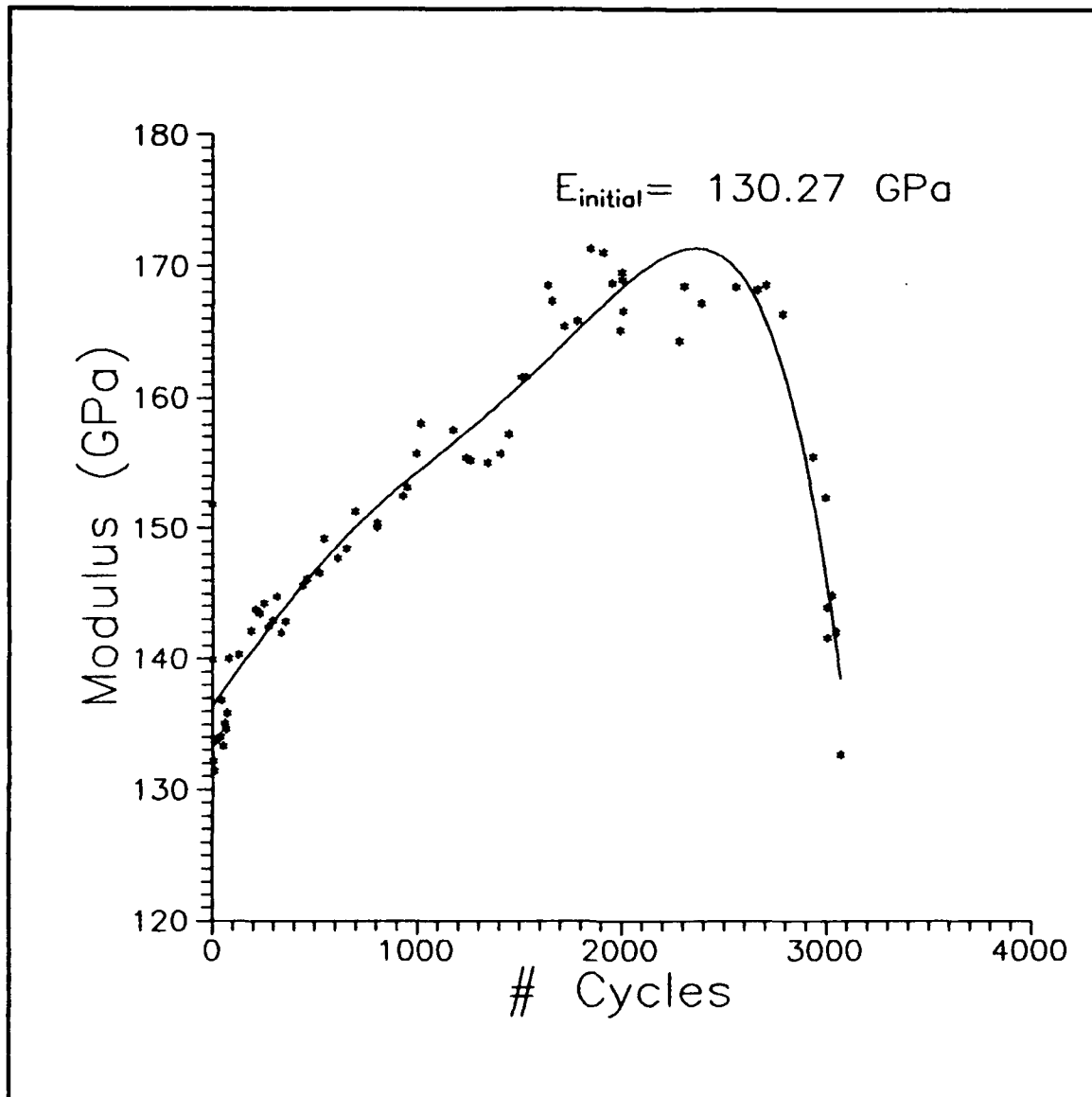


Figure 31. Modulus Data for 441 MPa In-Phase Test

replication technique, discussed at the beginning of this chapter and a summary of damage initiation on the edge of the specimens seen through the replica technique is shown in Figure 21. The second method of study was to investigate the damage at failure of the specimens at and near the fracture surface through scanning-electron-microscope (SEM)

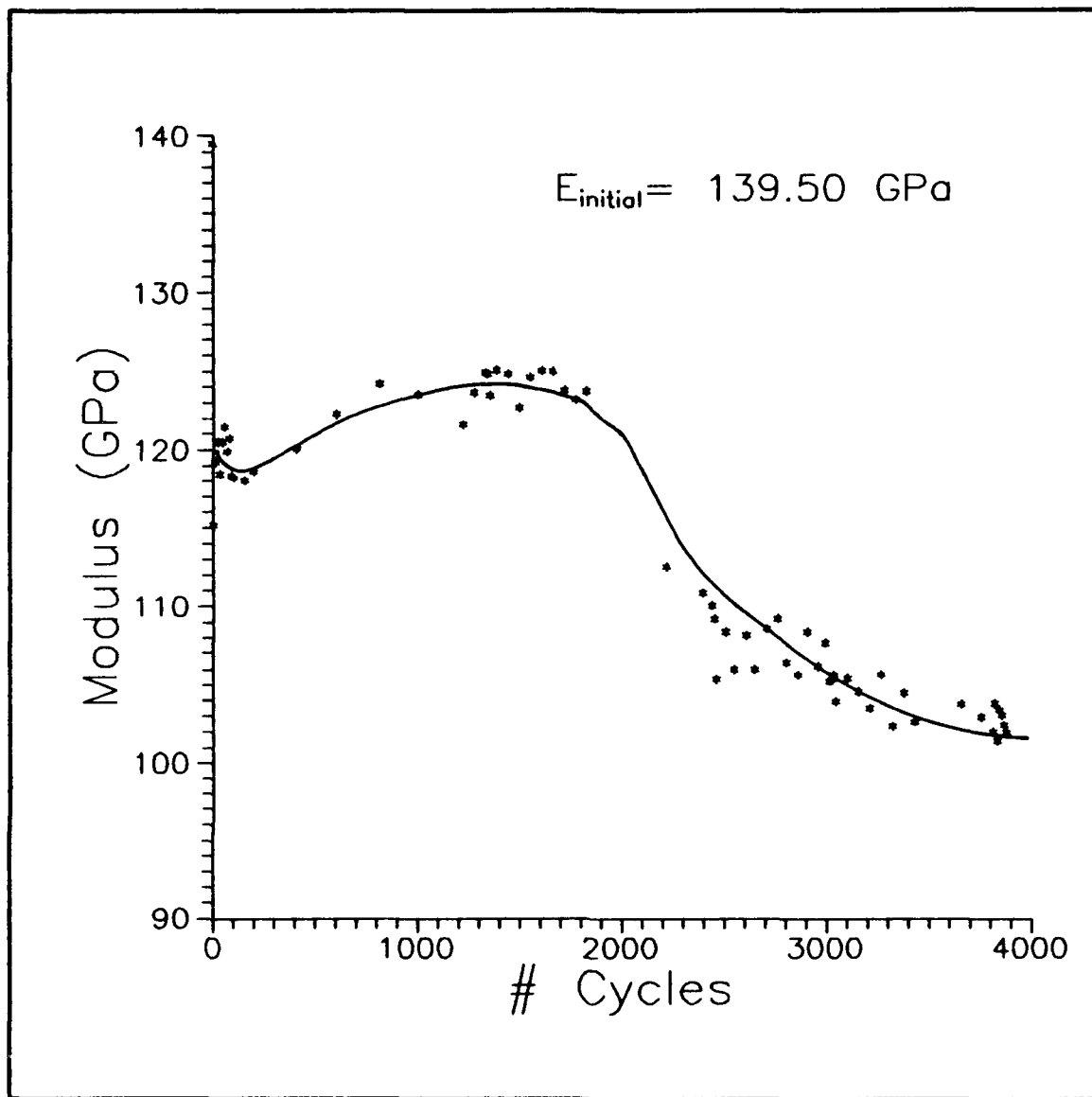


Figure 32. Modulus Data for 441 MPa Out-of-Phase Test

photographs. Small sections of the specimens to include the fracture surface and pieces very-near (<1.5 mm) the fracture surface were cut off using a diamond sectioning wheel, mounted in a thermoplastic mounting compound, and polished to a 1 micron finish. The specimens were then observed optically, photographing internal cracks. They were then etched using a

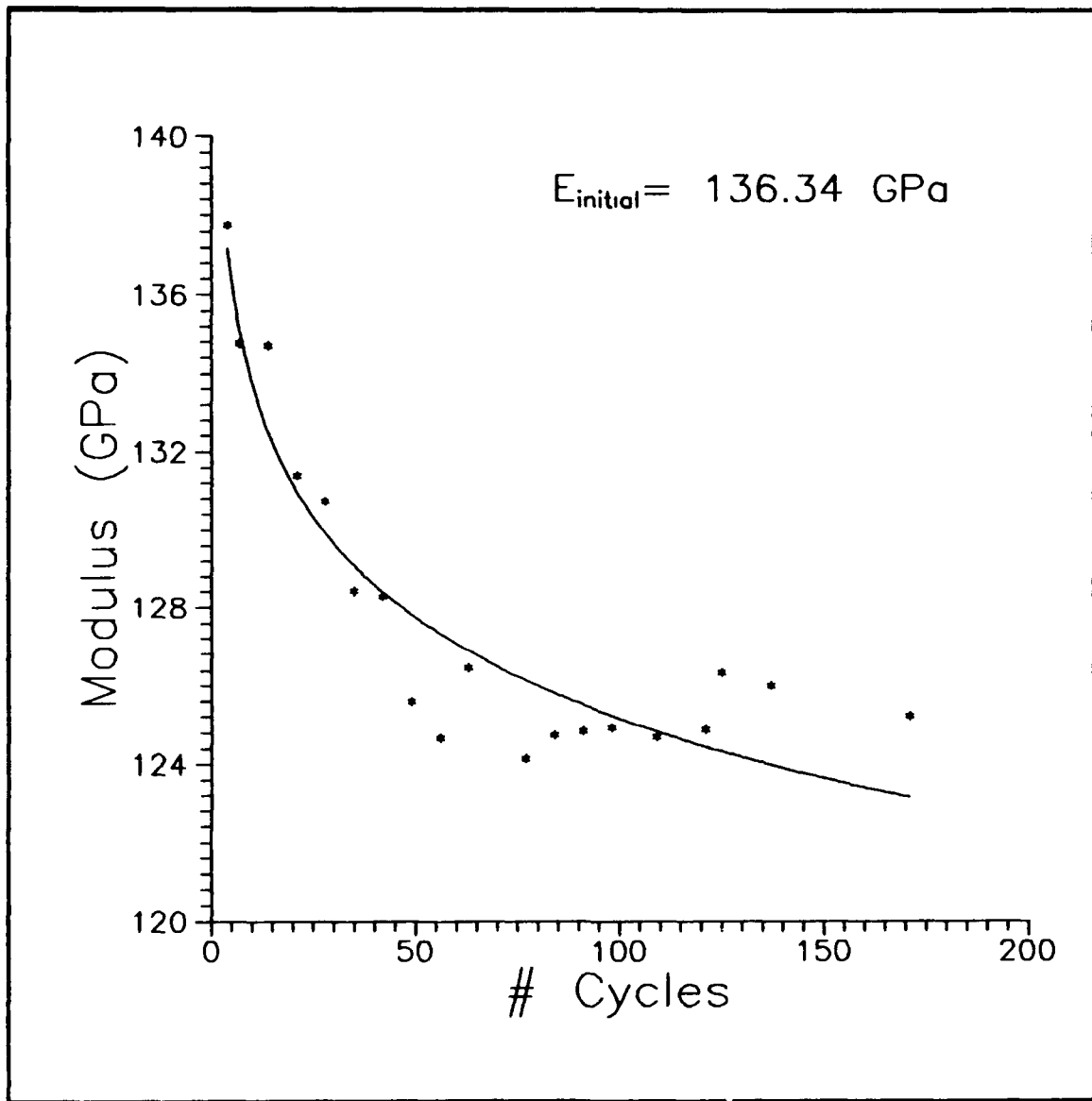


Figure 33. Modulus Data for 612 MPa In-Phase Test

weak nitric acid-based etchant (Kroll's) to reveal  $\alpha$  and  $\beta$  phasing in the matrix alloy during SEM analysis. This procedure helps to distinguish the reaction zone size surrounding fibers by providing a better surface contour between  $\beta$  and precipitated  $\alpha$  phase alloy. Surfaces cut and observed through this procedure for each of the failed

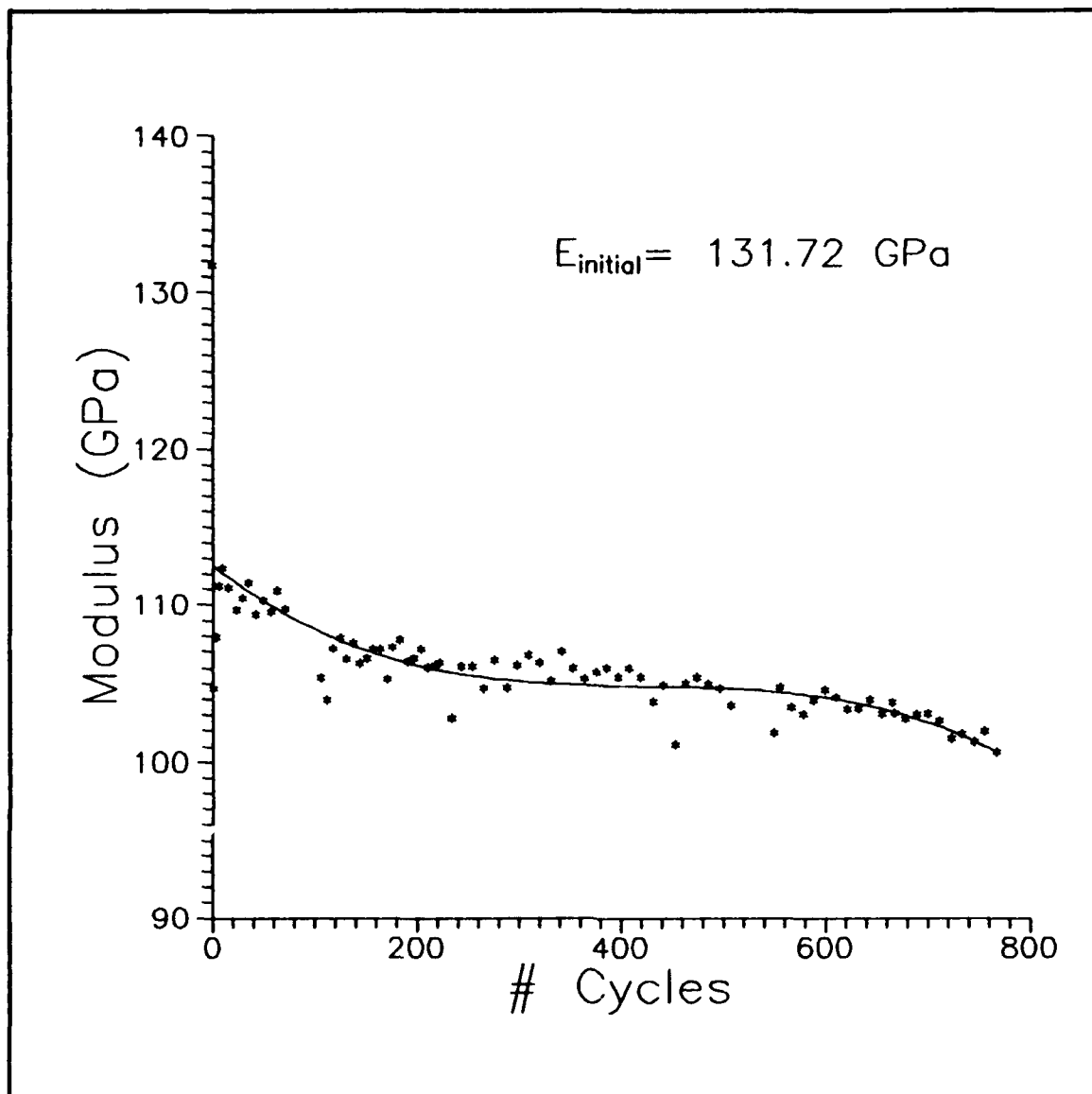


Figure 34. Modulus Data for 612 MPa Out-of-Phase Test

specimens are shown in Figure 35. It was noted that the reaction zone size during TMF testing increases rapidly during the first 5,000 cycles and the rate of increase slows between 10,000 to 20,000 cycles. Roughly 2/3 of the growth noted up to 28,900 cycles occurred between 0 and 5,000 cycles. Figure 36 plots average reaction zone thickness vs. number of cycles

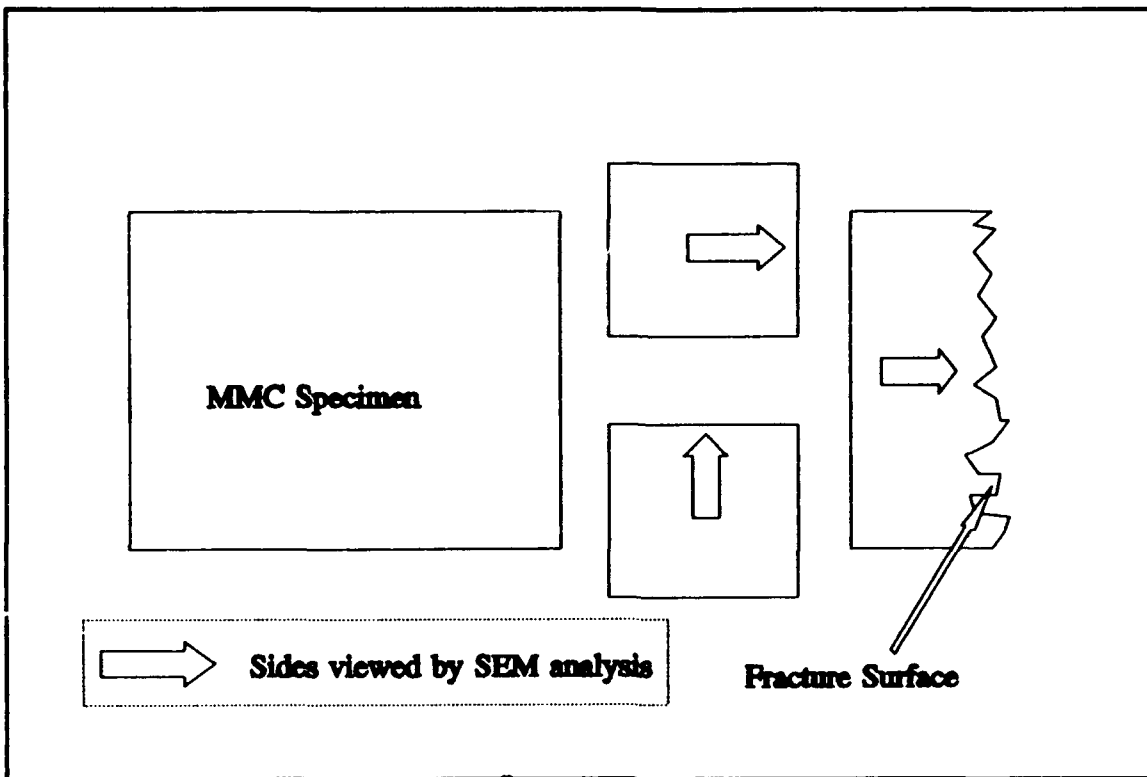
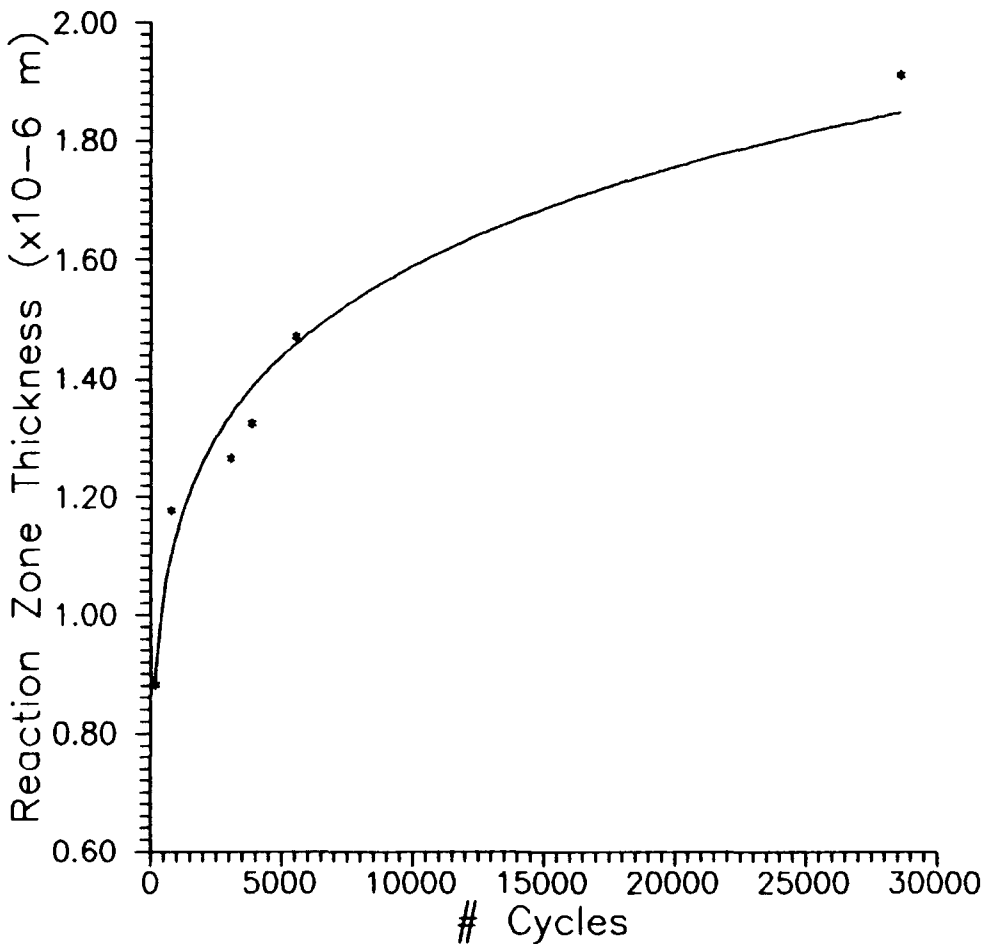


Figure 35. SEM Sectioning Schematic

to show this trend. Also, it can be seen in Figures 37 and 38, showing the reaction zones at 180 and 28,900 cycles, respectively, that the zone starts thin, smooth, and closely attached to the fiber and with extended thermal cycling thickens and exhibits a definitely weak or detached bond to the fiber. Zones shown are from  $0^\circ$  fibers to eliminate the effect of separation due to load magnitude.

Analysis of the fracture surfaces shows three distinct crack progression trends. First, as would be expected, in the two tests conducted at  $\sigma_{max}$  above predicted first ply failure strength obvious points of  $90^\circ$  ply failure exhibiting large failure areas and ductile necking of material were found.



**Figure 36. Reaction Zone Sizing**

Also, for both in and out-of-phase high load tests, the fracture surface is not even and there is a definitive plateauing effect due to many cracks propagating on different levels and coalescing near where fracture occurred.

Cook and Gordon, as referenced by Meyers and Chawla (21:456), analyzed stress distributions in front of a

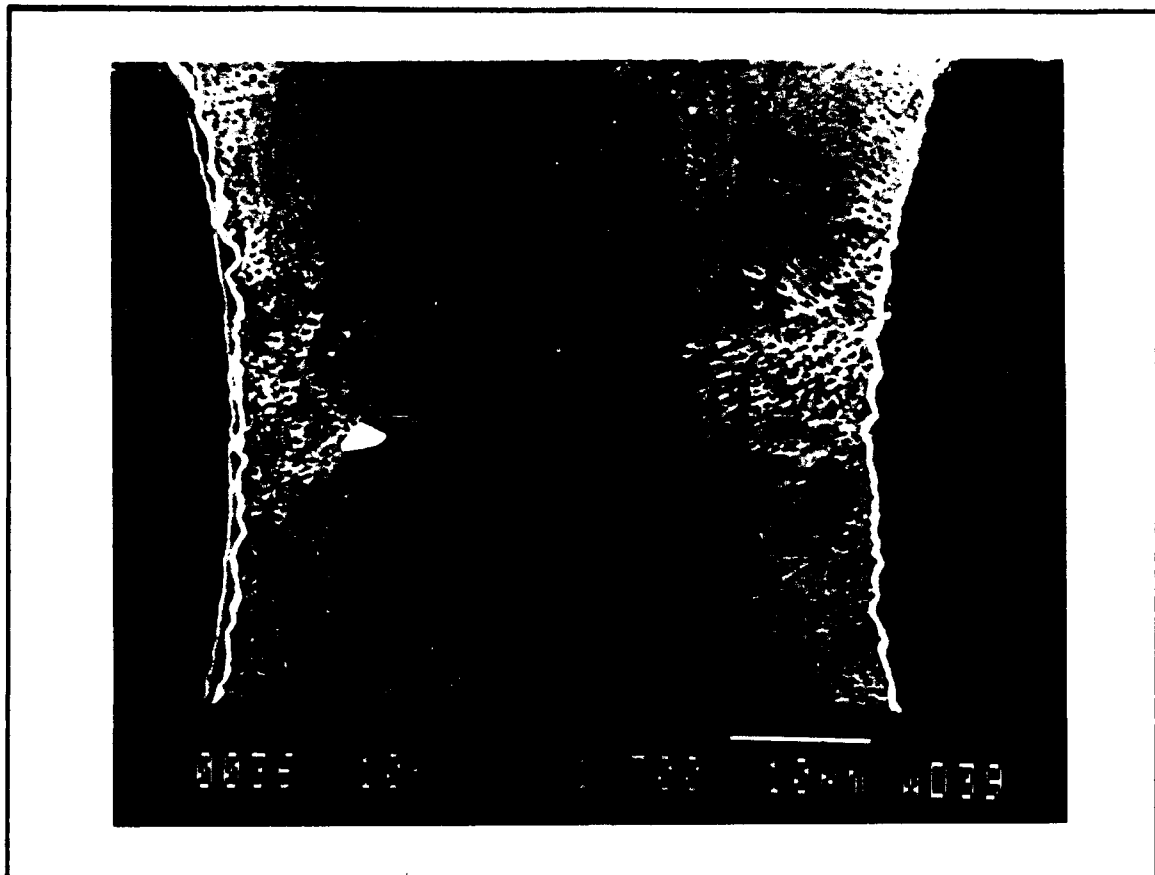


Figure 37. Reaction Zone at 180 Cycles

transverse crack tip propagating toward a  $0^\circ$  fiber in composites. These authors concluded that as the transverse tensile stress  $\sigma_{22}$  reached a critical value relative to the applied longitudinal stress  $\sigma_{11}$ , the fiber matrix interface in front of the crack tip will fail and pull away from the  $0^\circ$  fiber under the influence of the transverse tensile stress and the transverse crack will be deflected  $90^\circ$  from the original direction. Figure 39 depicts this deflection effect. The deflection, due to the high loading stresses, caused the transverse cracks in the  $90^\circ$  ply of the specimen to be

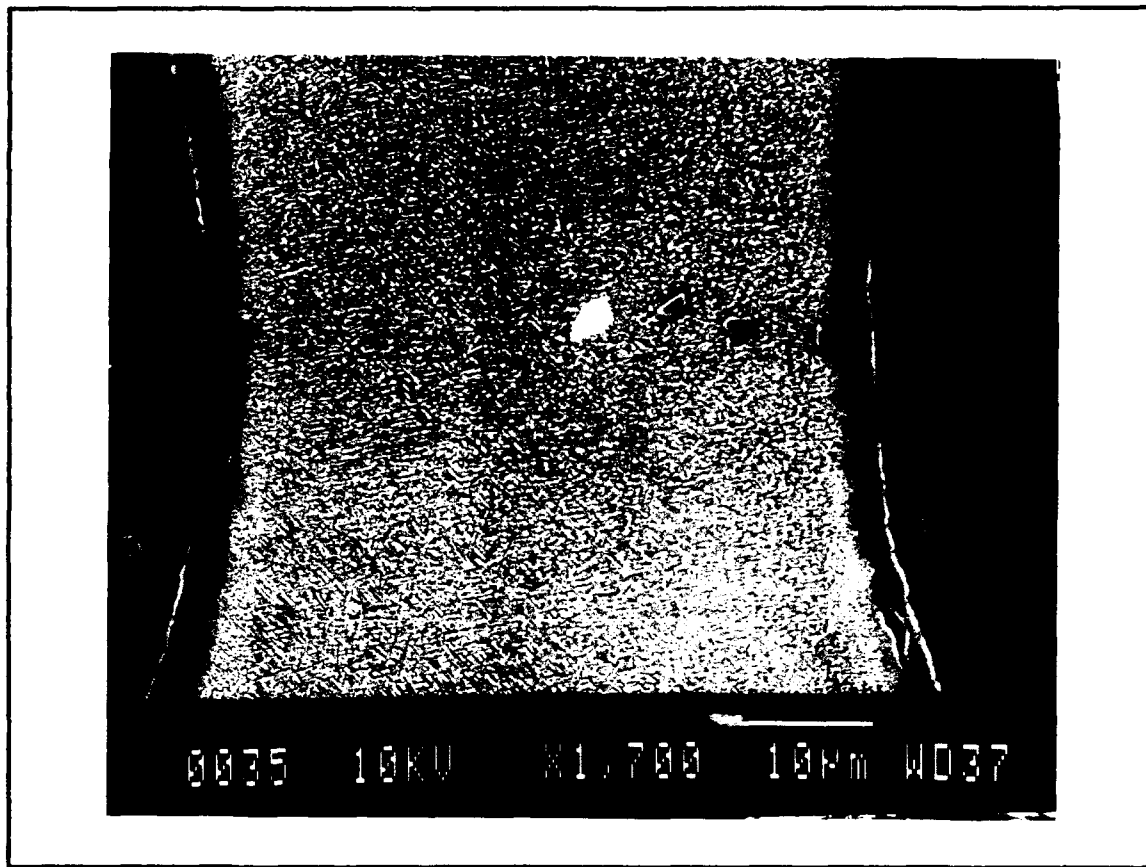


Figure 38. Reaction Zone at 28,900 Cycles

deflected and coalesce on various levels in the specimen at failure as well as cause a necking down or channelling effect of matrix material at points between failed  $0^\circ$  fibers generating local stress concentrations and ductile failure in the matrix material (28:9).

Figures 40 shows the reaction zone of a  $0^\circ$  fiber in a 125% FPF test without an incoming crack and Figure 41 shows the same fiber where a crack has separated the zone from the fiber. This crack deflection effect in a high stress test is shown by the fracture surface in the top of Figure 47. The

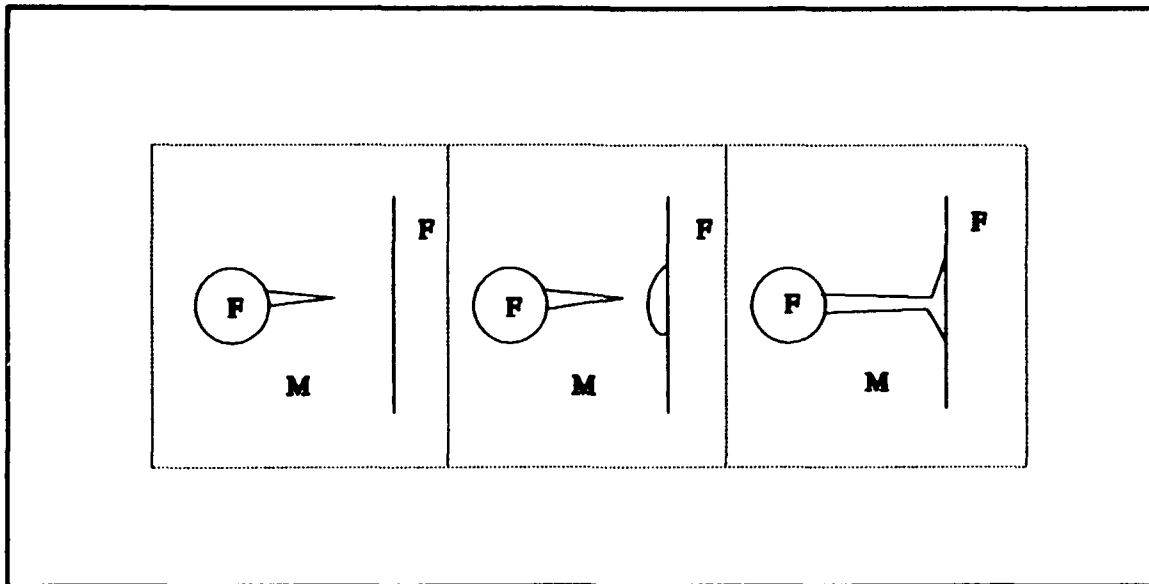


Figure 39. Interface Crack Deflection

resulting surface is uneven with a great deal of fiber pullout.

A similar uneven fracture surface occurred in the low load (367 MPa) IP test. The effect this time was caused by a time factor in the test rather than high stress but results are similar in appearance. Interfaces had degraded to such an extent over the thermal cycling time that even at the minimal loading stress, the interfaces separated and caused the slow-growing transverse cracks to deflect to different planes. This separation of reaction zone and fiber for the low load test is shown in Figure 42. The fracture surface is shown at the top in Figure 45. In the previous two cases, 90° fibers at the fracture surface seemed to separate cleanly from the matrix indicating a weak or damaged bond between fiber and matrix.

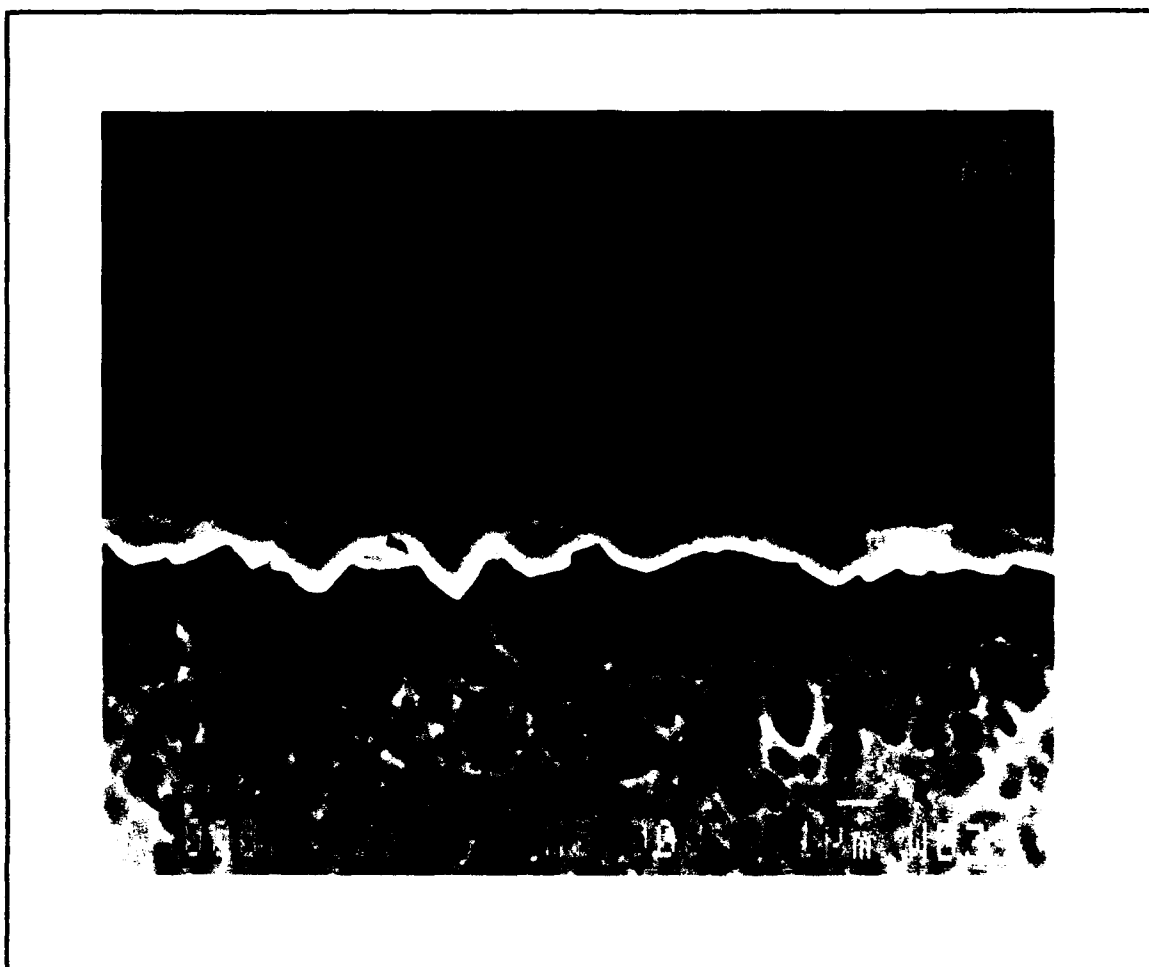


Figure 40. High Load Test Reaction Zone Without Crack

For the 90% IP (441 MPa) and 75/90% OP (367/441 MPa) tests, fracture surfaces were flat, relatively even, and had little fiber pullout. This indicated transverse cracking began and ended in the same plane, progressing around and eventually through 0° fibers when stress levels increased to a critical level. Figure 43 shows a reaction zone bond to the fiber in the 441 MPa O-P test. The fracture surface of the test is at the bottom of Figure 46. It should also be noted that the fibers in this fracture surface are well bonded and

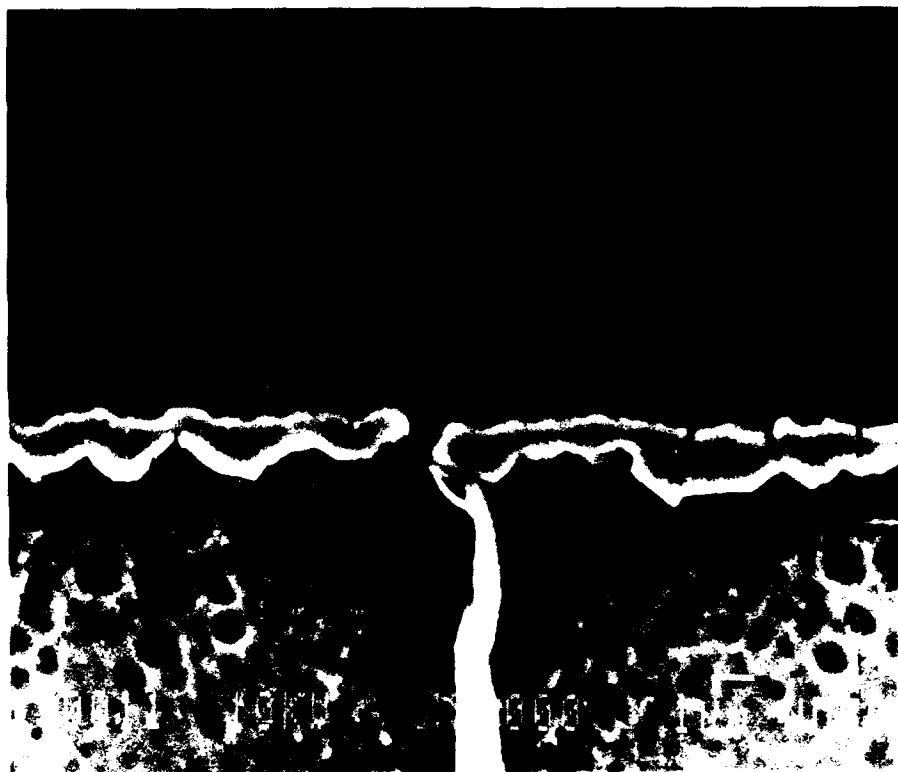


Figure 41. High Load Test Reaction Zone With Incoming Crack

some even split rather than separated from the matrix. Figure 44 depicts the characteristic spectrum at the fracture surfaces. Fracture surface photographs for all six fracture surfaces are shown in Figures 45-47.

As was shown in Figure 21, edge damage analysis using the replica technique showed exposed 0° edge fibers cracked almost immediately after test initiation, with the number of cracks increasing in number with increasing load and cycles. These cracks, though, did not seem to progress into the matrix nor

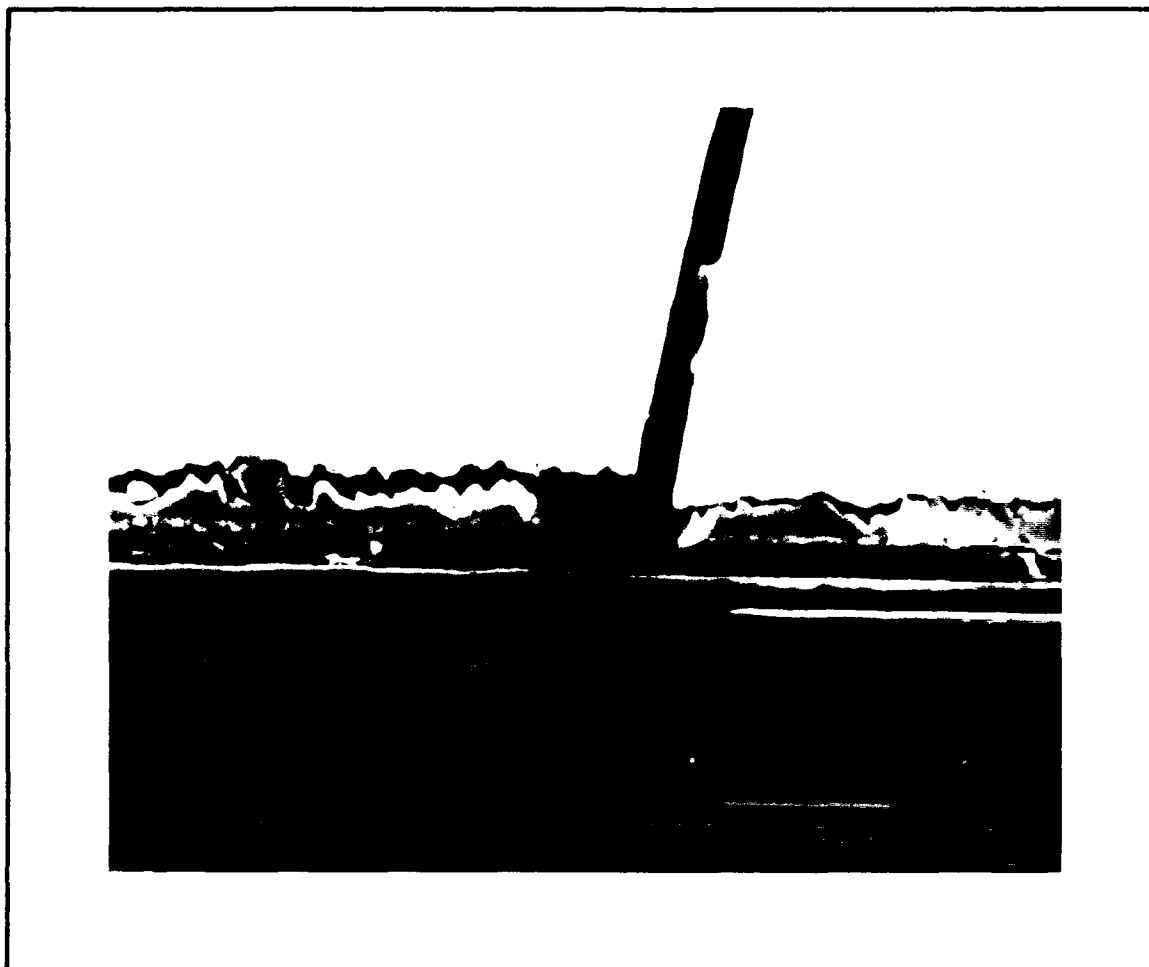


Figure 42. Low Load Test Reaction Zone With Incoming Crack

did these cracks seem to correlate directly with internal fiber cracking at failure. This damage, along with the longitudinal cracks noted in the TF test, was isolated to the edge of the specimen and did not effect failure damage characteristics. This "edge effect" was also noted by Ermer (6). Although the longitudinal and 0° fiber cracks were isolated to the edge of the specimens, replica analysis proved to be a good indicator of internal transverse matrix cracking.

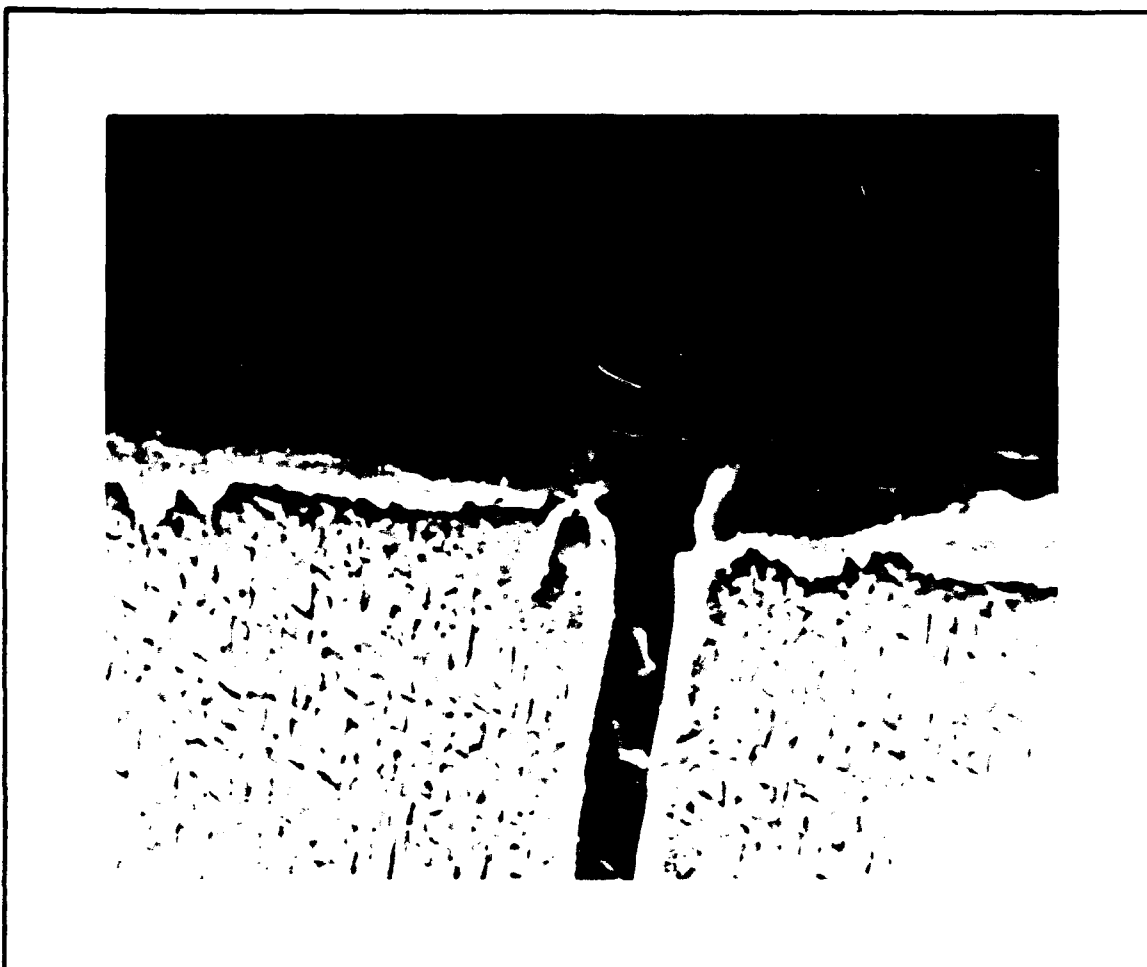


Figure 43. Medium Load Test Reaction Zone With Incoming Crack

No conclusive characteristics could be found distinguishing IP and OP internal damage at an individual load level. Transverse cracking as seen in Figure 48 was the dominant damage factor in every case. Figure 49 shows the initiation of these cracks from the interface and reaction zone of the 90° fibers. Cyclic growth of these cracks can be seen by the river patterns seen in Figure 50 from a different angle (the central fiber in the photo is a 90° fiber). Damage from one load level to another load level shows changes in

## FRACTURE SURFACE SPECTRUM

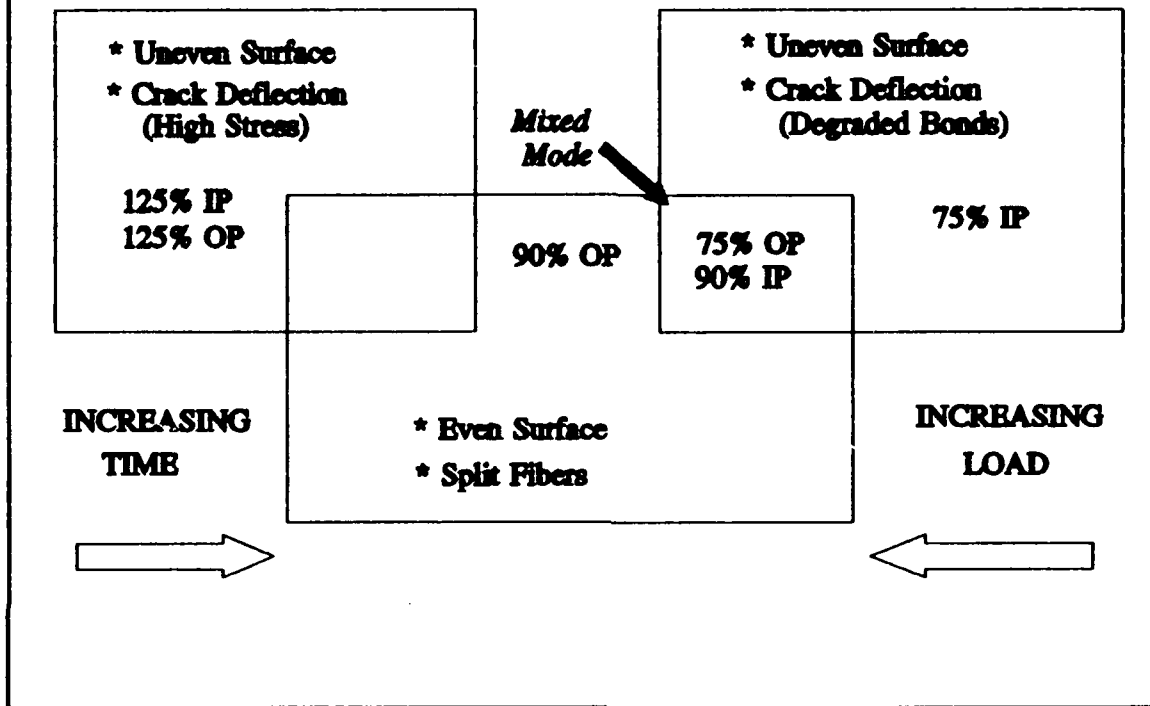


Figure 44. Fracture Surface Spectrum

size, number, and mode of progression as load is increased.

Low load tests showed many small, slow-growing cracks increasing in number with time (cycles). The largest and faster growing cracks initiated at the  $90^{\circ}$  fiber/matrix interface and grew transversely from fiber to fiber. As the cracks grew toward  $0^{\circ}$  fibers, they were deflected, as discussed earlier, and coalesced with cracks in other planes also being deflected along fibers. After failure of the matrix material,  $0^{\circ}$  fibers now cracked under increased stress

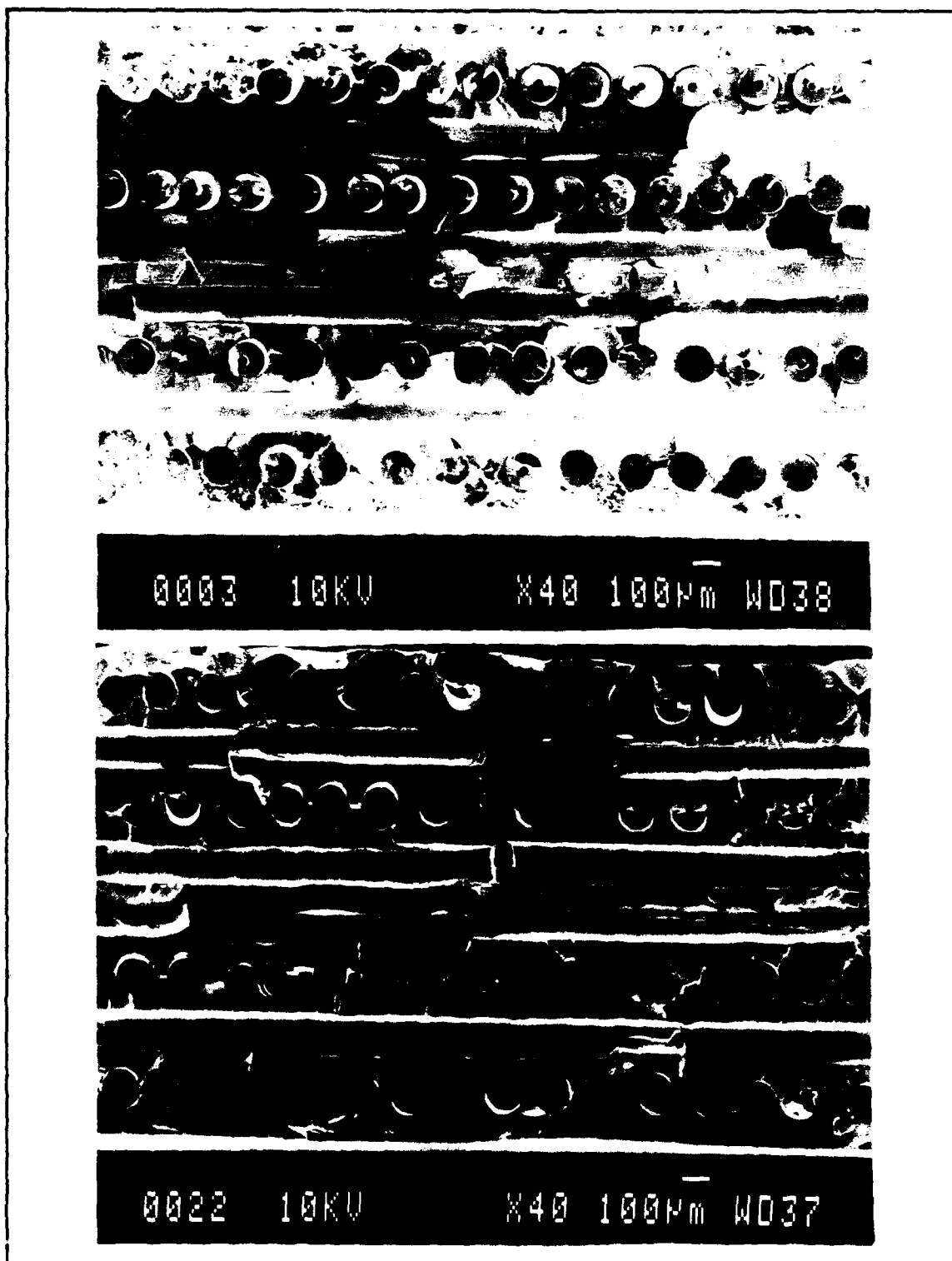
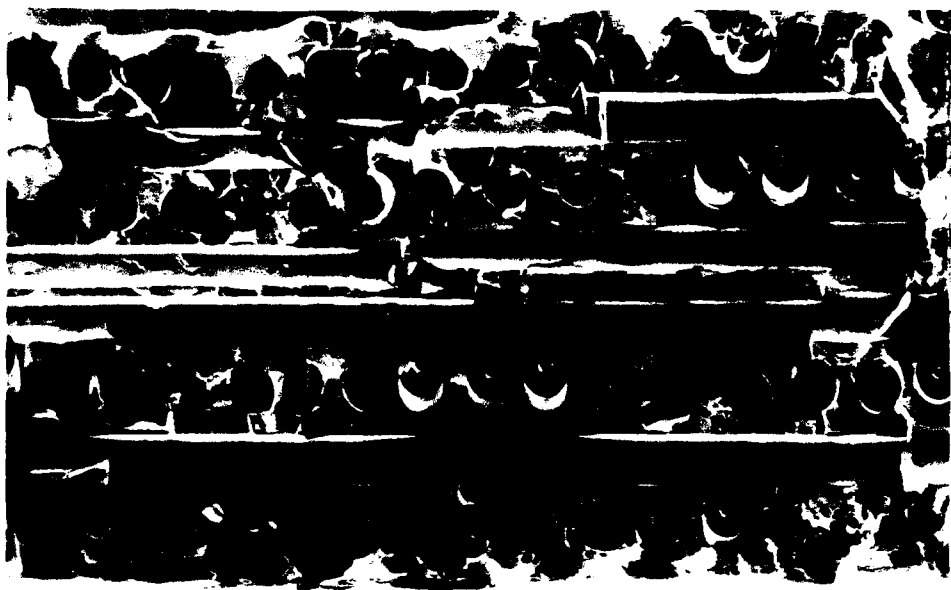
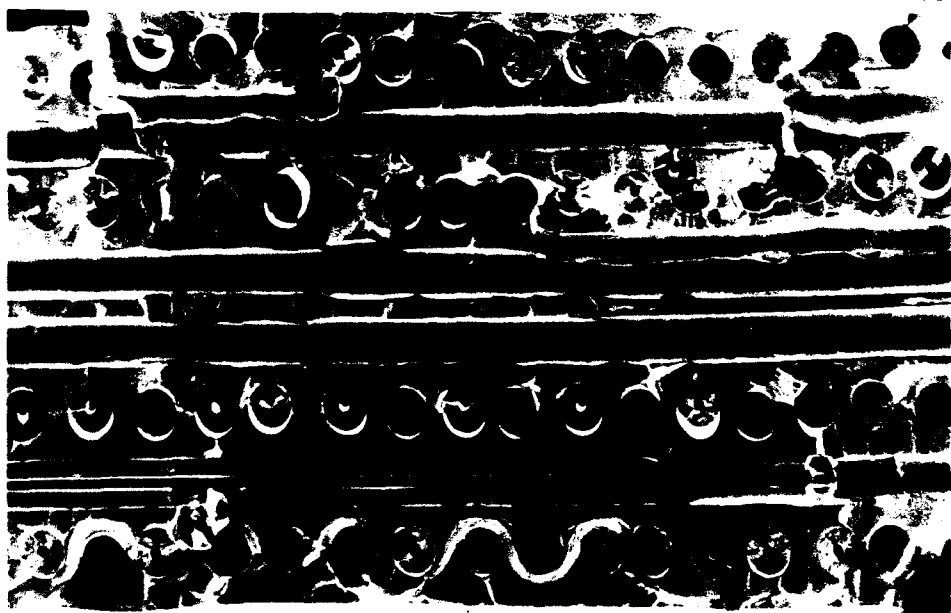


Figure 45. Fracture Surfaces - 367 MPa I-P (TOP):367 MPa O-P (BOTTOM)



0011 10KV

$\times 40$  100 $\mu$ m WD35



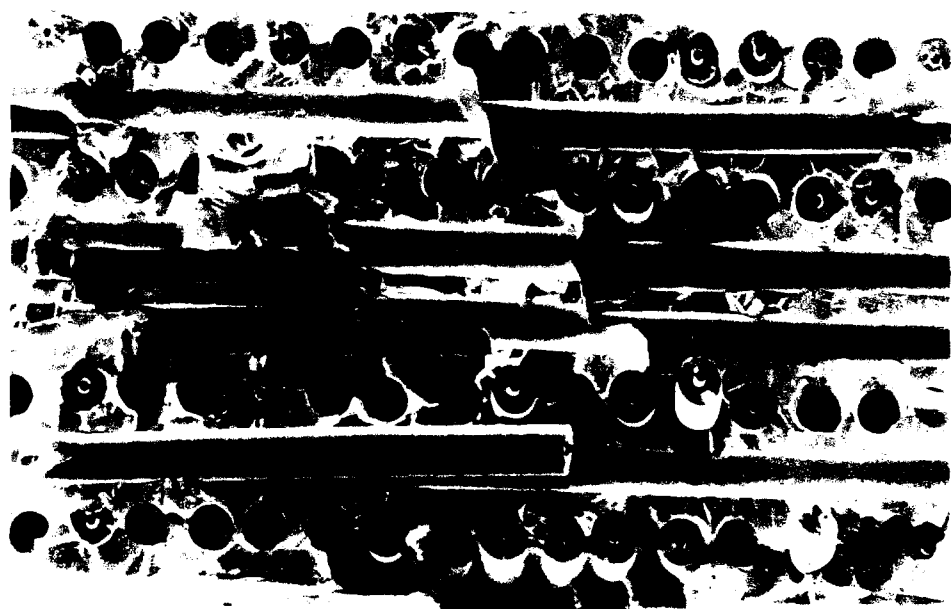
0019 10KV

$\times 40$  100 $\mu$ m WD37

Figure 46. Fracture Surfaces - 441 MPa I-P (TOP):441 MPa O-P (BOTTOM)



0007 10KV X40 100 $\mu$ m W035



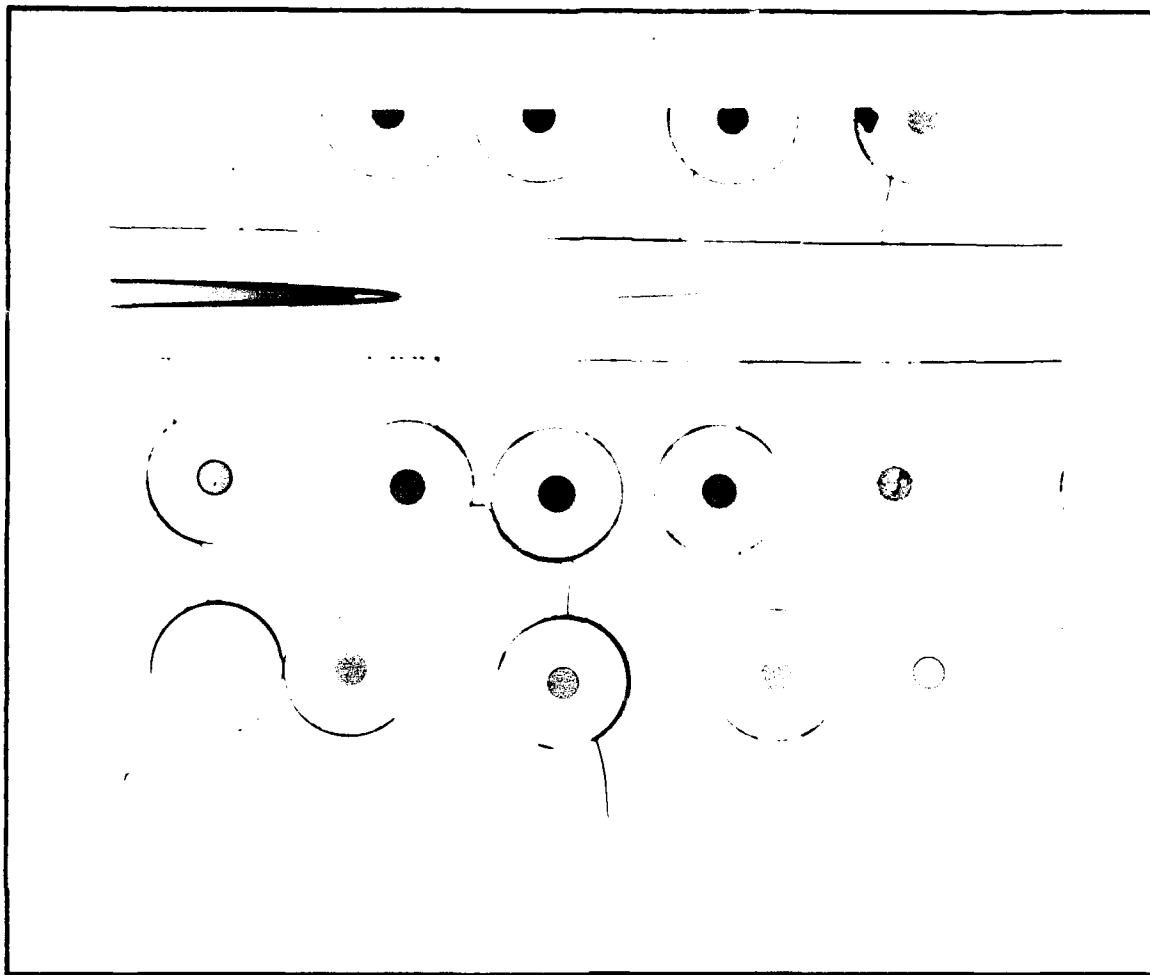
0015 10KV X40 100 $\mu$ m W037

Figure 47. Fracture Surfaces - 612 MPa I-P (TOP):612 MPa O-P (BOTTOM)

and the degraded fiber matrix interface gave way to failure with a large amount of fiber pullout.

In medium load tests, the size and progression rate of the cracks increased. This caused cracks to coalesce while still in the matrix and form a single coplanar transverse crack or a few large transverse cracks on closely spaced planes. When these cracks reached the 0° fibers, the stress level was not high enough to debond the matrix from the fiber nor had enough cycles elapsed to degrade the interfaces sufficiently for fiber pullout. Instead, the cracks progressed further through the matrix and around the 0° fibers. When enough of the matrix material had failed, stress concentrations around the fibers caused by matrix cracks at the failure plane, broke the 0° fibers with little or no fiber pullout.

In high load tests above predicted FPF strength, many large cracks initiate when 90° plies fail. These cracks progress very quickly and the load is sufficiently high to cause the debonding phenomenon discussed earlier. Cracks are partially or fully diverted and coalesce on many planes. Interfaces which have been debonded from the fibers by excessive stress can no longer hold fibers which have been cracked by high specimen strains. Failure is fast and the fracture surface exhibits both ductile and cyclic fatigue characteristics with a large amount of fiber pullout.



**Figure 48. Transverse Cracking - Sectioned Specimen**

A summary of the three main modes of crack progression is shown in Figure 51. These three modes of crack progression were common to both I-P and O-P tests.

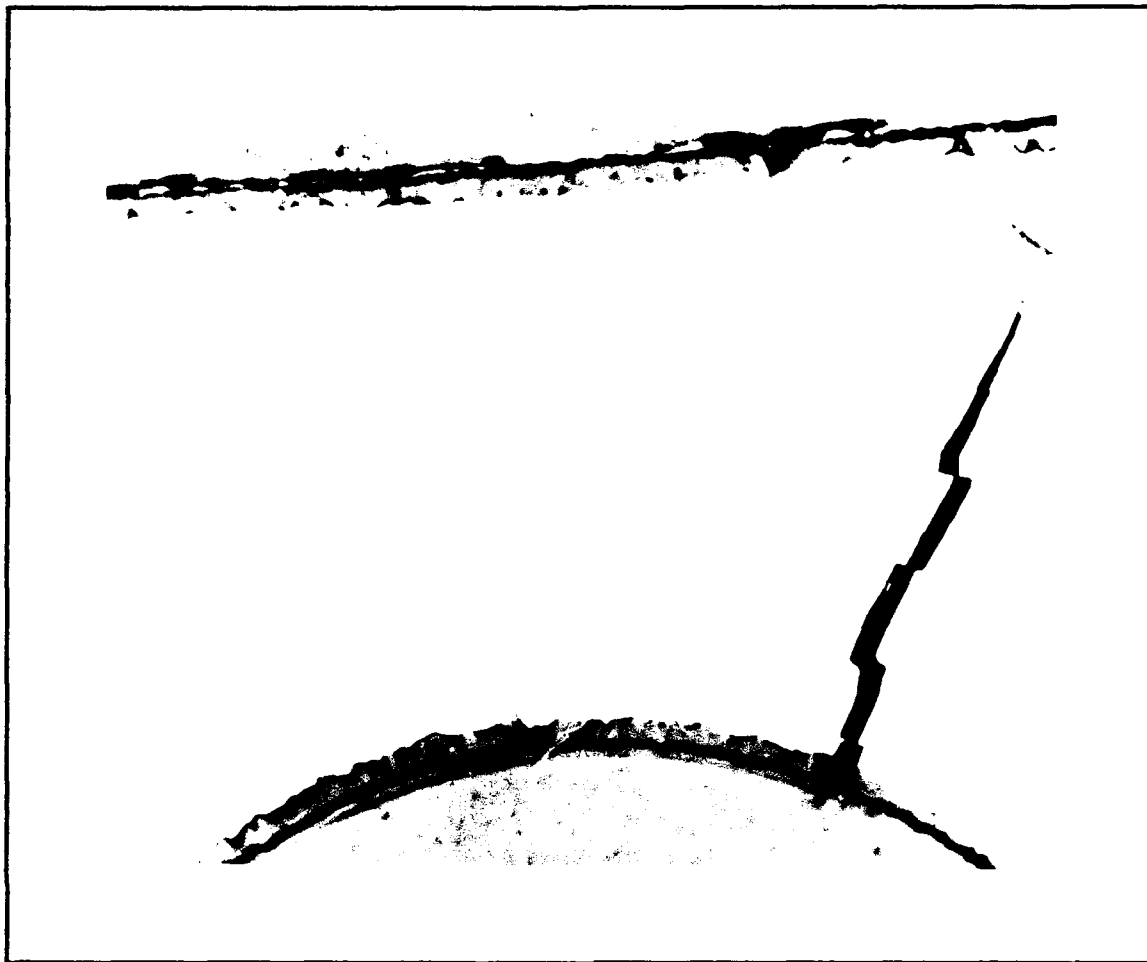


**Figure 49.** Close-up of Transverse Crack Initiation at Interface

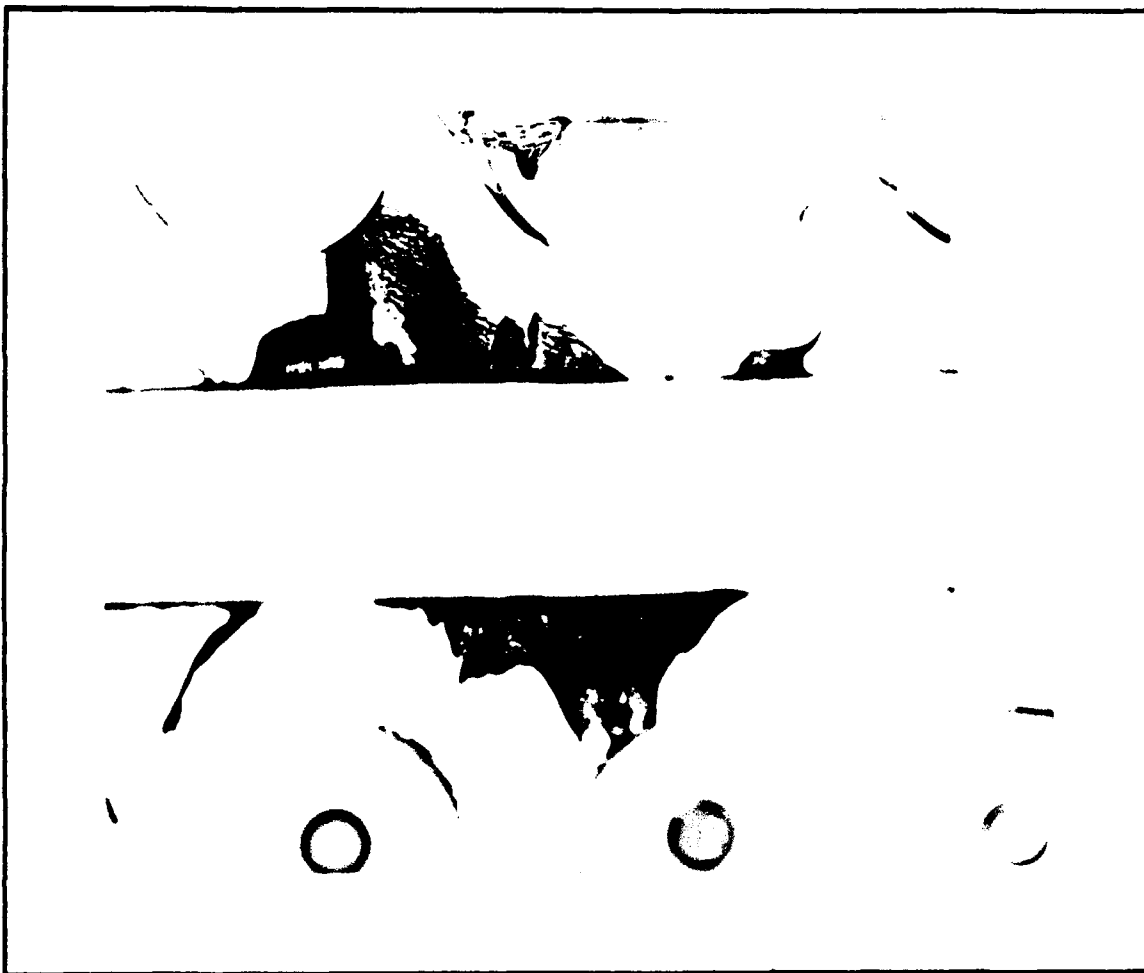


Figure 50. Fatigue Crack Growth from 90° Ply

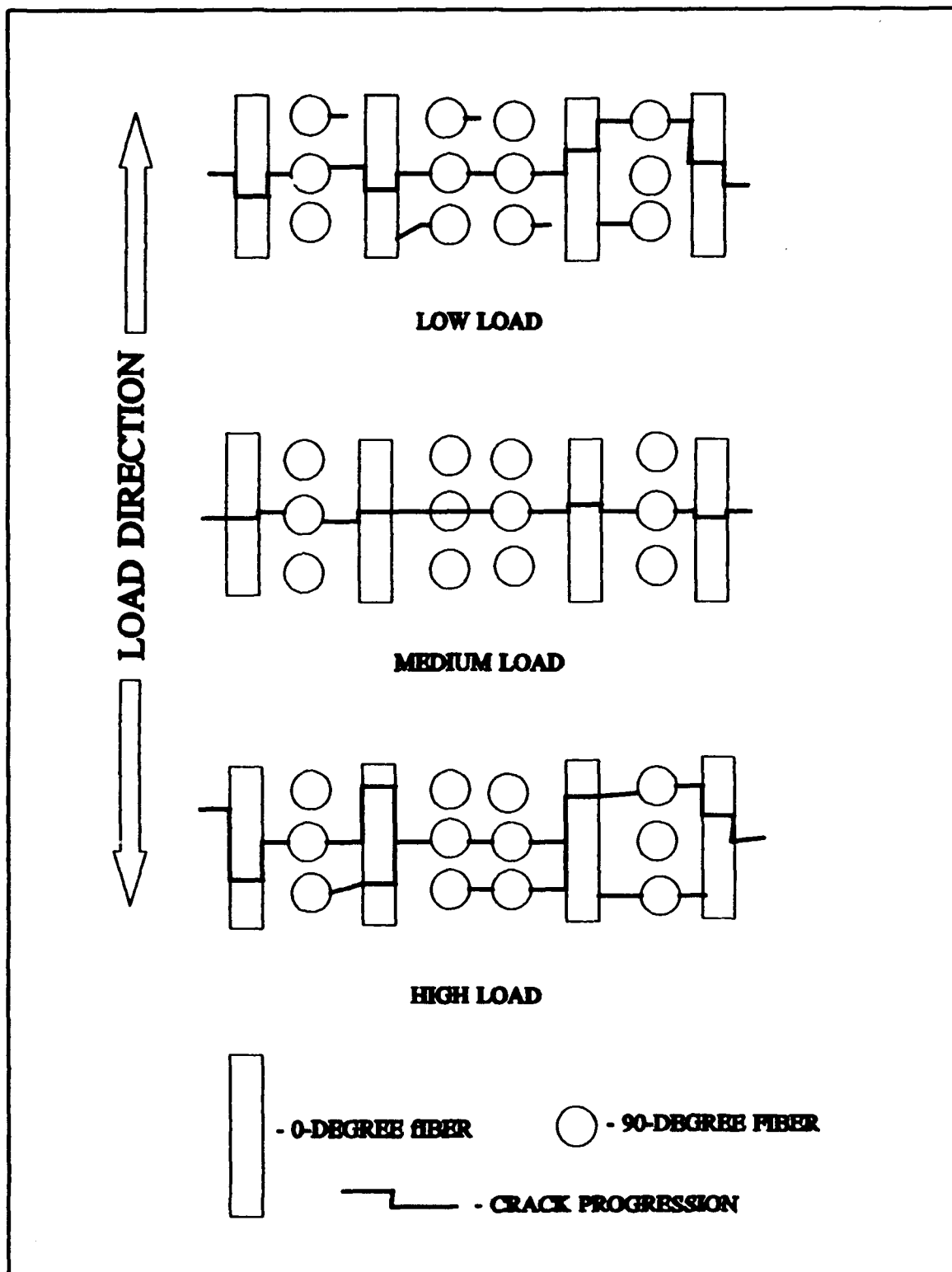


Figure 51. Summary of Crack Analysis

## V. Analysis

### A. Fatigue Life Governing Factors

The overall comparison of experimental data obtained from this study as well as data from Johnson's  $[0/90]_{2s}$  MMC tests

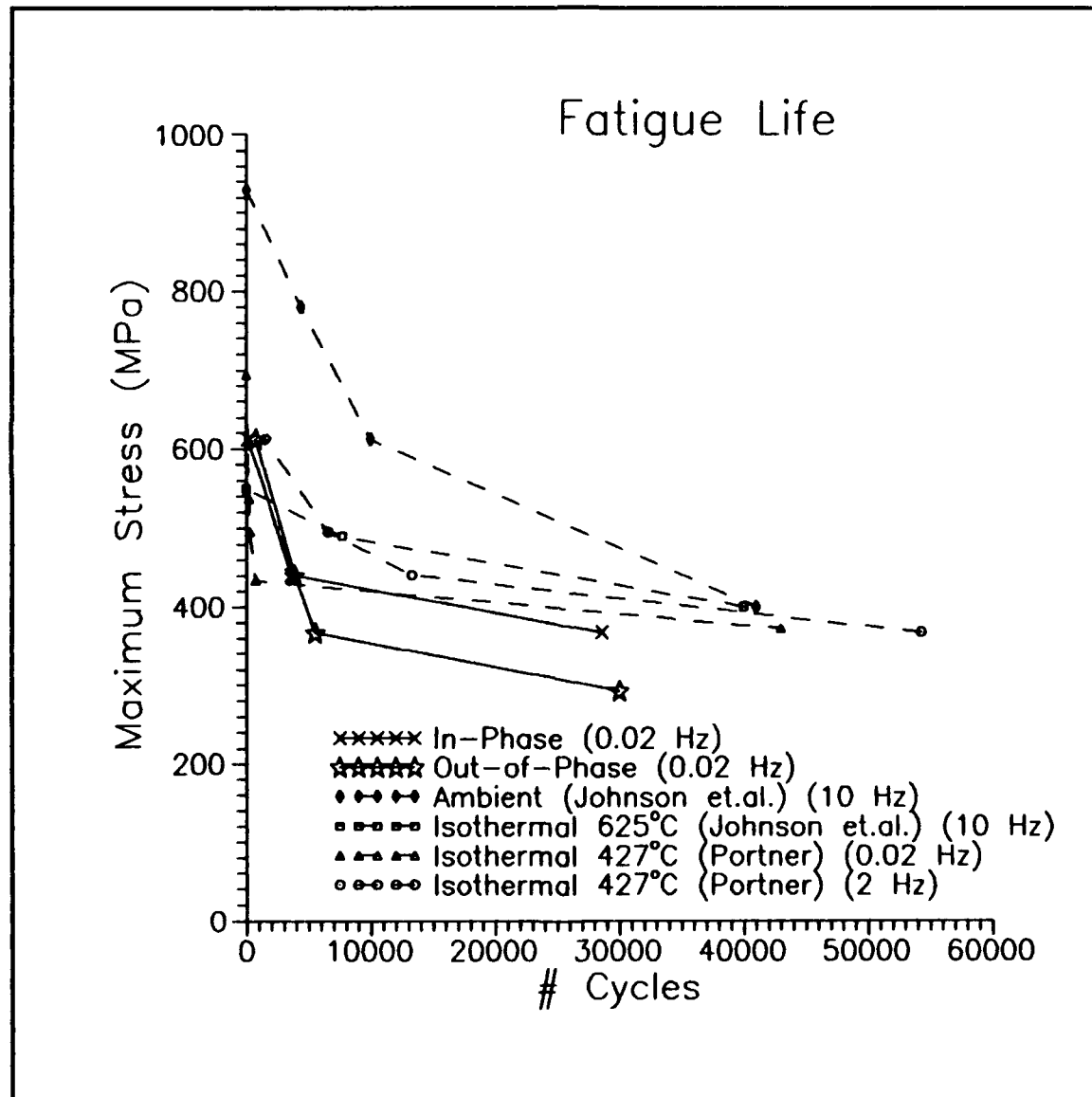


Figure 52. Fatigue Life Curves - Maximum Applied Stress

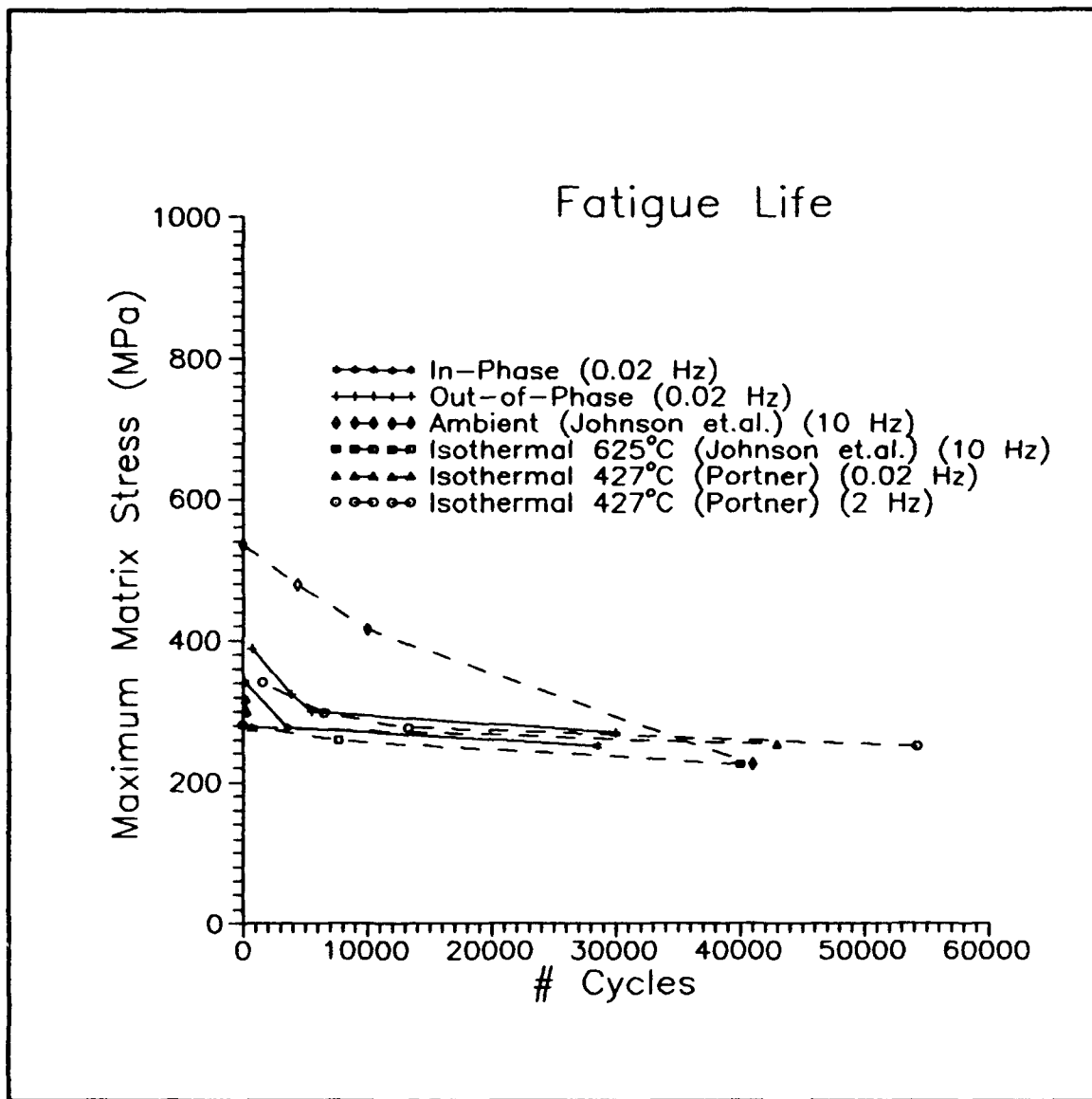


Figure 53. Fatigue Life Curves - Maximum 90° Matrix Stress

(16,28) and Portner's (29) isothermal data on the same lay-up is shown in Figure 52. The values of fatigue life differ widely with respect to applied stress for the different test frequencies, and test conditions of in-phase, out-of-phase, and temperature variations.

The maximum matrix and fiber stresses experienced during

these different test conditions were calculated using METCAN. Appendix A contains property values and details on which stresses were used from the code. Fatigue life for the IP, OP, and other tests were plotted against these calculated maximum matrix stress in the 90° ply and against maximum 0° fiber stress. Figures 53 and 54 show these results. It can be seen that a threshold level of matrix stress is converged which is independent of frequency, temperature, or phase angles between peak temperature and peak load (0° in-phase/180° out-of-phase) in Figure 53. The threshold level is between 250 and 300 MPa matrix stress. This information might be used by designers interested in designing below a fatigue threshold limit. The limit indicates that at threshold load levels fatigue life of the specimens is governed by the matrix properties only. As load is increased, other factors begin to spread the curves with other dependencies. Figure 54 shows that at lower load conditions there is no dominance of the 0° fiber stress on fatigue life. As load increases, the curves at a given temperature converge to a common value at 1 cycle (or the equivalent of a tensile test). At this point, failure of the specimen is dependent only on 0° fiber strength and temperature (static tests). A transition between matrix-determined fatigue life and fiber-determined life seems to occur across the applied stress spectrum.

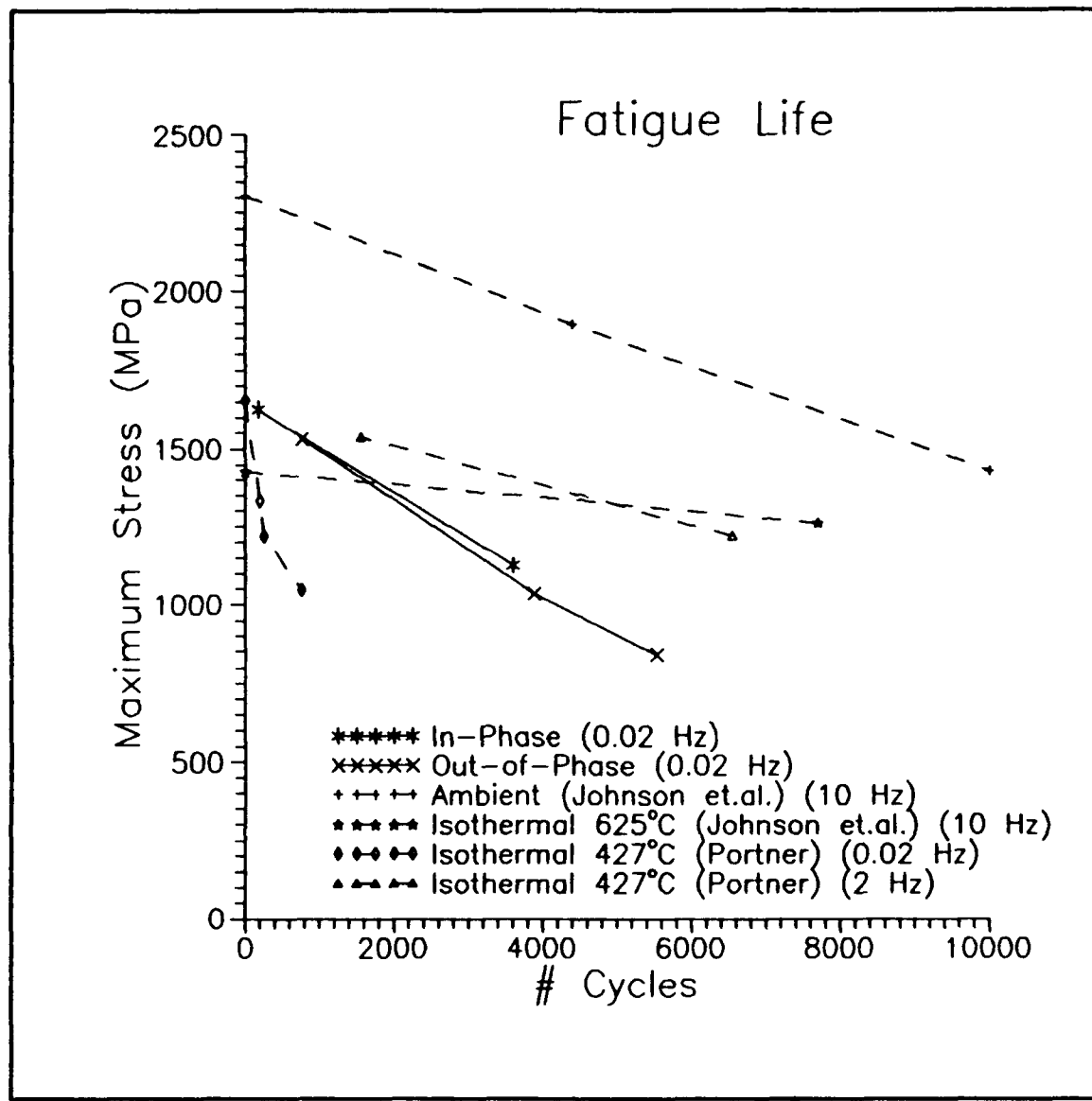


Figure 54. Fatigue Life Curves - Maximum 0° Fiber Stress

#### B. Cumulative Damage Models

The general concept of cumulative damage models incorporates the idea of a unit sample function. This unit sample is described as a component or material test in cyclic operation under a certain environment. During this operation irreversible changes occur in the unit until it can no longer

perform satisfactorily (i.e. failure). The time span of this operation is called the time to failure or lifetime. The overall process is called cumulative damage (CD). Some physical processes where CD takes place are (30:63-68):

- Fatigue
- Wear
- Crack Growth
- Creep-Rupture

One indicator of the progression of CD could be Young's Modulus. Given enough tests starting at a given initial damage (or initial modulus) and conducted under like experimental conditions, an empirical distribution function for damage vs time curves could be developed. Thus, a confidence band or mean damage curve predicting time to failure for a given component can be generated. Problems encountered with the generation of such models is the random nature of so many of the variables. Observations (30:69) of cumulative damage experimentation have shown that for any given unit:

- initial value of damage may be random
- damage at failure may be random
- damage in any given cycle is nondecreasing and random
- if the initial rise in damage is slow, a change in initial damage has a profound effect on time to failure of a given specimen

- if the final rise to failure is rapid, a change in damage at failure has little influence on time to failure
- even the generation of an empirical distribution function of time to failure does not necessarily characterize unit behavior

In this study, it is understood that the CD process is a stochastic process, therefore no simple model can totally characterize a given unit's characteristics. However, an attempt was made to derive a means to predict time to failure through a simple model by determining a failure criteria - damage. Curves derived from experimental data and the use of a damage parameter relationship gave simplified CD curves where linear portions of these curves could be used to predict remaining fatigue life.

A model used to linearly sum used portions of a specimen's life at various stress levels is given by the Palmgren-Miner Rule (21:702):

$$\sum_{i=1}^k \frac{n_i}{N_i} = 1 \quad (7)$$

$$\frac{n_1}{N_1} + \frac{n_2}{N_2} + \dots + \frac{n_k}{N_k} = 1$$

where  $N_i$  is a given fatigue life for specified  $\sigma_{max}$

$n_i$  is the portion of the given fatigue life used at a particular  $\sigma_{max}$

$k$  is the number of constant stress levels  $\sigma_{\max}$  encountered during a test and Damage at failure is defined to be unity. This relationship assumes damage growth and accumulation to be equal throughout each cycle of a life or unit time for a specified stress level. We know from experimental data that damage growth through time is not a linear relationship and therefore the model can only be used during the portion of

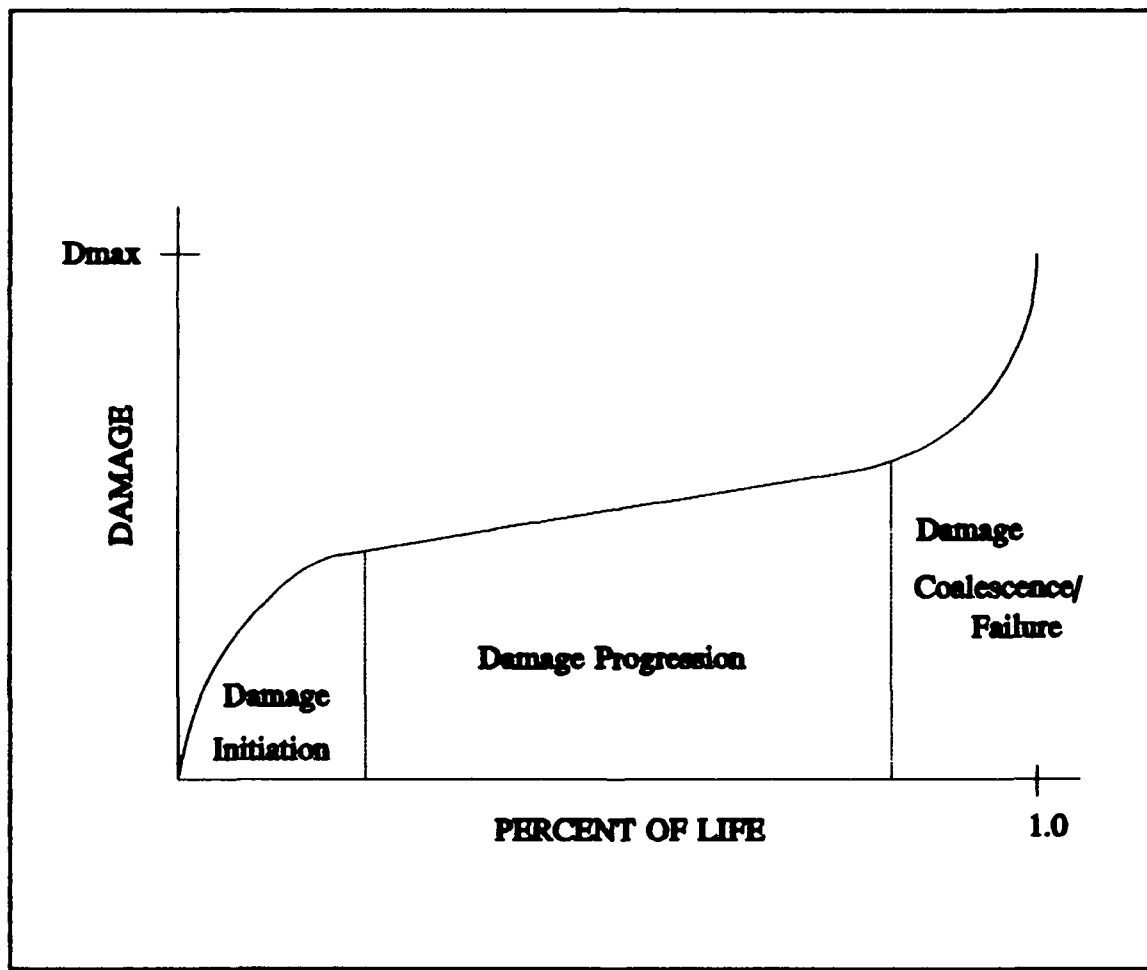


Figure 55. Classical Damage Growth Curve

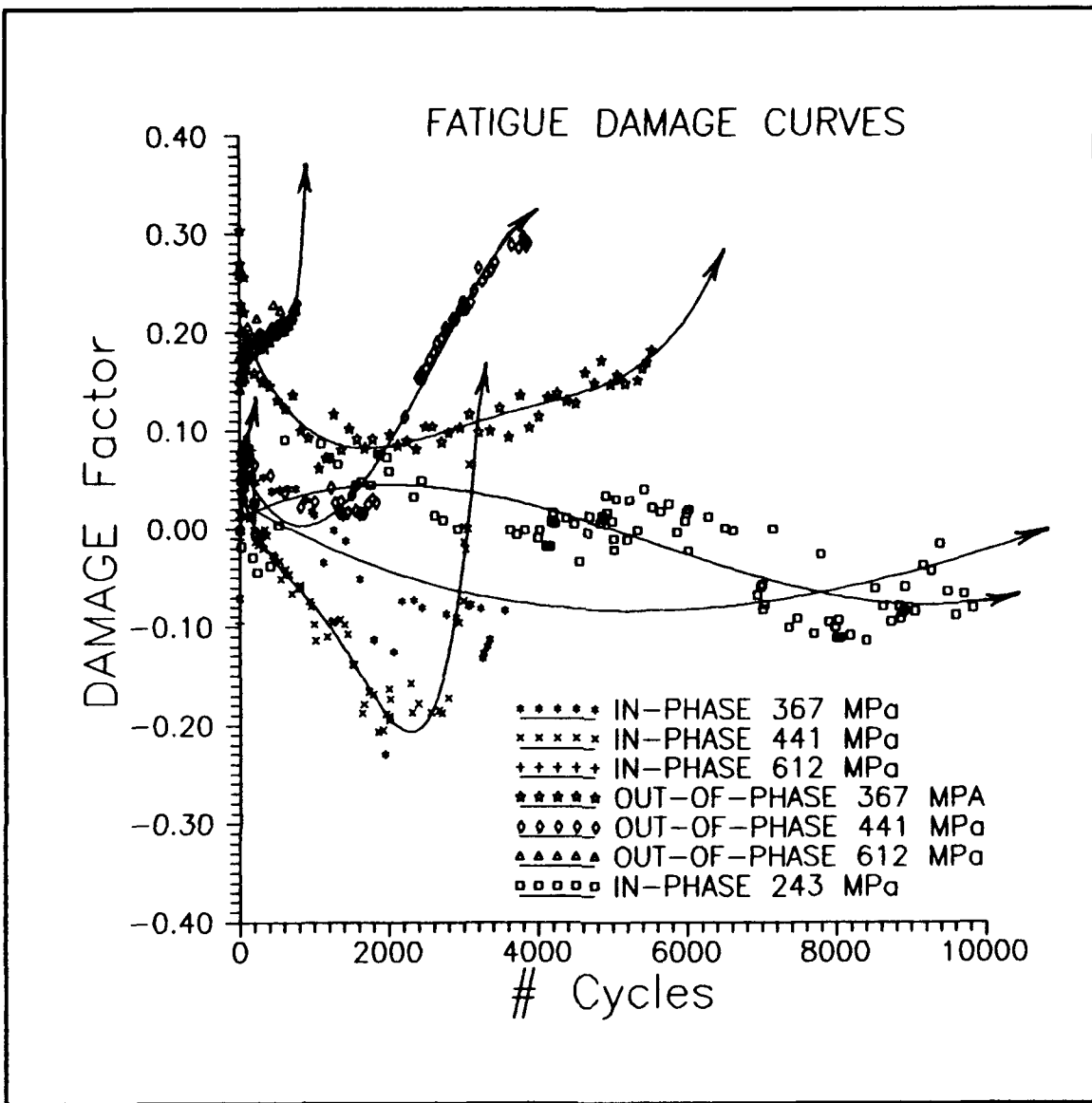


Figure 56. Fatigue Damage Curves Using True  $E_0$

life where damage growth is nearly linear. Figure 55 shows the configuration of a classical damage growth curve. This curve exhibits a definitive linear portion during the bulk of life and a safe operating interval can be determined by structural engineers by monitoring damage such as crack growth throughout a component's life.

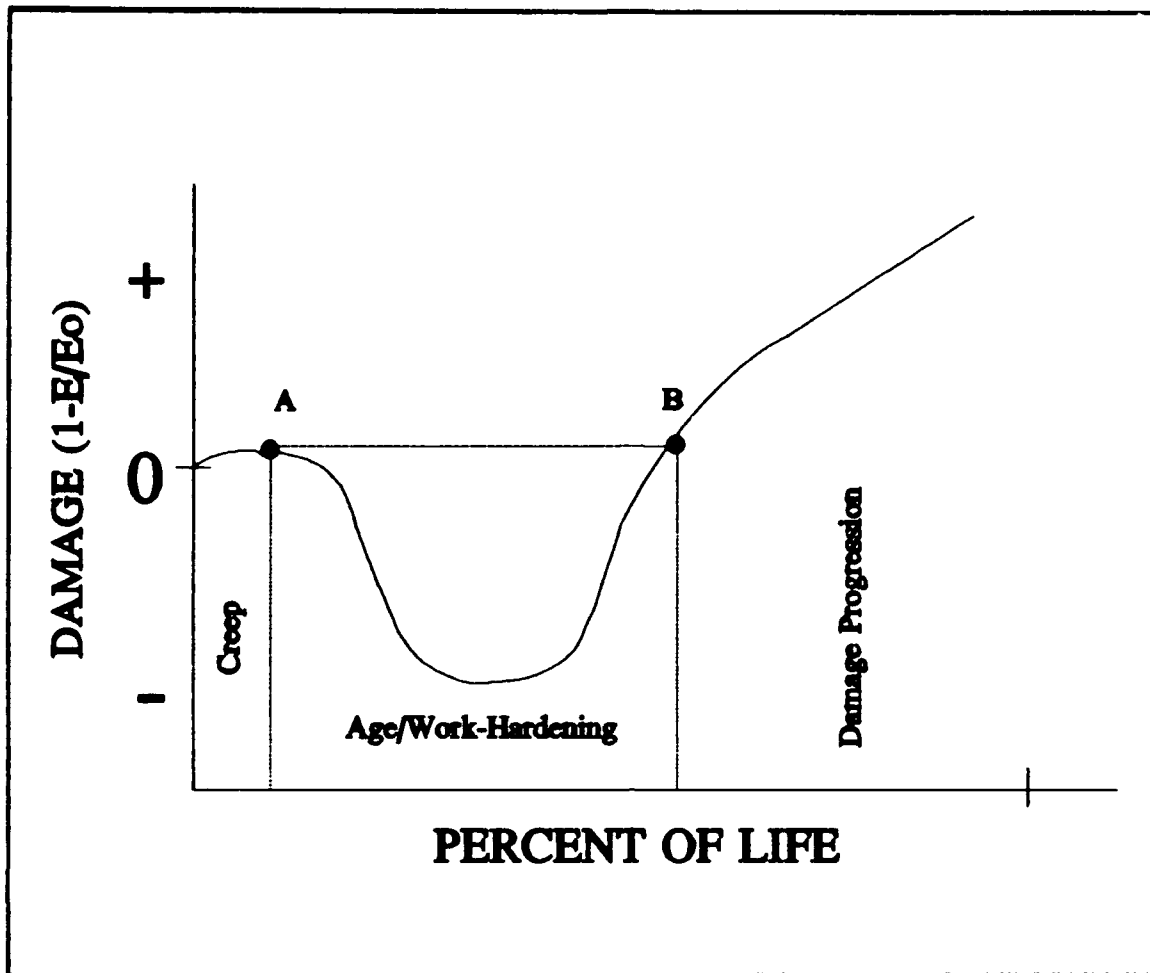


Figure 57. MMC Damage Trend

The damage parameter used in this study is derived from Young's Modulus changes in the relation  $D = (1-E/E_0)$  where  $E$  defines instantaneous modulus and  $E_0$  defines initial modulus. Damage curves for all but the highest load tests conducted in this study show a negative damage trend during an initial portion of life due to modulus increase. Figure 56 shows the results of plotting this function versus cycles. For discussion purposes, a general trend is shown in Figure 57. The decrease in  $D$  (or proportional increase in modulus) is

explained by aging at elevated temperature or work-hardening due to plastic work. High load tests did not exhibit such trends due to the immediate and high rate of damage progression. The phases shown in Figure 57 describe dominant mechanisms (as described in Chapter IV) in modulus change and are assumed independent of each other for the present discussion. It should be stated that all mechanisms may be working throughout a given test with only one factor dominating at a time.

If there were no work hardening involved in a test, as in the case of a specimen aged or worked prior to testing, two independent variables, creep and damage, may be used to predict remaining life in a model such as one proposed by Robinson (21:721):

$$\sum_1^n \frac{N_i}{N_{f_i}} + \sum_1^n \frac{t_i}{t_{r_i}} = 1 \quad (8)$$

where  $n$  is the number of unique stress levels

$N_i$  is portion of life used at the given stress level  
independent of creep

$N_{f_i}$  total fatigue life at the given stress level  
independent of creep

$t_i$  portion of creep to rupture time used  
 $t_{r_i}$  total time to creep rupture

To the author's knowledge there have been no models to handle

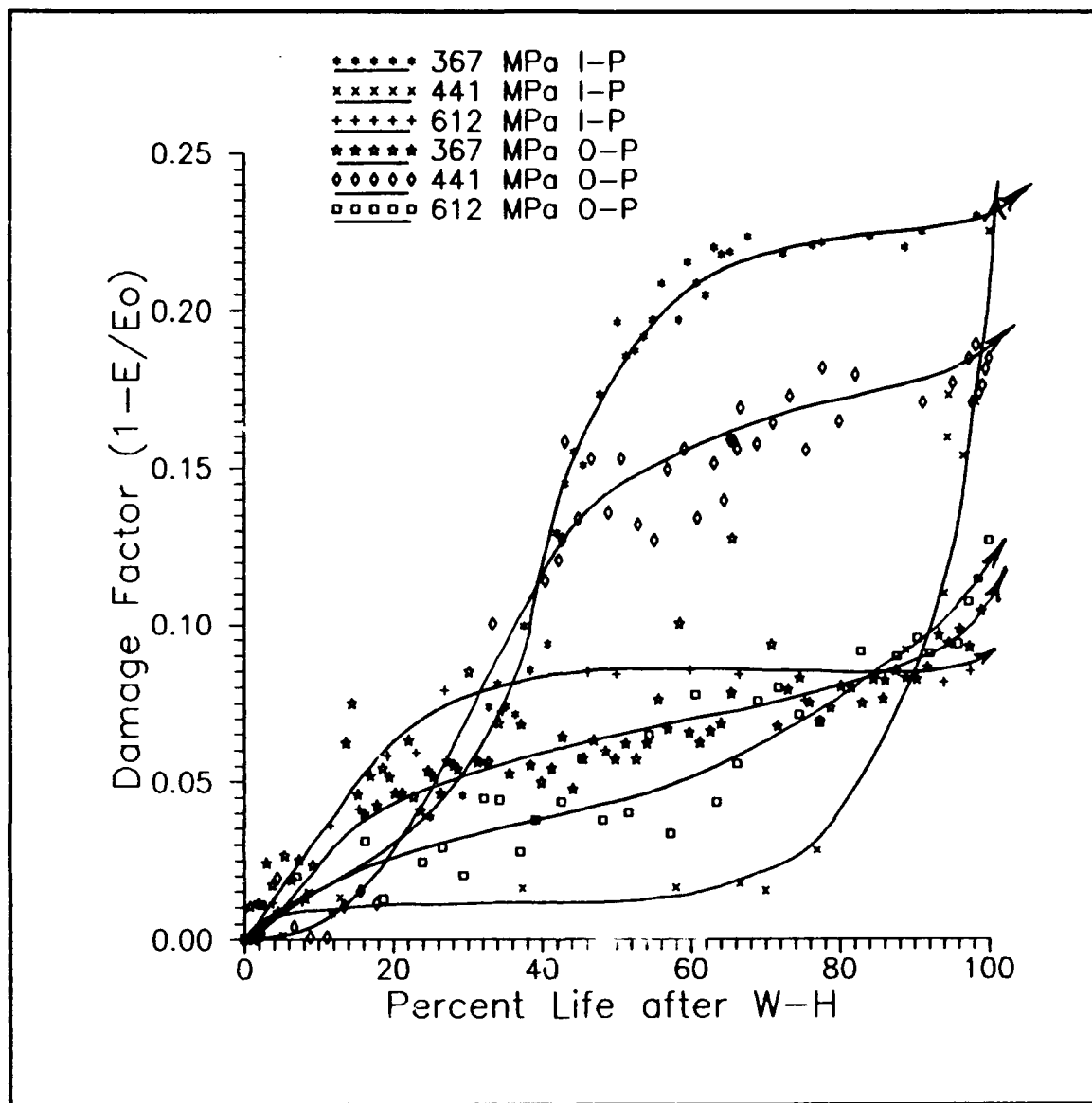


Figure 58. Damage vs. Remaining Life after W-H Phase

the age/work hardening phenomenon during tests. Therefore, an attempt was made to effectively remove the initial damage and W-H portions of the damage curves to form a damage vs effective life after work hardening (W-H) curve. The method used to eliminate these portions of the curve was to use a modulus  $E_0'$  where its value is an effective initial modulus

after any first cycle or initial softening of the specimen has occurred. Points A&B in Figure 57 show this  $E_0'$  location graphically. For data reduction, a numerical cyclic limit set for this parameter was chosen at approximately 20 cycles for those tests with W-H. This cycle count allowed any strain transients to settle and a first peak in damage was reached. A value of 5 cycles or less was used in higher load tests due to most damage occurring in the first cycle with little or no softening occurring before damage progression. No apparent W-H in these tests allowed for curves to be plotted directly from this point. Fatigue cyclic life is then measured from the point where the modulus once again reaches the  $E_0'$  point after W-H (point B - Figure 57). At this point it is assumed all W-H has been offset by damage progression and any additional W-H will be insignificant relative to crack damage progression in the curve. D is then given by  $D = (1-E/E_0')$  and percent life is given by  $P.L. = (\text{current # cycles after W-H})/(\text{Total # cycles after W-H})$ . The resulting damage curves from these calculations are shown in Figure 58. These normalized curves more closely represent the classical damage curve shown in Figure 55. A maximum damage value range appears for the lower load IP tests (367 MPa IP and 441 MPa IP) at around 0.22. In the cases of the high load tests (612 MPa IP/OP), a maximum range appears at 0.09-0.12. Inconsistencies arise in the cases of 367 and 441 MPa OP

maximum stress. These cases fail at values of 0.12 and 0.18, respectively. If all the cases are divided into two categories with one above FPF strength and the other below FPF strength, the D-range for the above FPF group was 8-13% and below FPF was 12-22%. It should be noted here that the lower load tests have a great range of scatter while the higher loads demonstrate a tighter distribution. The approximate 10% difference in maximum failure damage between these two groups can be attributed to the magnitude of initial damage between the high load and low load class of tests. An initial difference between  $E_0$  and  $E_0'$  for each specimen of 1-3% is noted for low load tests while a difference of 8-14% was noted for the high load tests. If this offset is added back to the individual high load test damage curves, all curves except the 367 OP test tend to coalesce near a 20% damage value. No direct correlation was found between fracture surfaces and the values of damage at failure.

The distributed range of values at these end points is consistent with observations (28:69) of CD models' stochastic properties noted earlier. In fact, the wider range of values at lower loads is also consistent with the fact that in the case of slow accumulation of damage, initial damage values have a much greater impact on conditions at failure of the specimens.

## VI. Conclusions and Recommendations

This study discussed, in detail, the results of a systematic study of damage mechanisms in a cross-ply MMC under TMF loading conditions. A computer controlled test system was employed and strain data was recorded under in-phase and out-of-phase TMF. Instantaneous Young's Modulus was calculated using this strain data and a damage parameter was developed to measure effective remaining life for given test conditions.

The conclusions drawn from this study can be summarized as follows:

- 1) The existing TF system was expanded to perform TMF testing
- 2) The high temperature extensometer readings exhibited drift under night and day temperature conditions. Extensometer strain instrumentation temperatures drifted due to air cooling temperature variations and in turn caused drifting in absolute strain measurements at low loads. No effect on  $\Delta\epsilon_p$  was noted.
- 3) The fatigue damage threshold limit was shown to correlate with 90° matrix stresses. This limit is independent of frequency, temperature, or phasing conditions.
- 4) Fiber-matrix interface zones are major players in the fatigue progression and re-direction in both high load and extended length tests. Interfaces have little effect on

relatively short duration or mid-level load tests.

5) At high load conditions fatigue life for in-phase (IP) TMF tests is shorter at a given applied stress level than out-of-phase (OP) tests. At low loads OP has less fatigue life than IP. There is an S-N curve cross-over point near 90% of predicted FPF (441 MPa - applied).

6) Maximum total strain at failure is greater for IP tests than OP indicating greater overall damage or plastic deformation prior to failure. By eliminating thermal strains, a critical strain  $\epsilon_c$  of 0.0075 mm/mm can be related to both IP and OP tests.

7) Thermal cycling to 10,000 causes macroscopic longitudinal edge crack damage, but there were no indications of macroscopic material property (CTE) changes.

8) Reaction zone size increases with thermal cycling but begins to stabilize between 5000-10000 cycles. Separation of the fiber and matrix interface occurs, with little additional growth in size of the reaction zone, by 28000 thermal cycles.

9) Primary fatigue damage mechanism in all tests was transverse cracking originating in the 90° ply reaction zones and progressing outward to the surface at failure.

10) Use of the replica technique during testing proved to be a good indicator of internal transverse cracking of the matrix. Cracking of surface 0° fibers proved to be less consistent with the amount of internal fiber cracking.

11) Instantaneous Young's Modulus can be monitored to provide a consistent damage parameter at failure.

Recommendations can be summarized as follows:

1) The air-cooled extensometer should be modified to use a temperature-regulated air system or be water-cooled to provide drift-free strain data at low loading conditions.

2) Additional tests should be run at low load conditions to better define the empirical distribution of failure life and damage at failure.

3) Heat-treated specimens should be tested and compared to previous results to determine extent of influence of work-hardening on damage curves and modulus change.

4) Varied combinations of loads should be used to test the proposed model. Ordering of load could be very important to fatigue life. Assumptions of the current model show fatigue life to be path independent. .

5) A study of effective load ratio  $R$  in matrix/fiber microstresses should be accomplished. Results from METCAN show some  $R$ 's for the matrix under these test conditions can be as high as .88 - effectively a static load.

## Appendix A

### Constituent Microstress Data From METCAN

The first four pages of this Appendix contain the property values used in the METCAN program to calculate microstresses in this MMC. Fiber volume ratio used ( $V_f$ ) was .386. Manufacturing cooldown of  $1000^{\circ}\text{C}$  to  $22^{\circ}\text{C}$  (1832 to  $70^{\circ}\text{F}$ ) was incorporated similar to Gabb et. al. (8). Stresses in the constituent materials are assumed to be zero at the  $1000^{\circ}\text{C}$  temperature value. Individual microstresses were calculated for each ply and each constituent material. Stresses for the matrix material are calculated using the three zones of the multi-cell model. From the multi-cell model described in the text,  $\sigma_{11}/\sigma_{22\text{M}}$  stresses were determined to be the maximum  $0^{\circ}$  fiber and  $90^{\circ}$  matrix stresses encountered, respectively.

Data contained in this Appendix is shown in charts formatted for Stress (GPa) vs. Time Increment. Time increments for all charts should be read as follows:

0-1: Factory cooldown from  $1000^{\circ}\text{C}$  to  $21^{\circ}\text{C}$ .

1-2: Applied stress increase from 0 to  $R=0.1$  level.

In-phase - Temperature increase from  $21^{\circ}\text{C}$  to  $149^{\circ}\text{C}$ .

Out-of-phase - Temp increase from  $21^{\circ}\text{C}$  to  $427^{\circ}\text{C}$ .

2-3: Applied stress increase to Maximum level.

In-phase - Temp increase from  $149^{\circ}\text{C}$  to  $427^{\circ}\text{C}$ .

Out-of-phase - Temp decrease from  $427^{\circ}\text{C}$  to  $149^{\circ}\text{C}$ .

3-4: Applied stress decrease to  $R=0.1$  level.

In-phase - Temp decrease  $427^{\circ}\text{C}$  to  $149^{\circ}\text{C}$ .

Out-of-phase - Temp increase from  $149^{\circ}\text{C}$  to  $427^{\circ}\text{C}$ .

4-5: Repeat 2-3

5-6: Repeat 3-4

METCAN Material Properties Used

FIBER

<u>Property</u>	<u>Units (METCAN)</u>	<u>SICA</u>
DF	MILS	5.600
RHOF	Lb/IN <sup>3</sup>	0.110
TEMPMF	DEG F	4780.
EF11	MPSI	58.00
EF22	MPSI	58.00
NUF12	IN/IN	0.250
NUF2S	IN/IN	0.250
GF12	MPSI	23.80
GF23	MPSI	23.80
ALFAF11	PPM/F	2.290
ALFAF22	PPM/F	2.290
KF11	BTU/HR/IN/F	0.750
KF22	BTU/HR/IN/F	0.750
CF	BTU/LB	0.290
SF11T	KSI	500.0
SF11C	KSI	650.0
SF22T	KSI	500.0
SF22C	KSI	650.0
SF12S	KSI	300.0
SF23S	KSI	300.0

**MATRIX**

<u>Property</u>	<u>Units (METCAN)</u>	<u>TI15</u>
RHOM	LB/IN <sup>3</sup>	0.172
EM	MPSI	9.000
NUM	IN/IN	0.360
ALFAM	PPM/F	4.360
KM	BTU/HR/IN/F	0.390
CM	BTU/LB	0.120
SMT	KSI	130.0
SMC	KSI	130.0
SMS	KSI	90.00
EPSMT	%	12.00
EPSMC	%	12.00
EPSMS	%	12.00
EPSMTO	%	12.00
KVOID	BTU/HR/IN/F	0.019
TEMPMM	DEG F	3000.

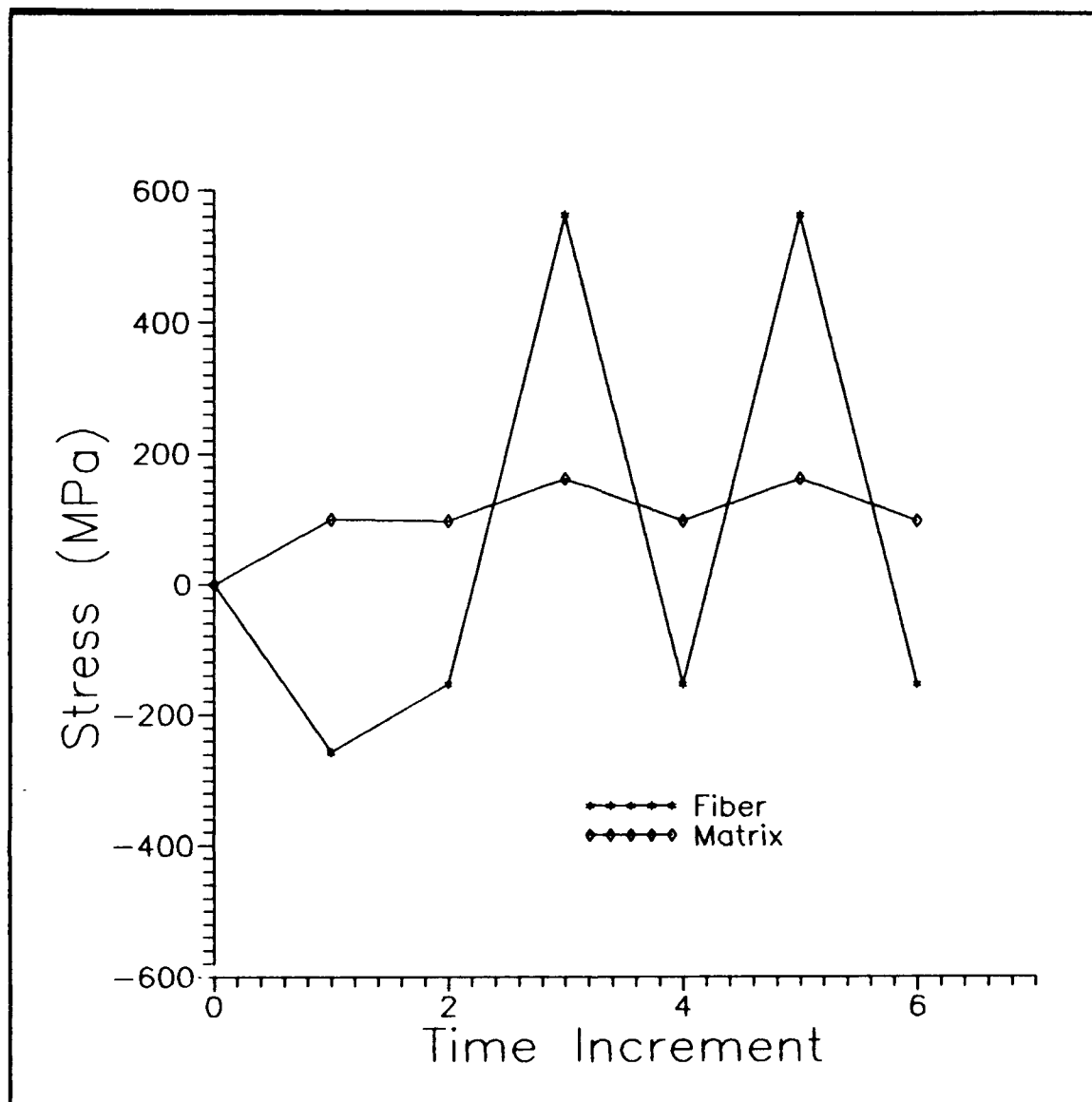


Figure 59. Maximum Stress 248 MPa - In-Phase / 0-degree Ply

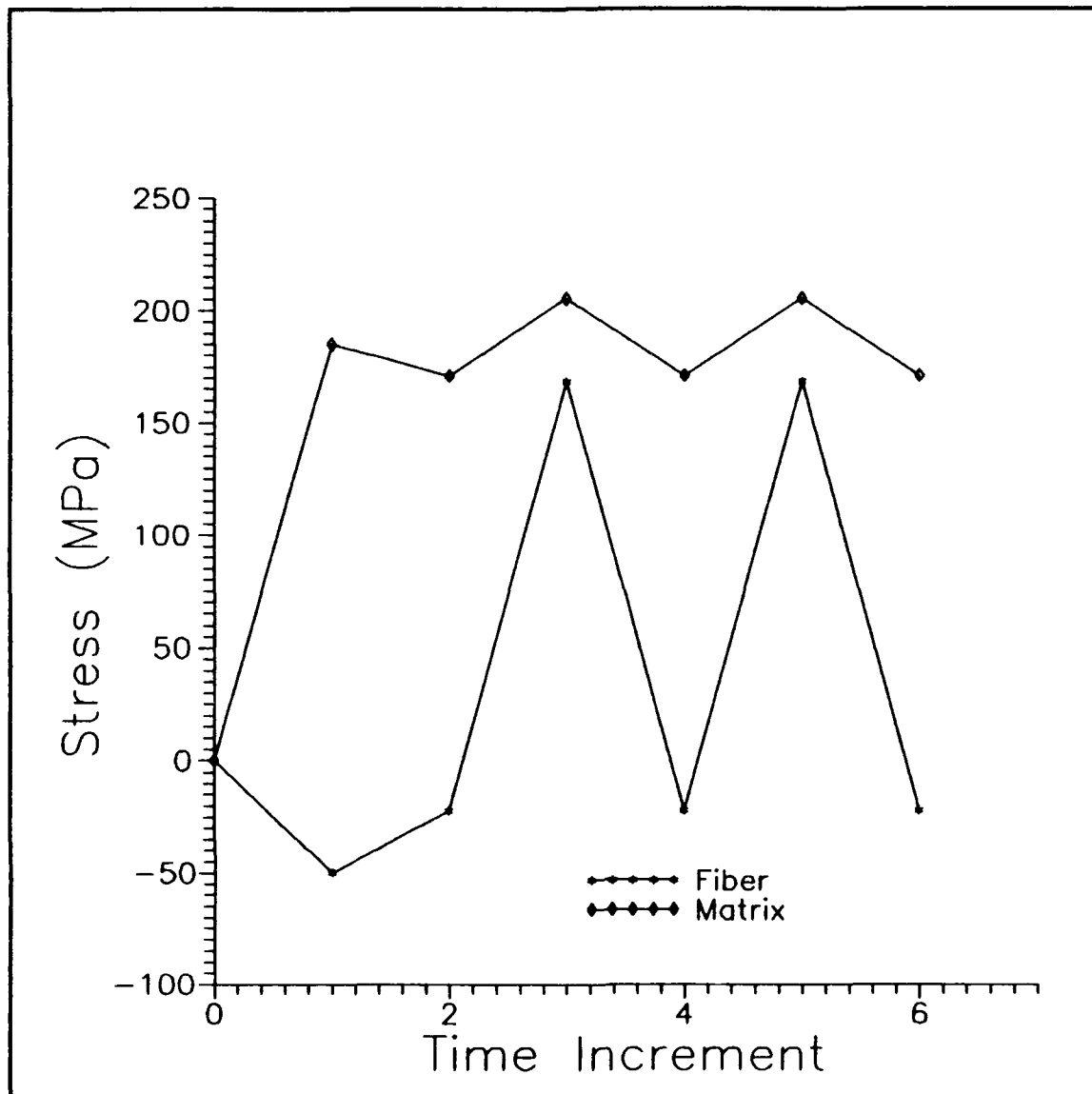


Figure 60. Maximum Stress 248 MPa - In-Phase / 90-degree Ply

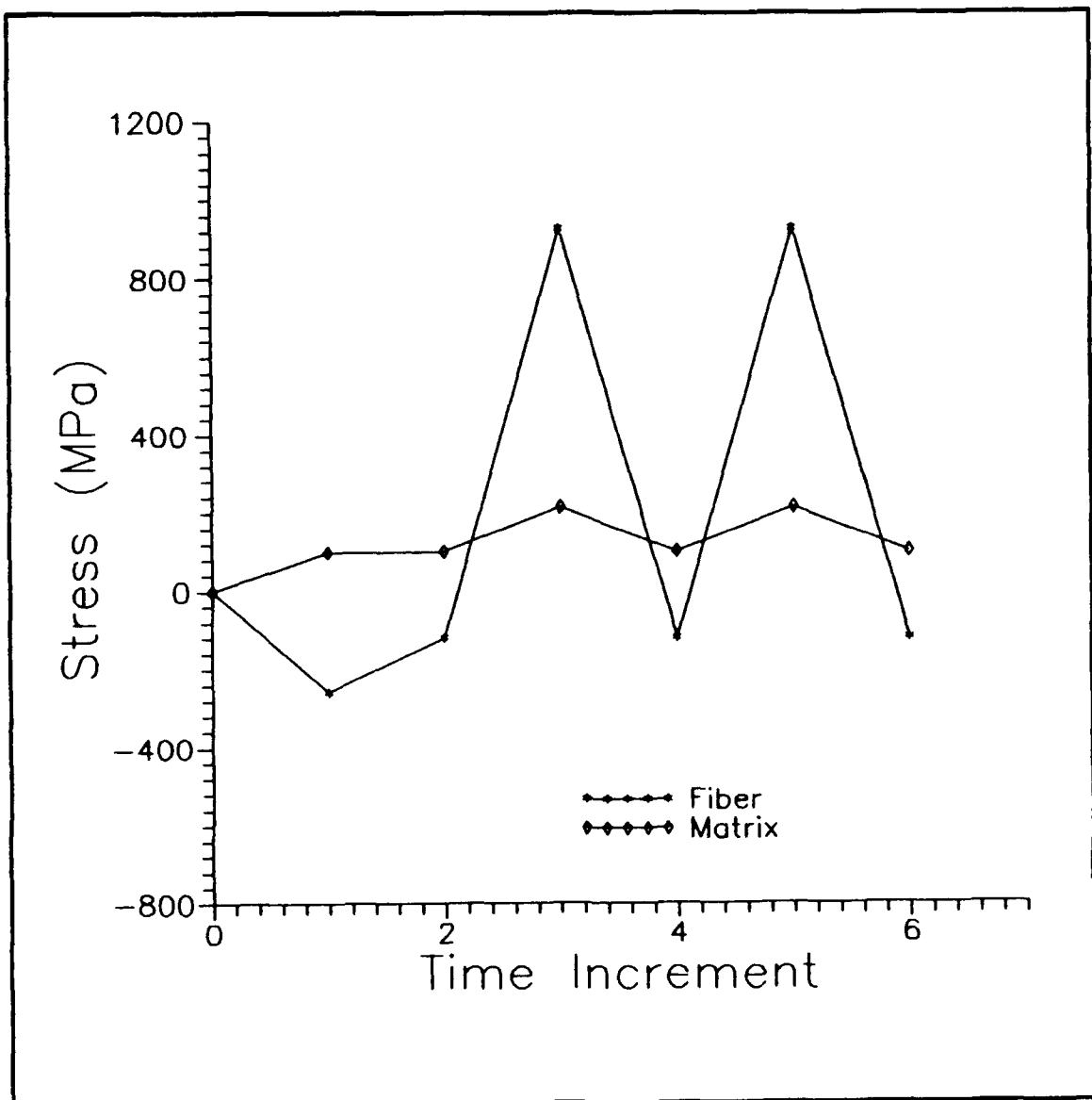


Figure 61. Maximum Stress 367 MPa - In-Phase / 0-degree Ply

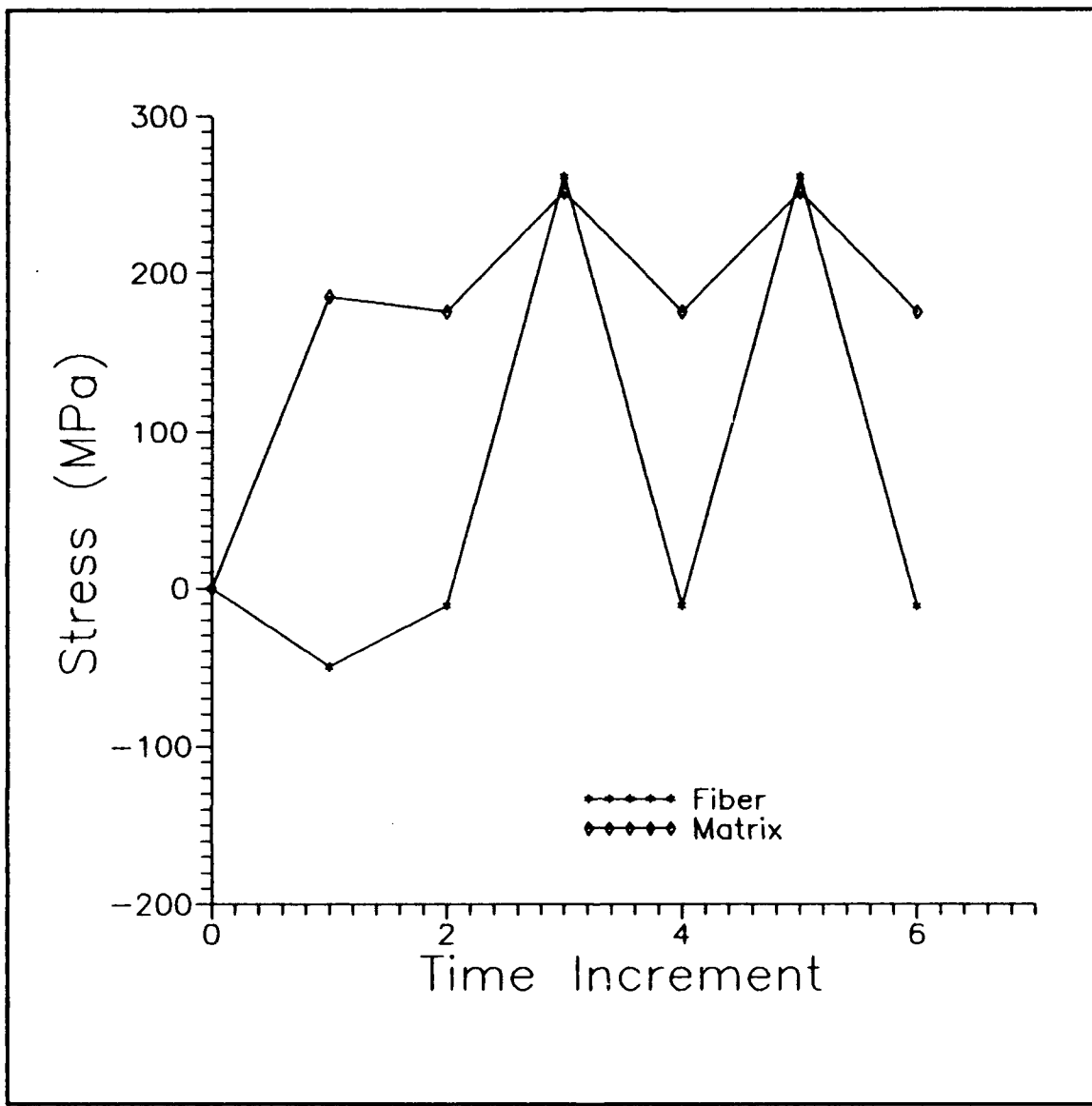


Figure 62. Maximum Stress 367 MPa - In-Phase / 90-degree Ply

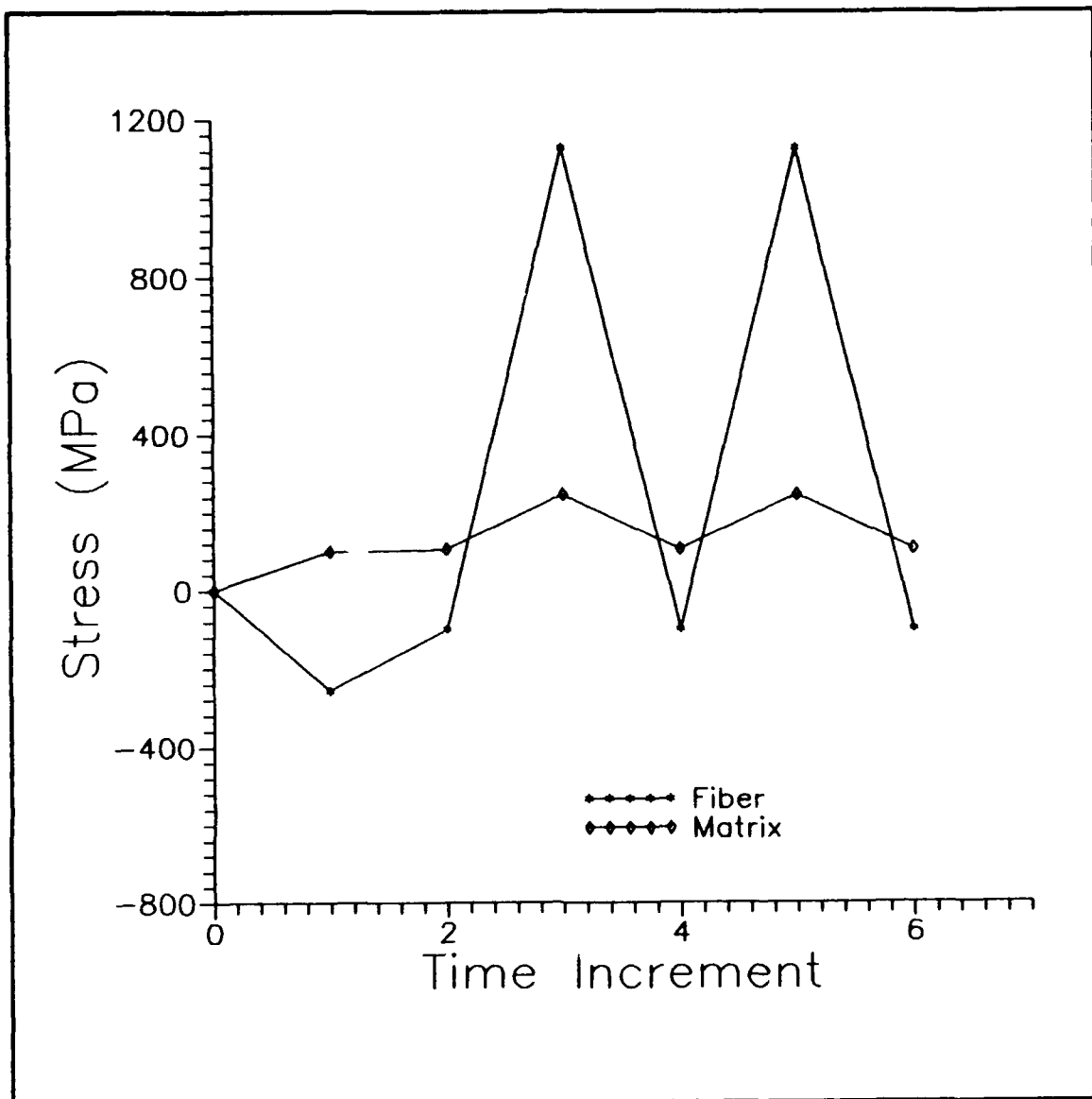


Figure 63. Maximum Stress 441 MPa - In-Phase / 0-degree Ply

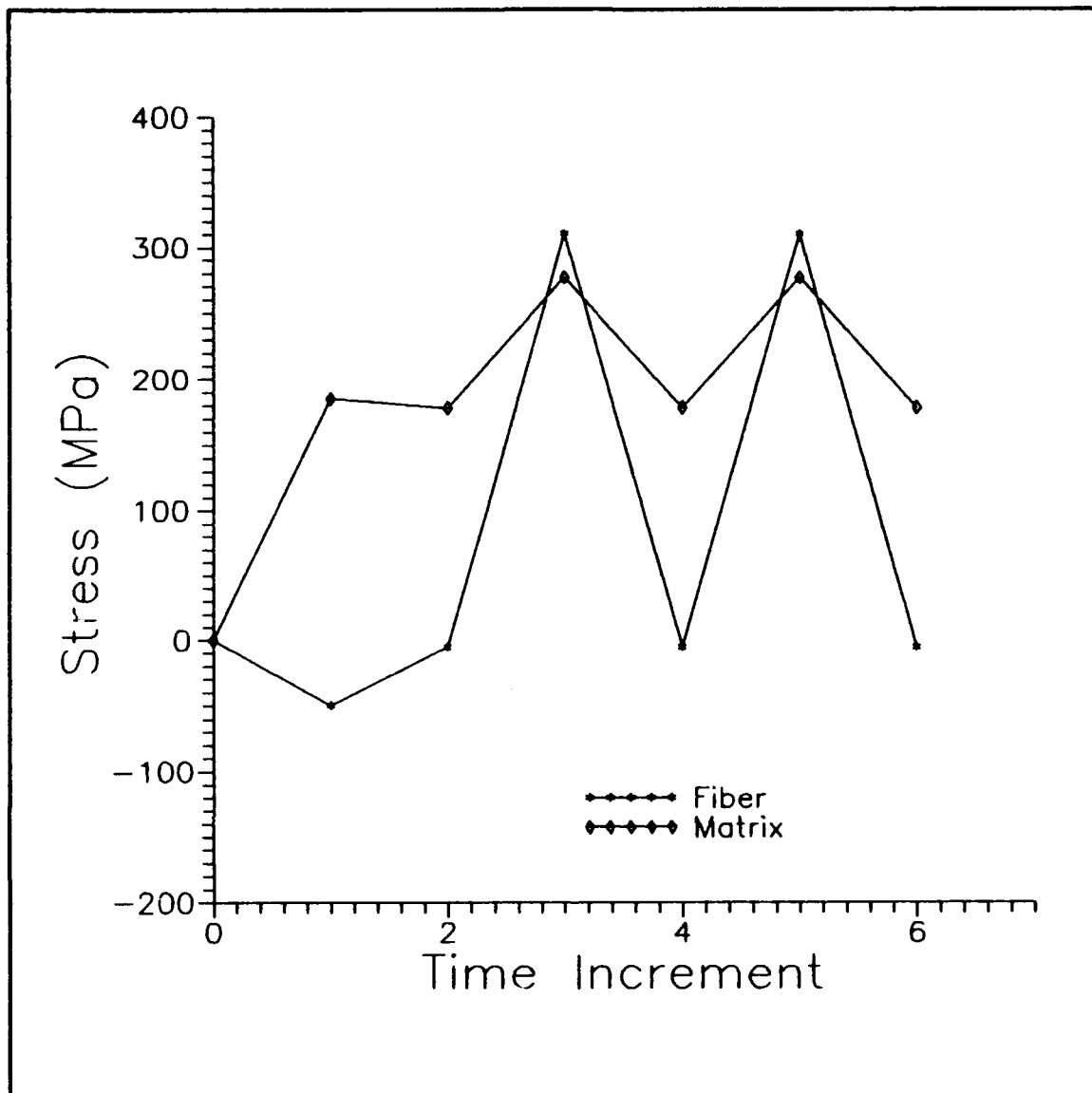


Figure 64. Maximum Stress 441 MPa - In-Phase / 90-degree Ply

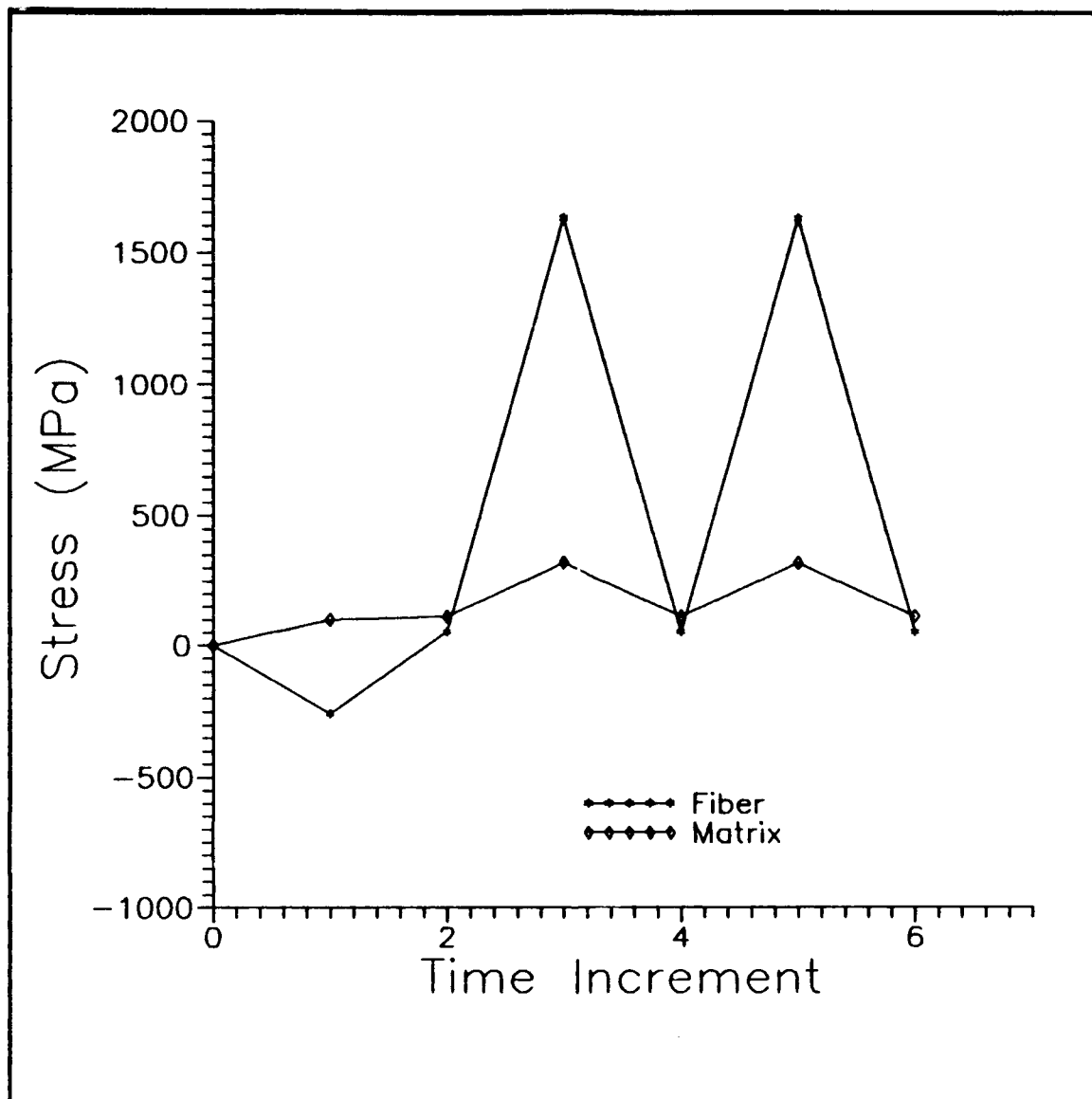


Figure 65. Maximum Stress 612 MPa - In-Phase / 0-degree Ply

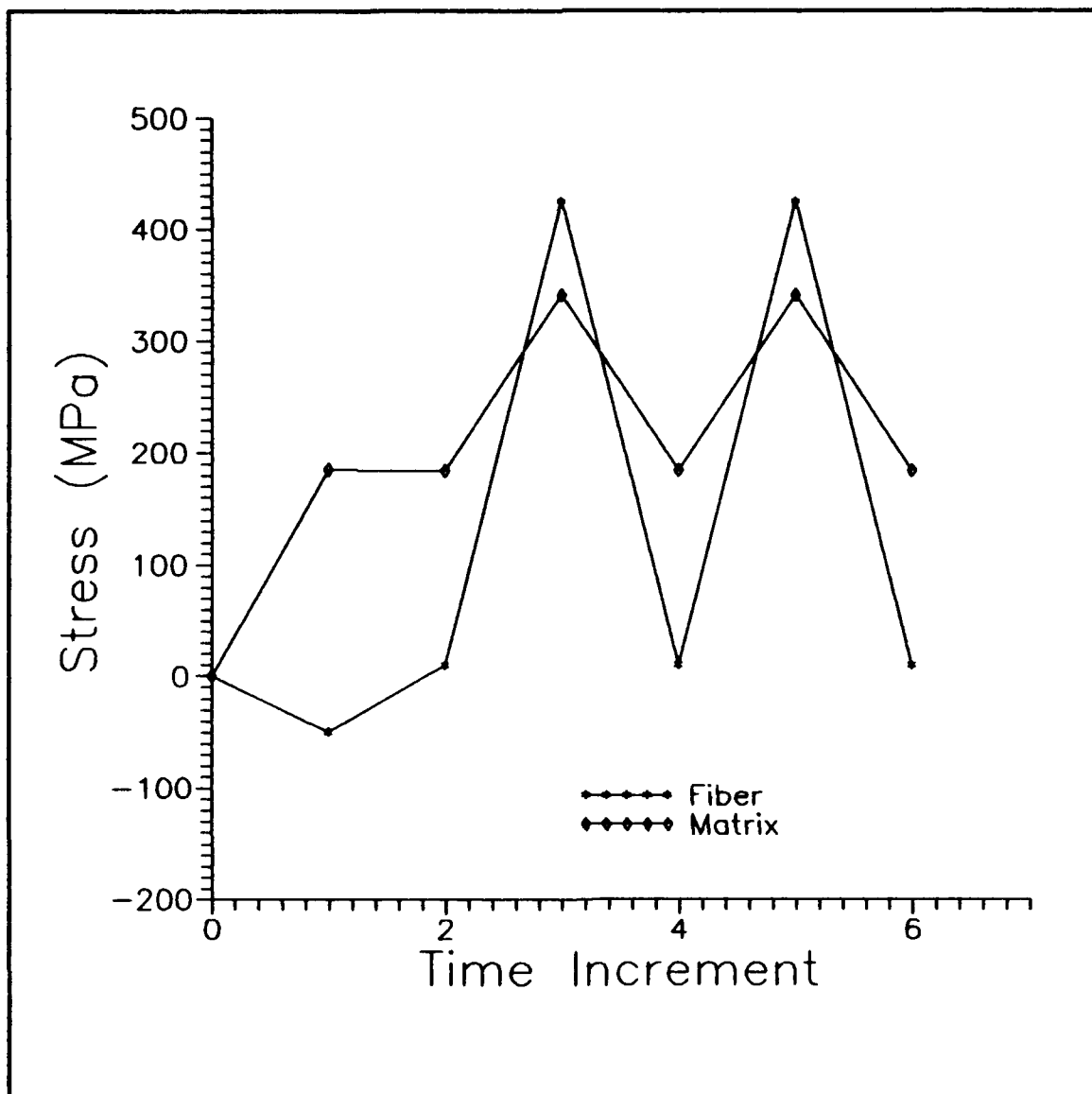


Figure 66. Maximum Stress 612 MPa - In-Phase / 90-degree Ply

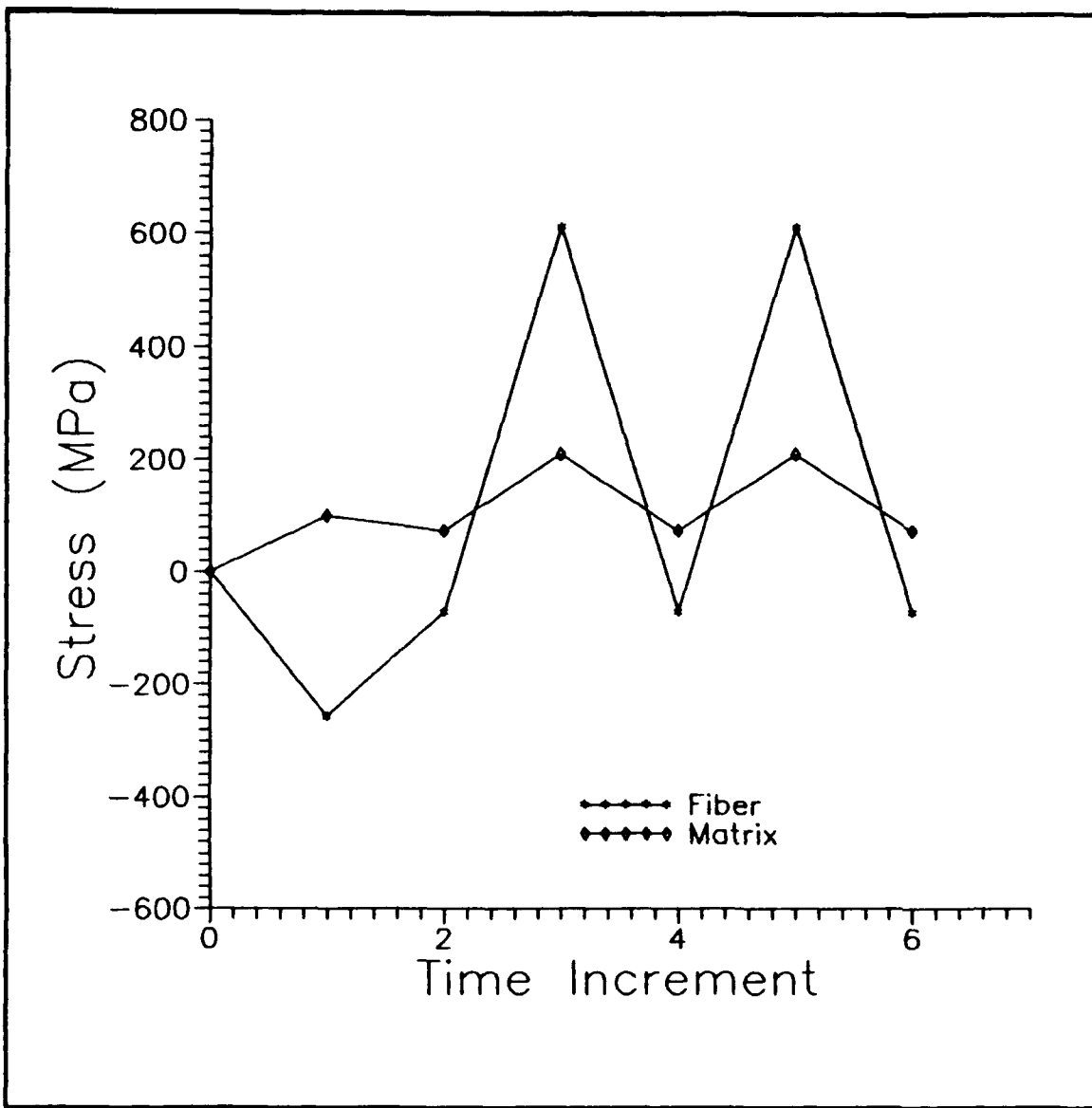


Figure 67. Maximum Stress 293 MPa - Out-of-Phase / 0-degree Ply

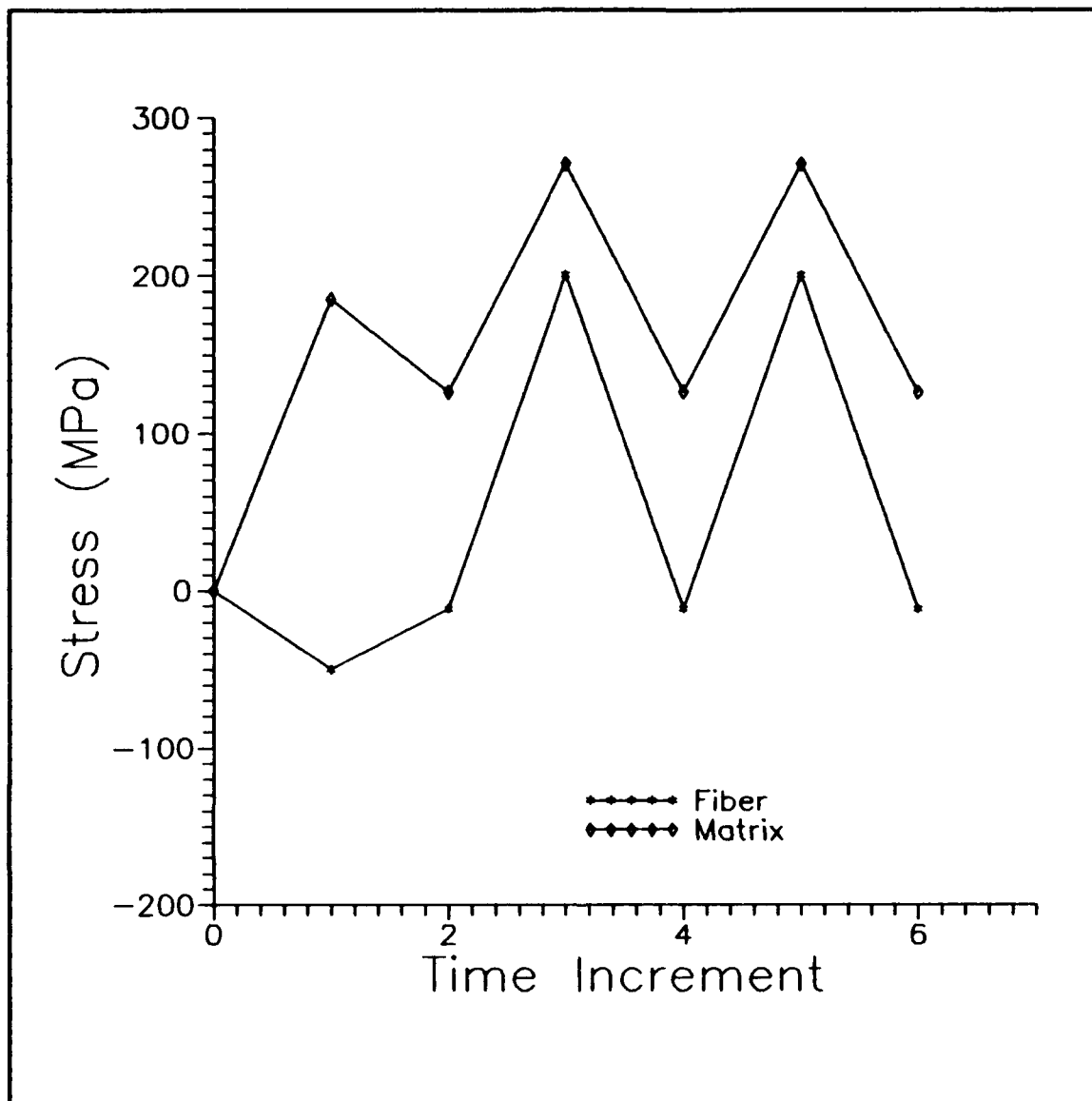


Figure 68. Maximum Stress 293 MPa - Out-of-Phase / 90-degree Ply

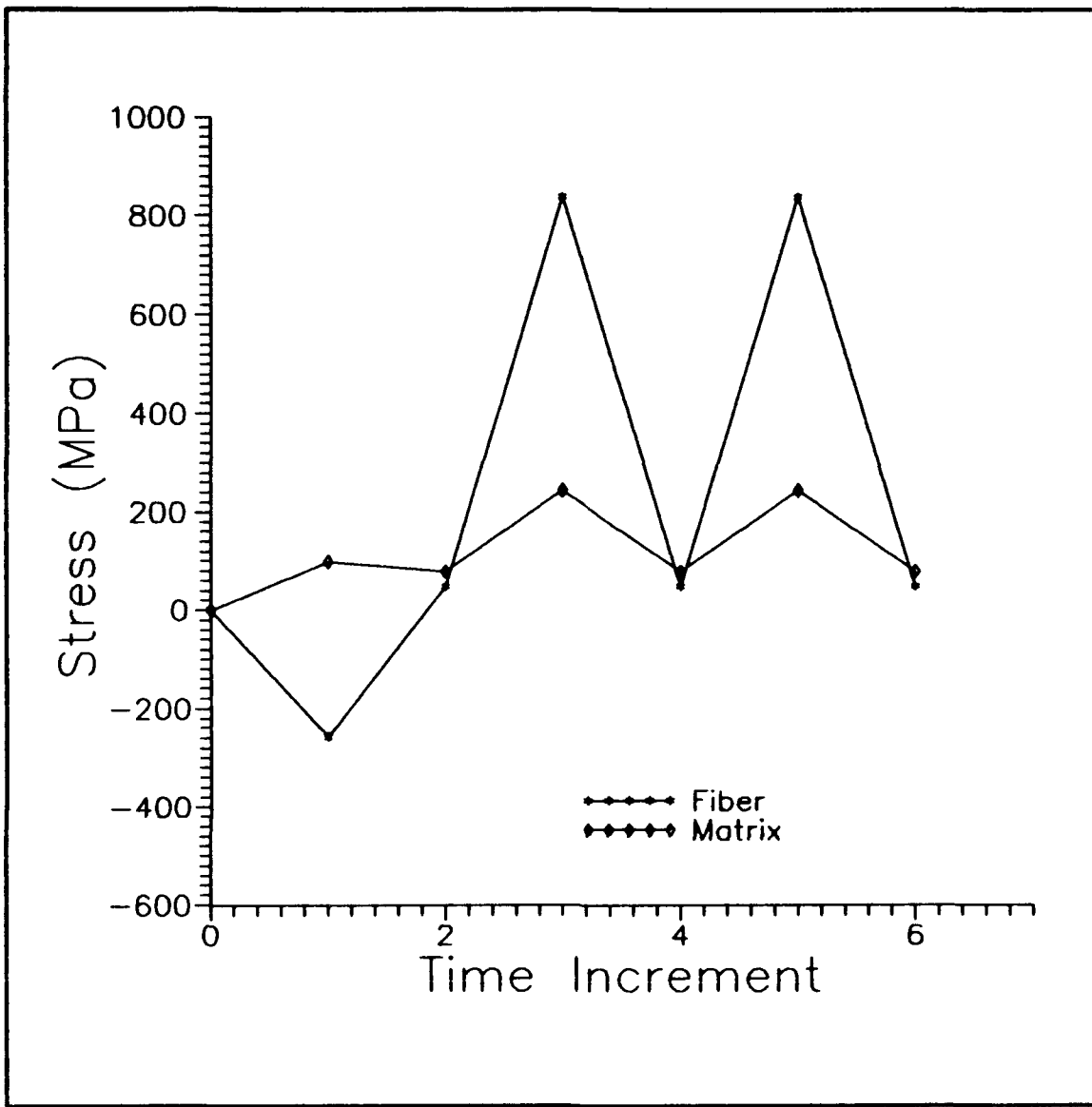


Figure 69. Maximum Stress 367 MPa - Out-of-Phase / 0-degree Ply

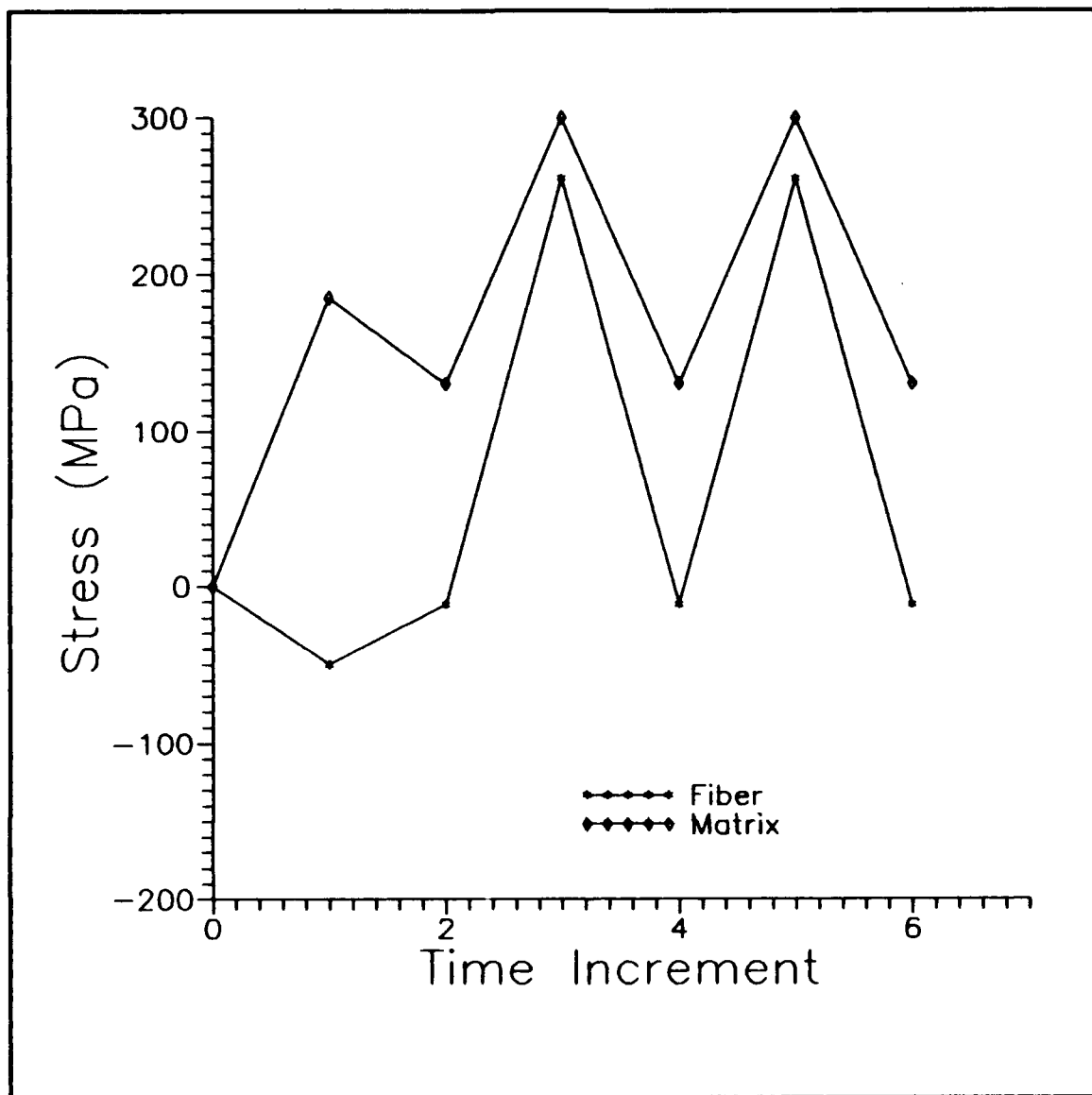


Figure 70. Maximum Stress 367 MPa - Out-of-Phase / 90-degree Ply

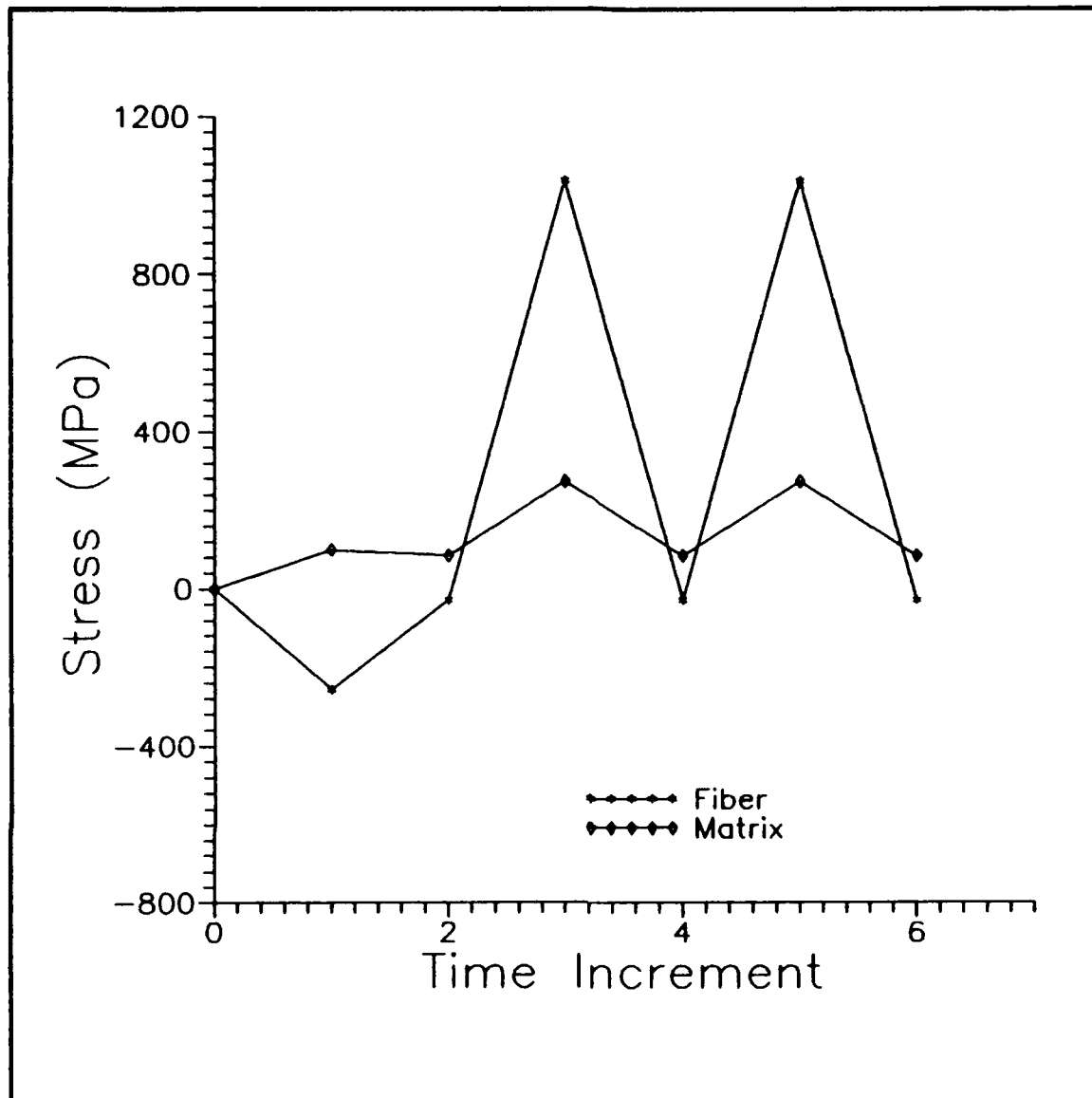


Figure 71. Maximum Stress 441 MPa - Out-of-Phase / 0-degree Ply

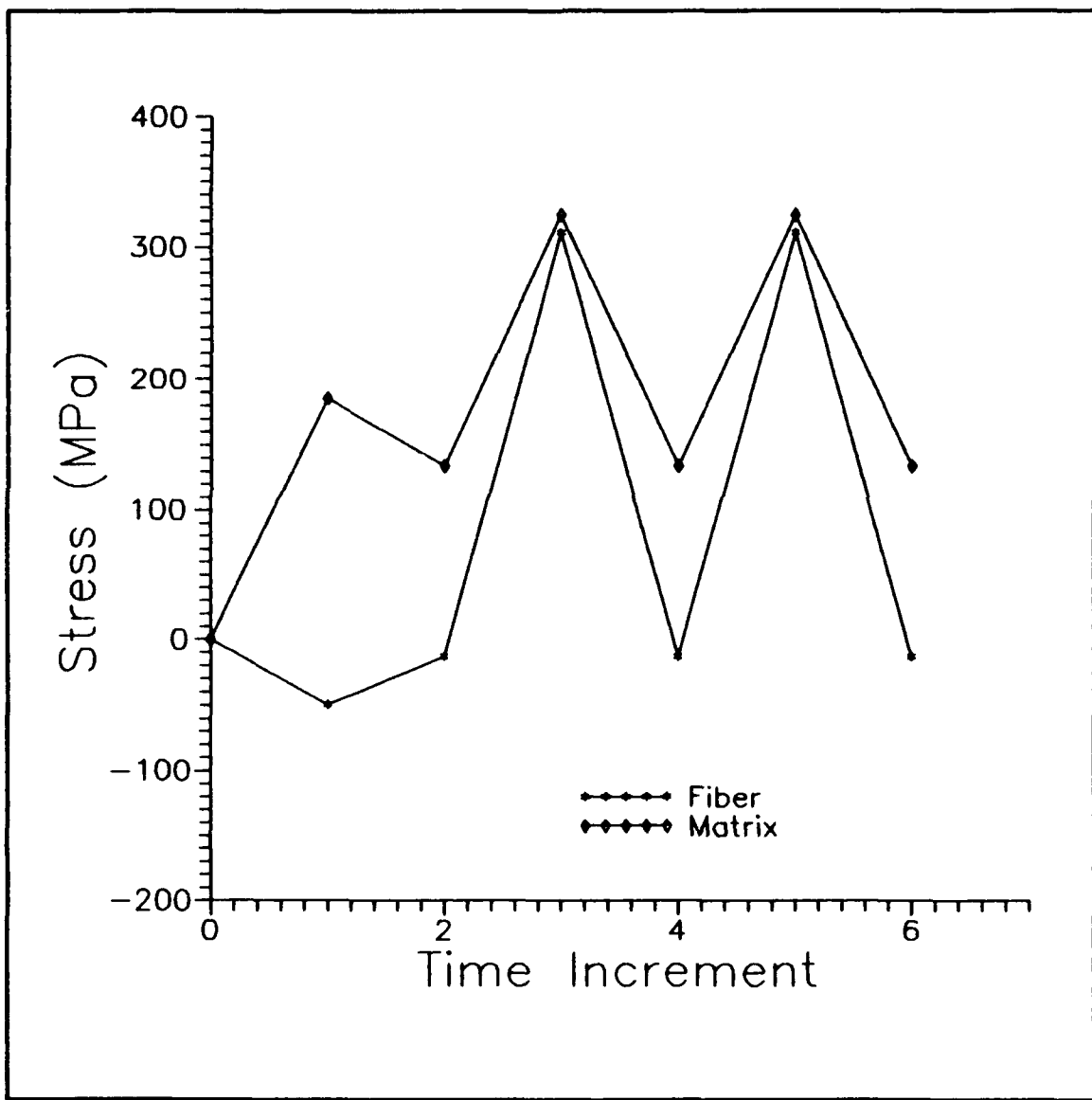
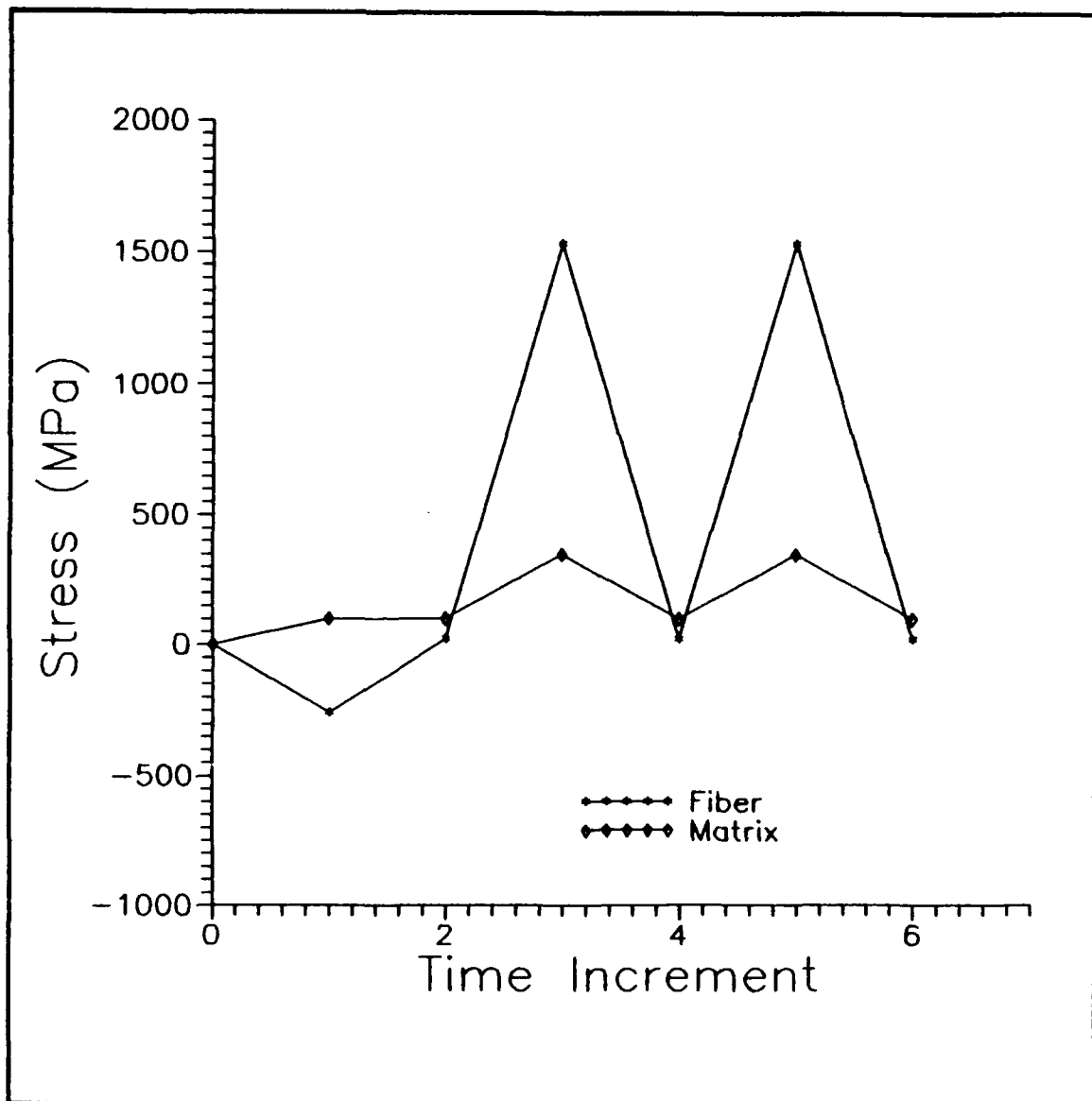


Figure 72. Maximum Stress 441 MPa - Out-of-Phase / 90-degree Ply



**Figure 73. Maximum Stress 612 MPa - Out-of-Phase / 0-degree Ply**

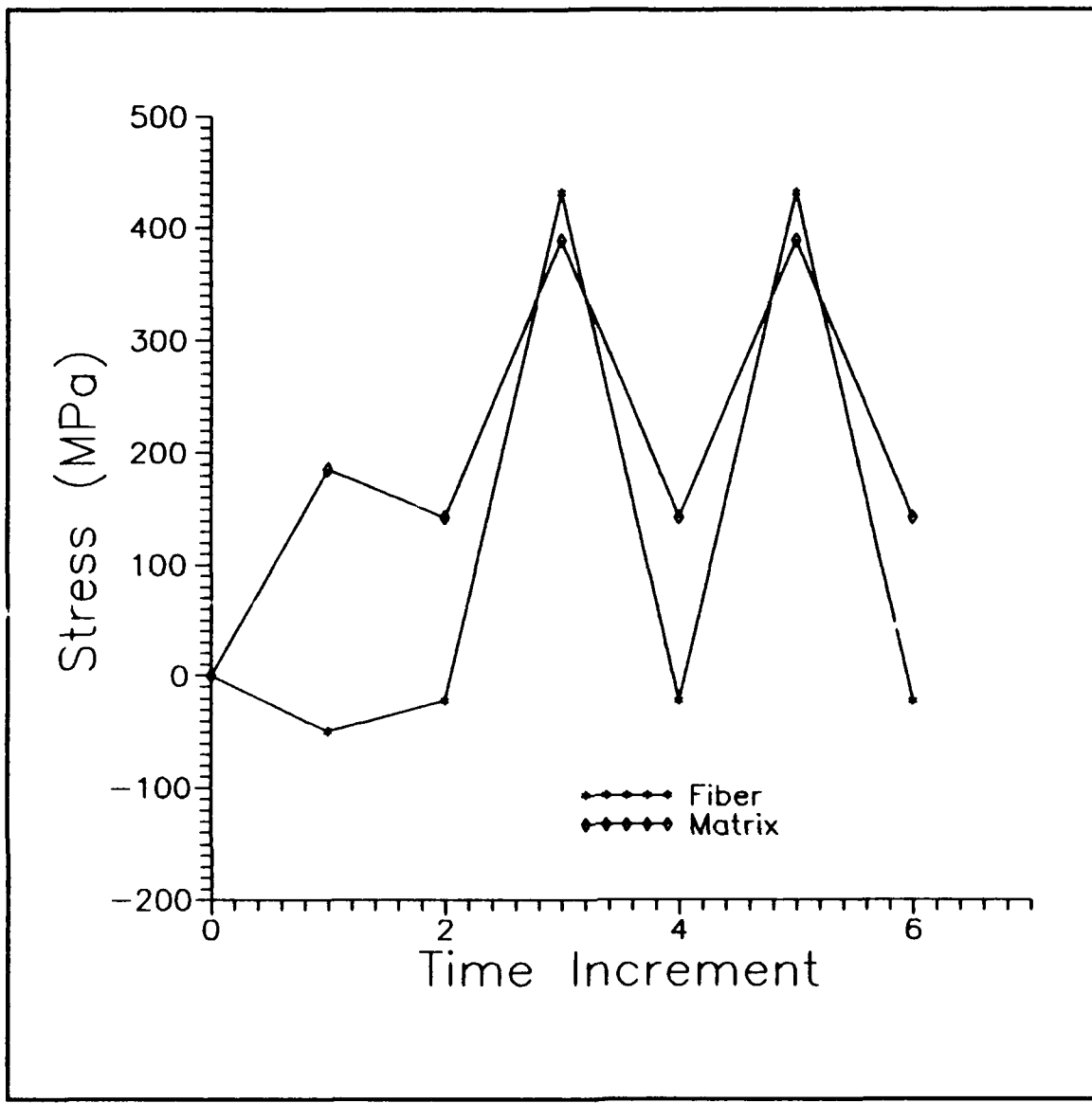
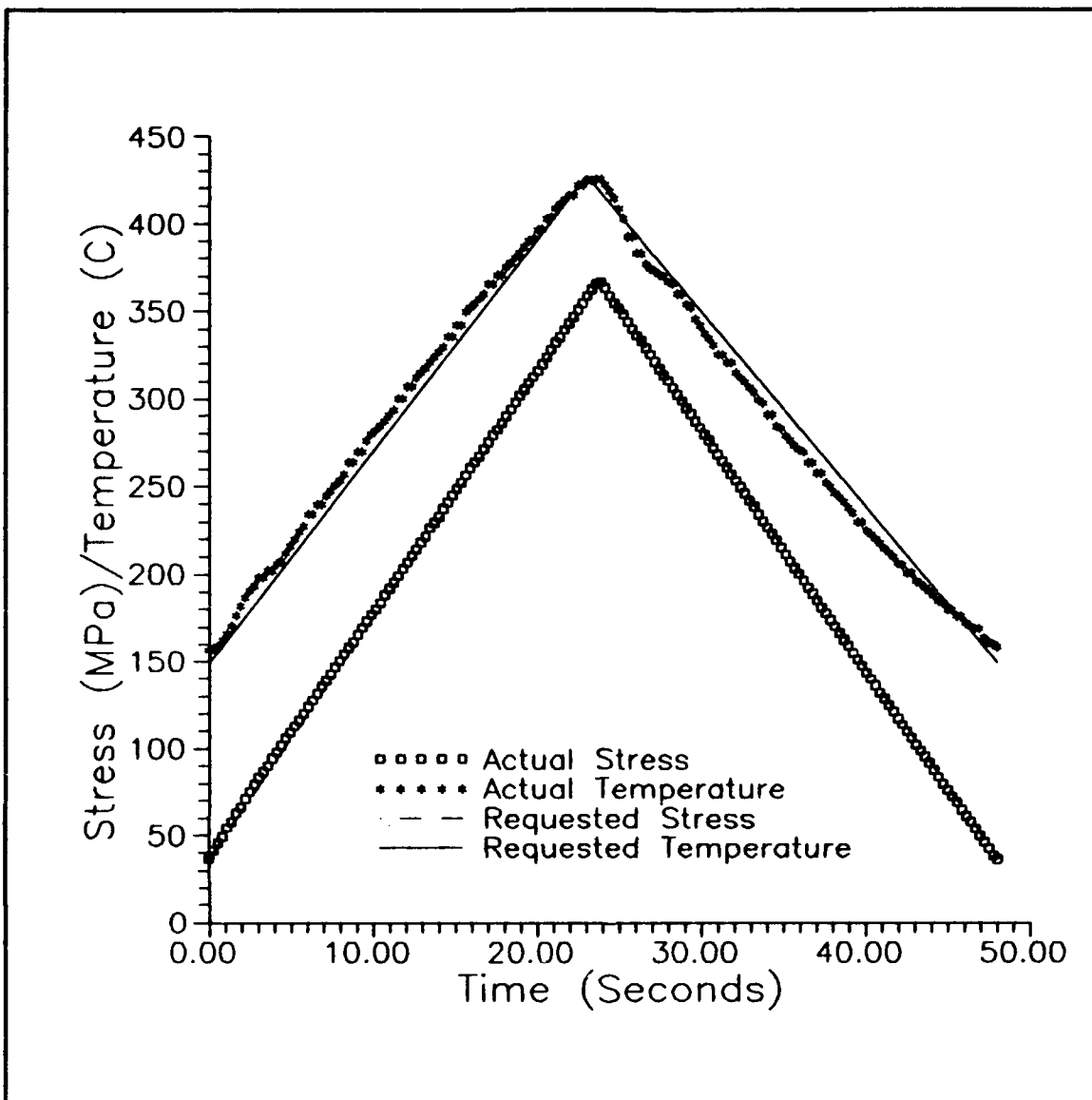


Figure 74. Maximum Stress 612 MPa - Out-of-Phase / 90-degree Ply

**Appendix B**

**Example Actual Stress/Temperature vs. Time Profiles**



**Figure 75. In-Phase Profile Example**

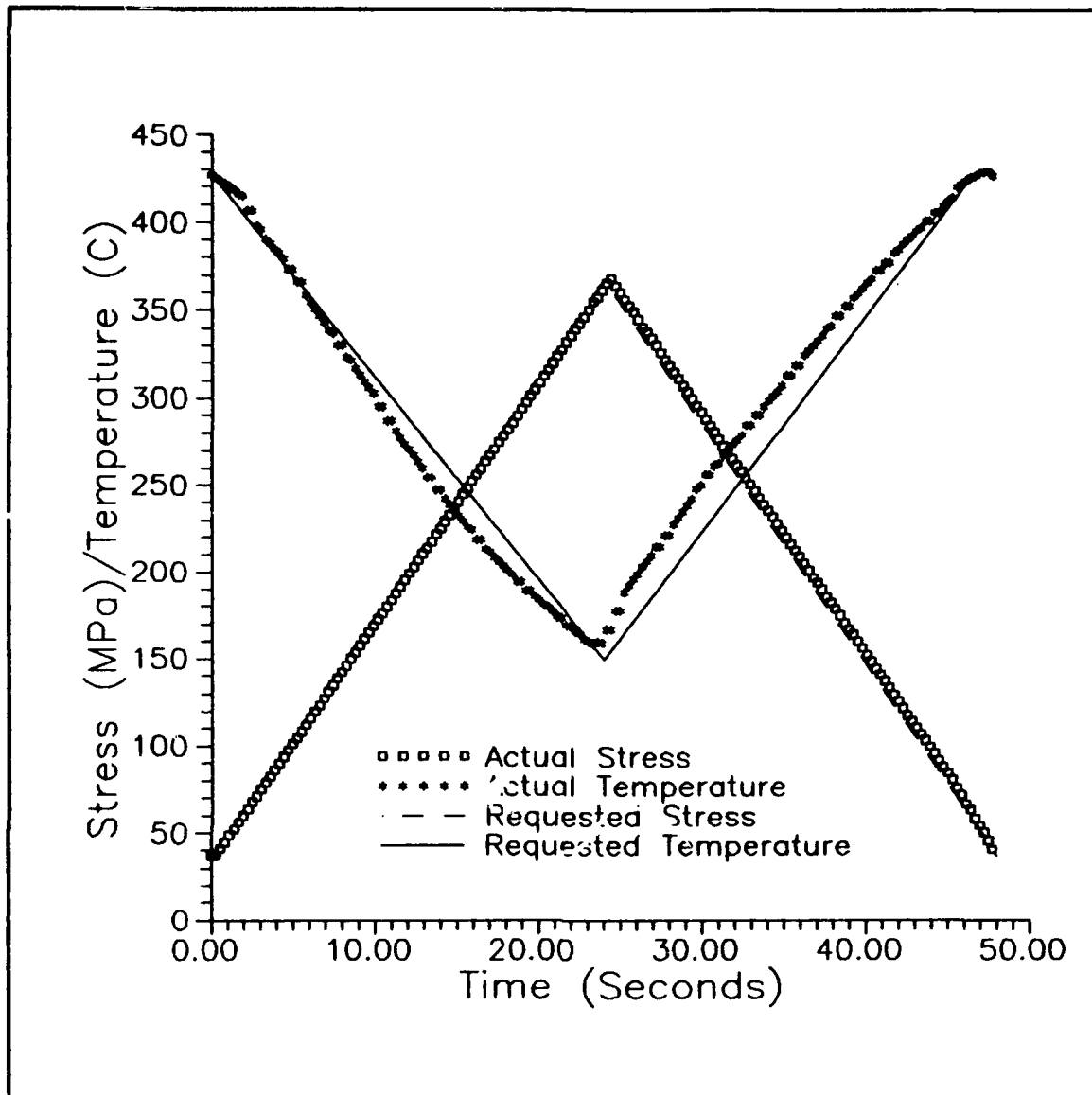


Figure 76. Out-of-Phase Profile Example

## Appendix C

### Additional Data

#### 1. Unfailed Specimen Modulus Data

#### 2. Example Strain Progression Data

The following representative strain hysteresis loops are given for each respective test (cycle numbers vary due to data acquisition frequency variance):

441 MPa I-P - Cycles 4, 13, 24, 3069  
612 MPa I-P - Cycles 1, 7, 21, 180  
367 MPa O-P - Cycles 1, 10, 13, 46, 2182, 5492,  
5524  
441 MPa O-P - Cycles 1, 13, 57, 3864  
612 MPa O-P - Cycles 1, 6, 29, 767

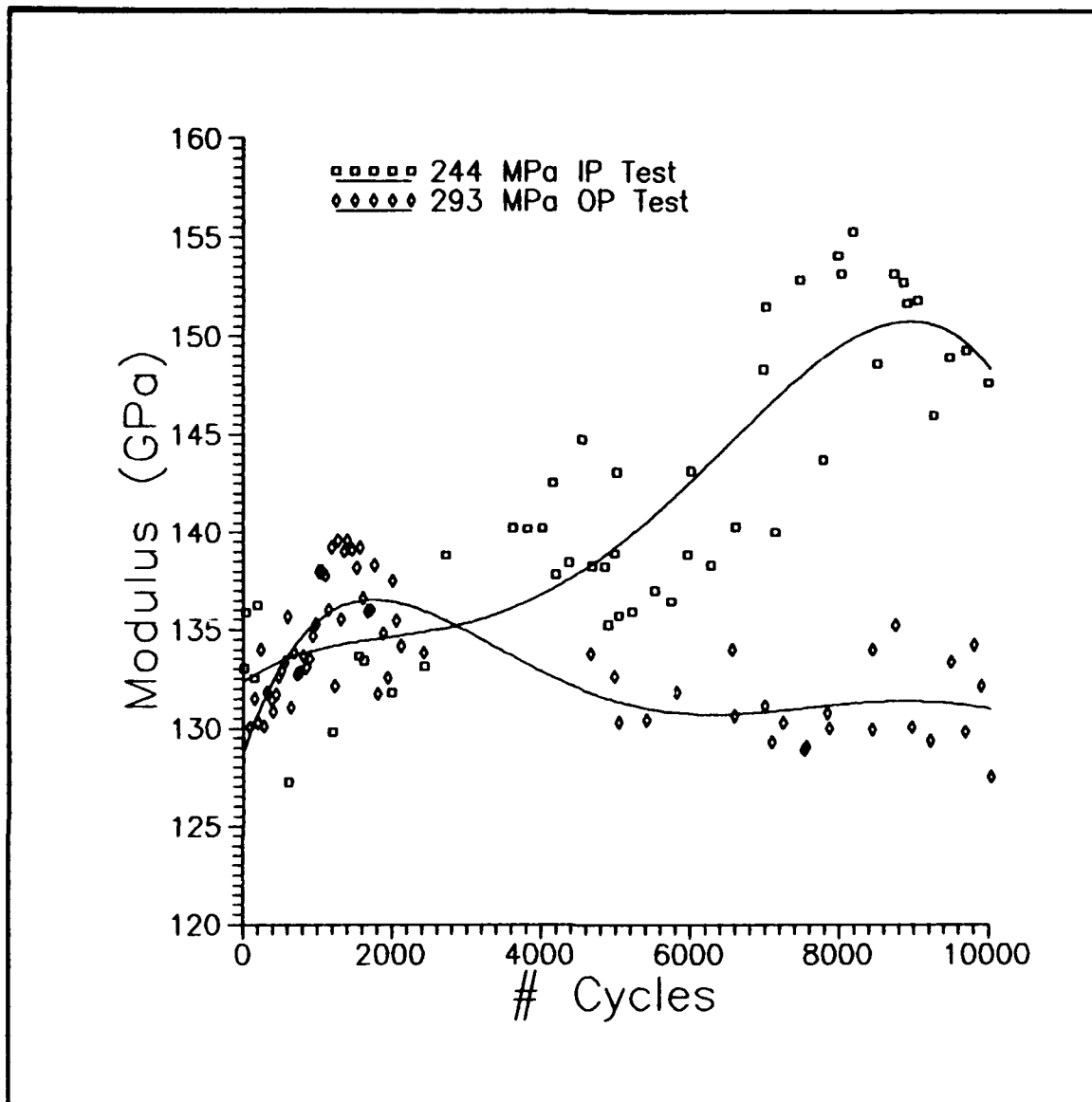


**Figure 77. 50% IP and 60% OP Tests - Modulus Data**

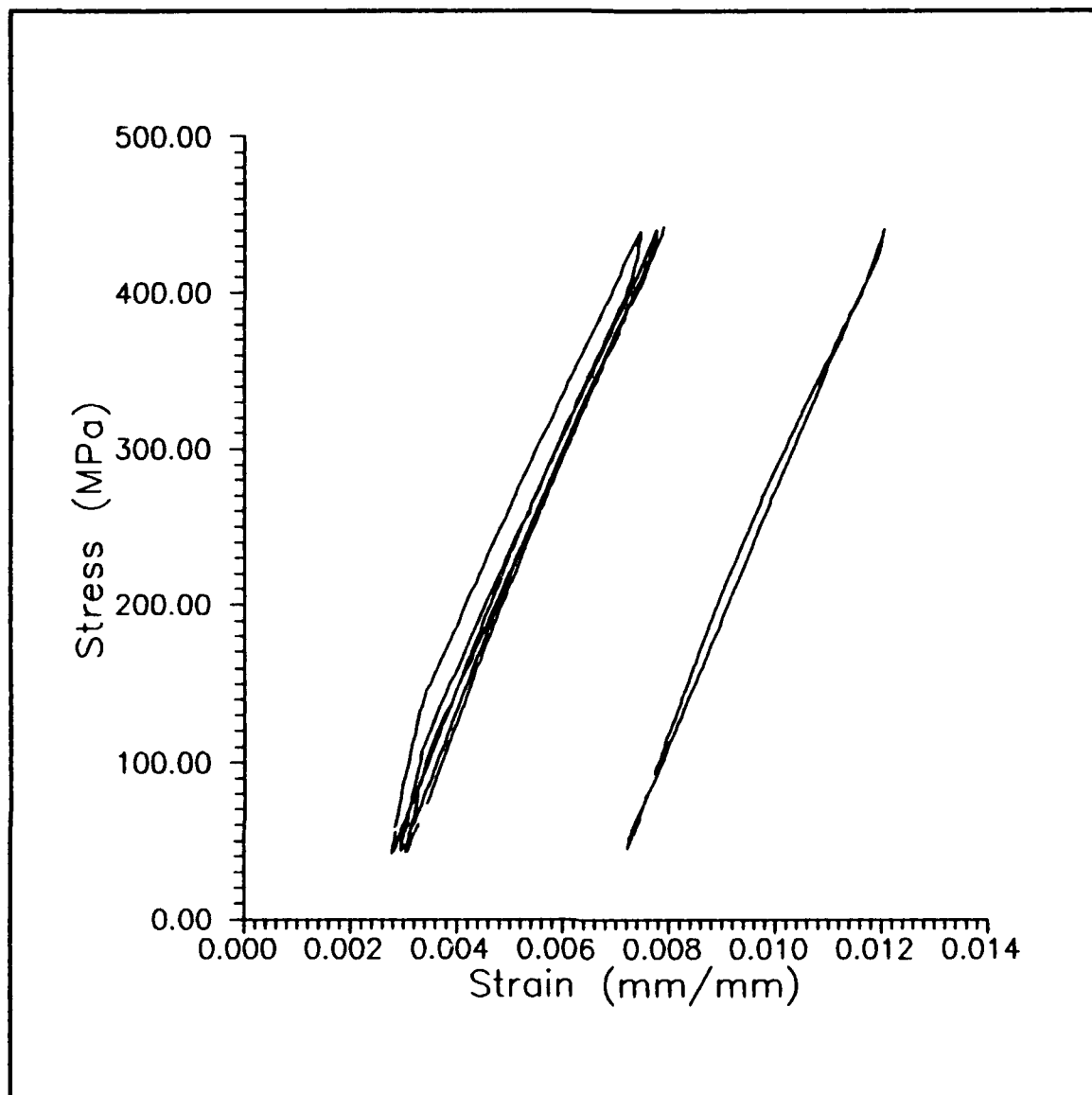


**Figure 78.** 441 MPa I-P Test Strain Progression

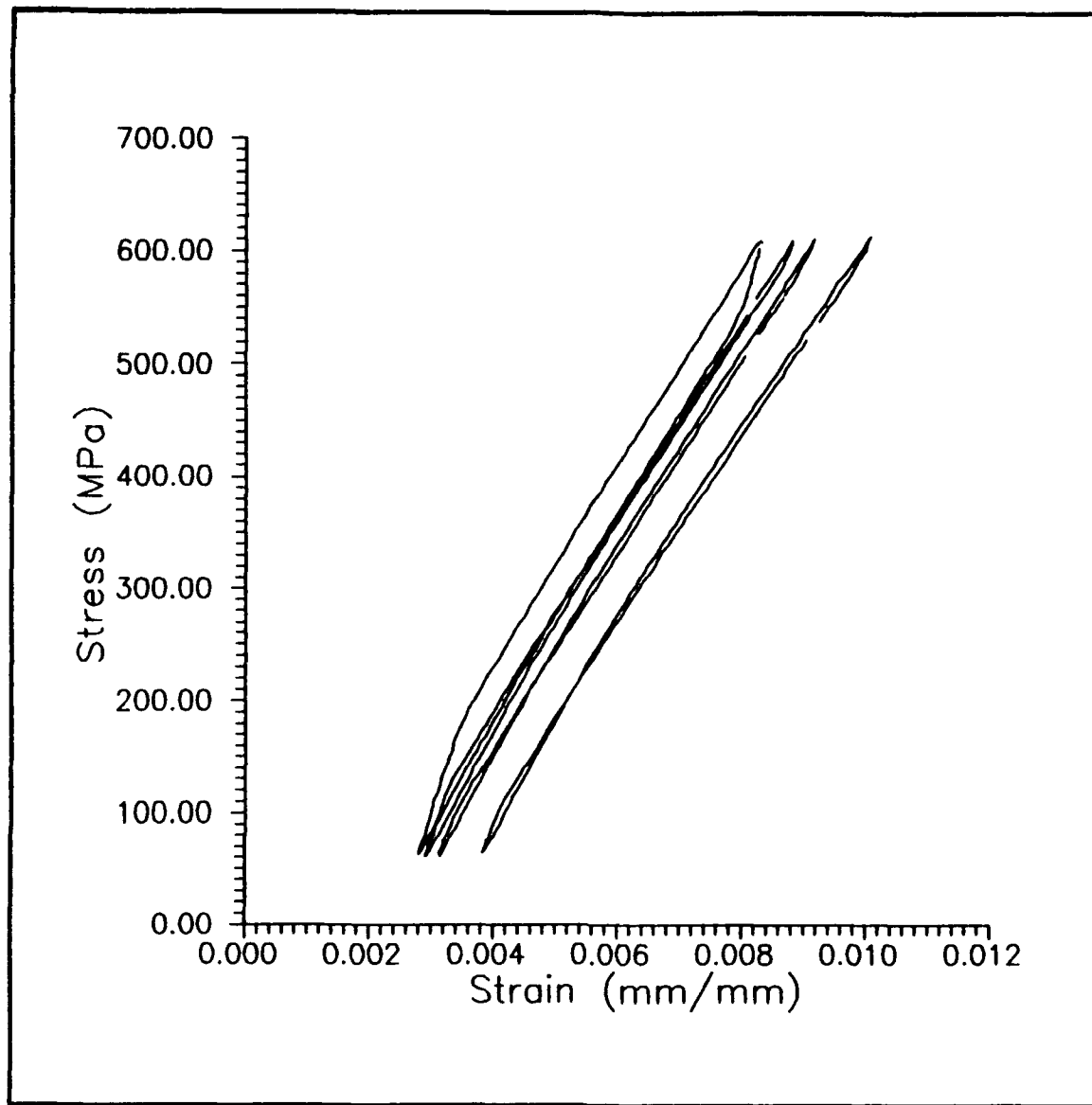
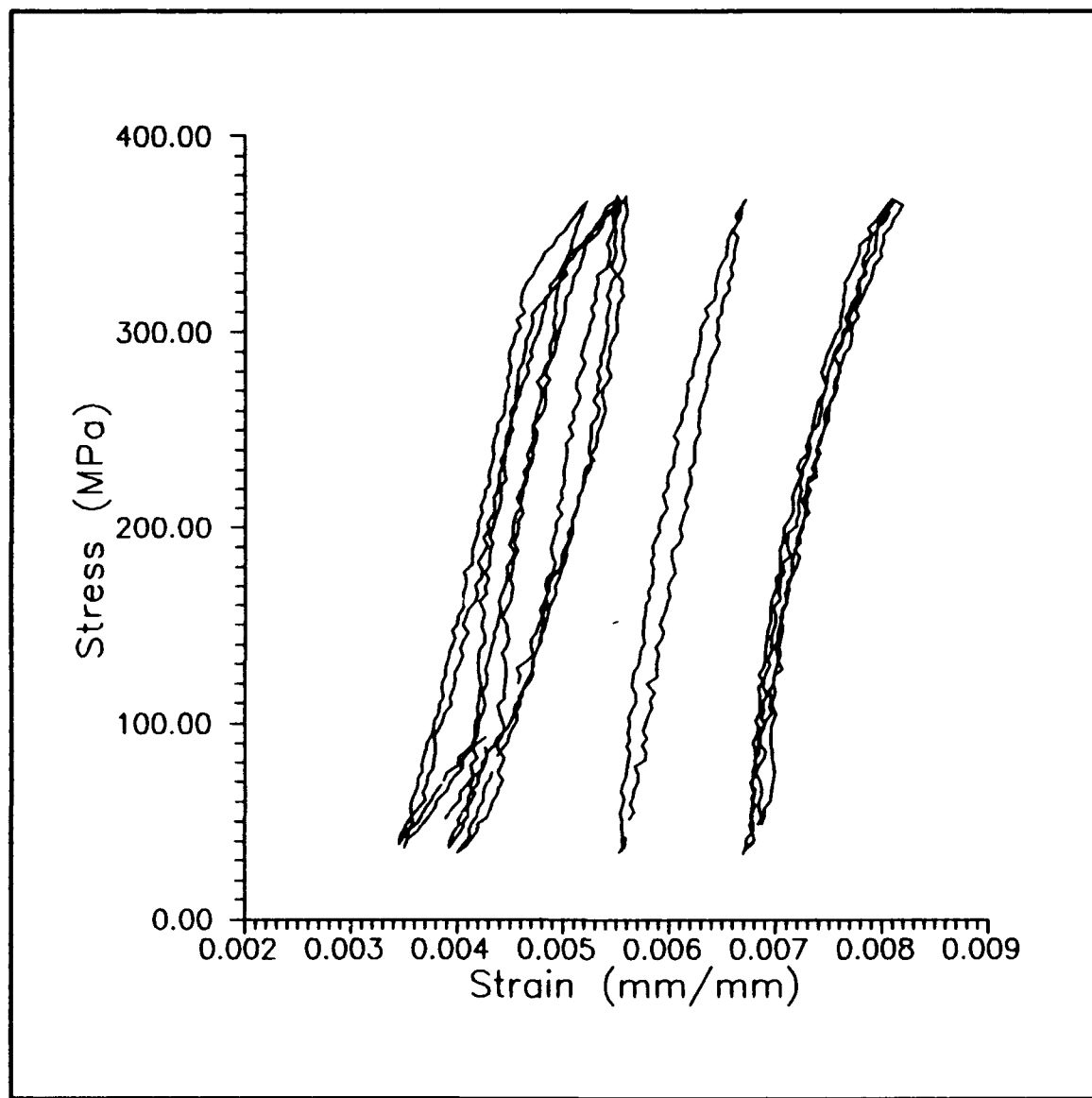
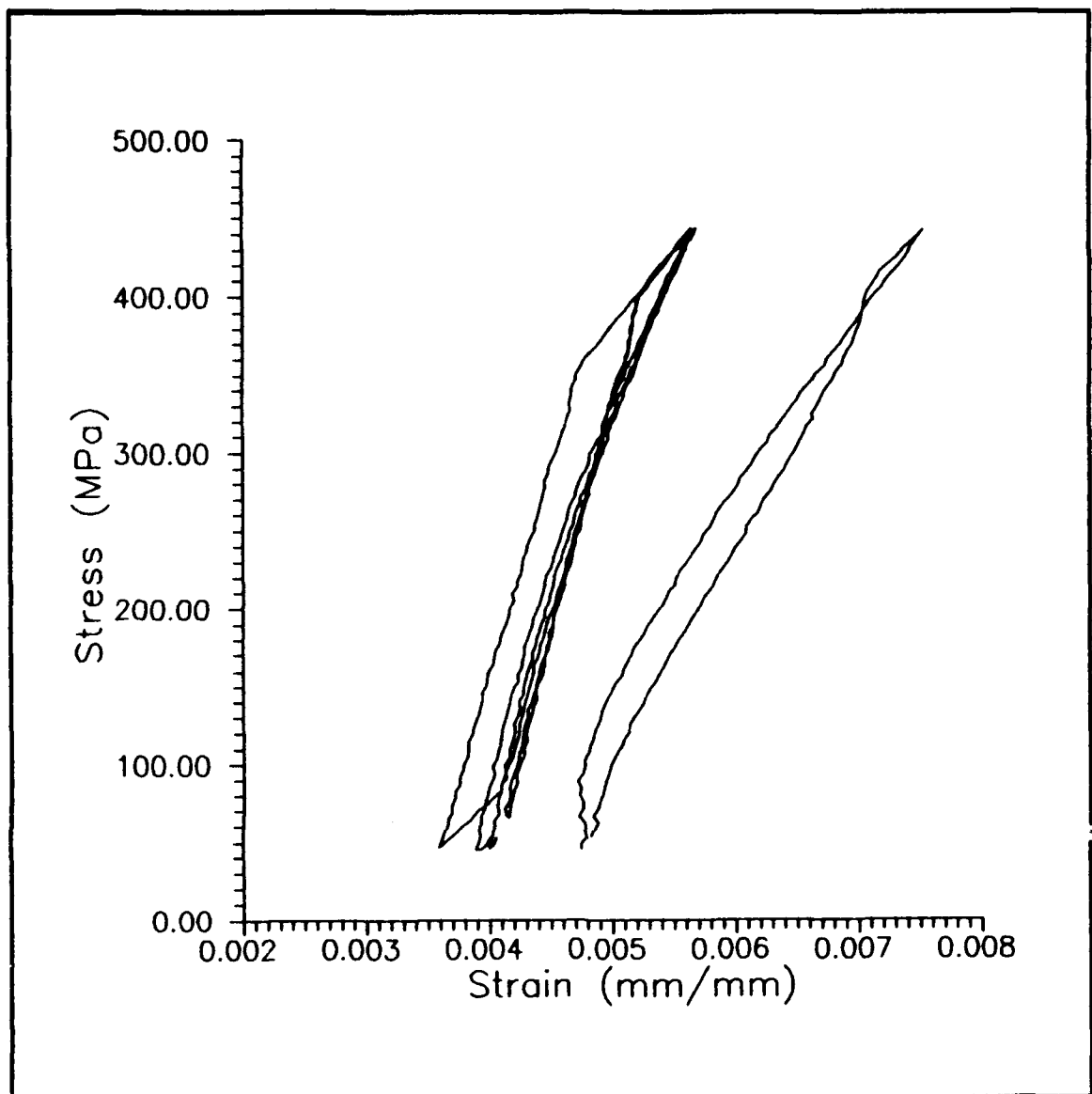


Figure 79. 612 MPa I-P Test Strain Progression



**Figure 80.** 367 MPa O-P Test Strain Progression



**Figure 81. 441 MPa O-P Test Strain Progression**

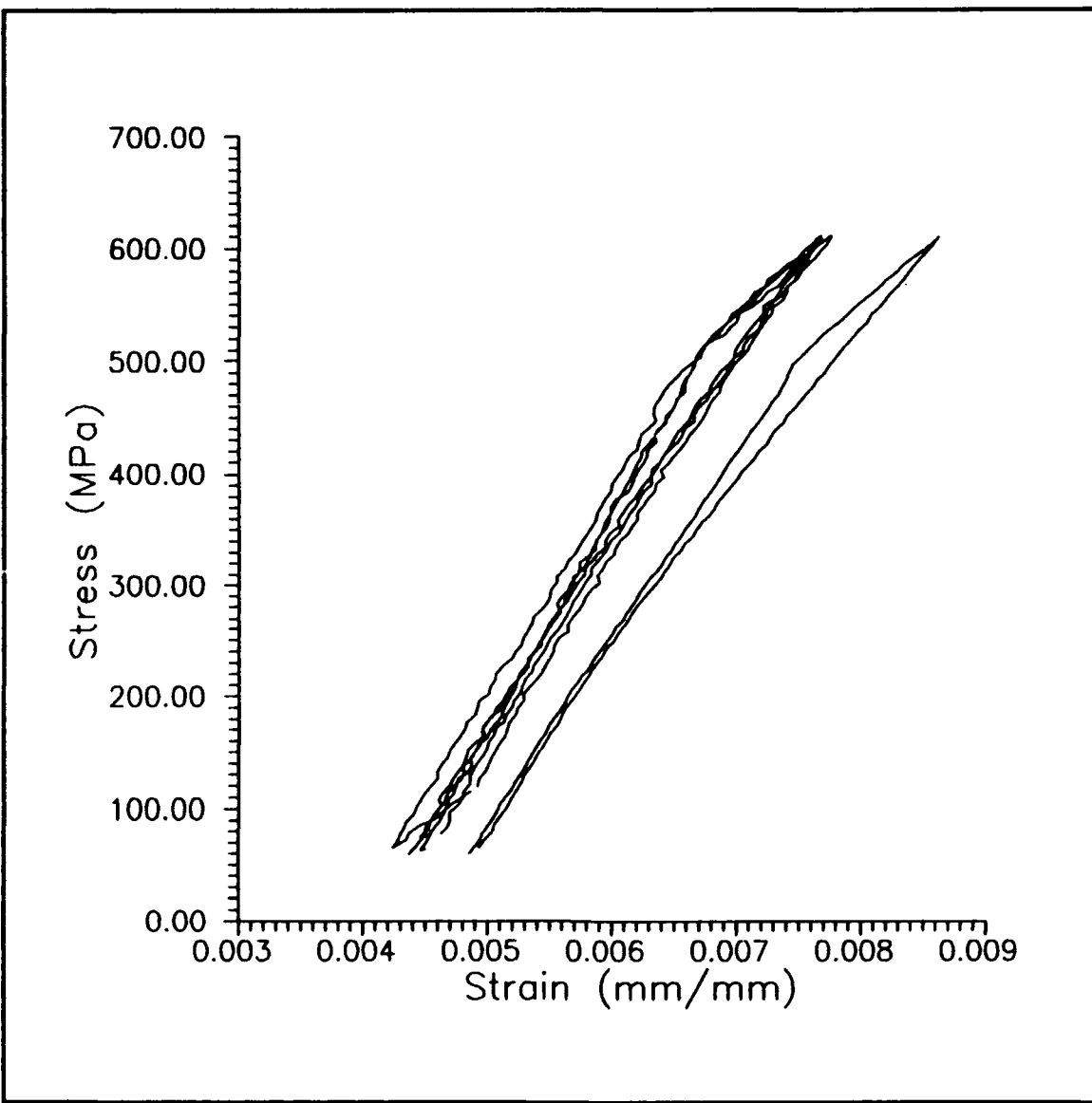


**Figure 82. 612 MPa O-P Test Strain Progression**

## Bibliography

1. Age Hardening of Metals, Kenyon R.L. and Burns R.S., "Aging in Iron and Steel," Cleveland, OH: American Society for Metals, 1940.
2. Beta Titanium Alloys in the 80's, Edited by Boyer, R.R. and Rosenberg, H.W., Warrendale, PA: The Metallurgical Society of AIME, 1984.
3. Broek, David. Elementary Engineering Fracture Mechanics. Netherlands: Martinus Nijhoff Publishers, 1986.
4. Castelli, M.G. and others. "Thermomechanical Testing techniques for High Temperature Composites: TMF Behavior of SiC(SCS<sub>6</sub>)/Ti-15-3," Sverdrup Technology, Brook Park, Ohio/NASA Lewis Research Center, Cleveland, OH, Unpublished.
5. Chamis, C.C. and Hopkins, D.A. "Thermoviscoplastic Nonlinear Constitutive Relationships For Structural Analysis of High Temperature Metal Matrix Composites," NASA TM-87291, November, 1985.
6. Ermer, Capt Paul G. Investigation of the Failure Modes in a Metal Matrix Composite Under Thermal Cycling. MS Thesis, AFIT/GAE/ENY/89D-07. School of Engineering, Air Force Institute of Technology (AU), Wright-Patterson AFB OH, December 1989.
7. Fundamentals of Process Control. Research, Inc., Minneapolis MN, May 1981.
8. Gabb, T. P. and others. "Isothermal and Nonisothermal Fatigue Behavior of a Metal Matrix Composite," Submitted to the Journal of Composite Materials, 1989.
9. Gayda, John Jr. and others. "The Isothermal Fatigue Behavior of a Unidirectional SiC/Ti Composite and the Ti Alloy Matrix," NASA TM-101984, April 1989.
10. Hartman, G. and Nicholas T. "An Enhanced Laser Interferometer for Precise Displacement Measurement", Experimental Techniques, Feb 1987.
11. Heil, Major Michael L. Crack Growth in Alloy 718 Under Thermal-Mechanical Cycling. PhD Dissertation. School of Engineering, Air Force Institute of Technology (AU), Wright-Patterson AFB OH, November 1986.

12. Highsmith, A.L. and others. "Local Stresses in Metal Matrix Composites Subjected to Thermal and Mechanical Loading," Presented at Symposium on Thermal and Mechanical Behavior of Ceramic and Metal Matrix Composites (ASTM), Atlanta, GA, November 7, 1988.
13. High Temperature Materials, Edited by Hehemann R.F. and Ault G.M., New York: John Wiley & Sons, Inc., 1959.
14. Hopkins, D.A. and Chamis, C.C. "A Unique Set of Micromechanics Equations for High Temperature Metal Matrix Composites," NASA TM-87154, November 1985.
15. Johnson, W.S. and others. "Fatigue Testing and Damage Development In Continuous Fiber Reinforced Metal Matrix Composites," NASA TM-100628, 1988.
16. Johnson, W.S. and others. "Mechanical Characterization of Unnotched SCS<sub>6</sub>/Ti-15-3 Metal Matrix Composites at Room Temperature," NASP TM - 1014, April 1988, Presented at the ATSM Symposium, Atlanta, GA., November 1988.
17. Kyno, T. and others. "Effects of Thermal Cycling on Properties of Carbon Fiber/Aluminum Composites," Journal of Engineering Materials and Technology, 110: 89-95 (April 1988).
18. Majumdar, Bhaskar S. and Golam N. Newaz. "Thermo-Mechanical Fatigue Response and Damage in an Angle-Ply Metal Matrix Composite," Battelle Memorial Institute, Columbus, OH. Submitted to The Journal of Engineering Materials and Technology - ASME, October, 1989.
19. Mate Technical Reference Manual. University of Dayton Research Institute, Dayton, OH.
20. Metal Matrix Composite Analyzer METCAN Version 2.0 User's Guide. NASA Lewis Research Center, Cleveland OH, September 1988.
21. Mechanical Metallurgy, Edited by Meyers, M.A. and Chawla, K.K., New Jersey: Prentice-Hall, Inc., 1984.
22. Micricon Control PID Adjustments, Research Inc., Minneapolis MN, 1981.

23. Micricon User's Manual. Research Inc., Minneapolis, MN, 1986.
24. Model 5305 Parabolic Strip Heater Rev B. Research Inc., Minneapolis, MN, December 1985.
25. MSC/NASTRAN Version 65C User's Manual, Aug 1987.
26. Naik, R.A. and others. "Effect of a High Temperature Cycle on the Mechanical Properties of Silicon Carbide/Titanium Metal Matrix Composites," Unpublished.
27. Pernot, J.J. Thermal-Mechanical Fatigue Testing of a Titanium-Aluminide Alloy. Master's Thesis, AFIT/GAE/AA/87D-18. Air Force Institute of Technology (AU), Wright-Patterson AFB, December 1987.
28. Pollack, W.D. and Johnson, W.S. "Characterization of Unnotched SCS-6/Ti-15-3 Metal Matrix Composites at 650°C," NASA T-M 102699, September 1990.
29. Portner, Capt B. Investigation of Fatigue Damage Mechanisms in a Metal Matrix Composite Under Elevated Temperature. MS Thesis, AFIT/GAE/ENY/90D-20. School of Engineering, Air Force Institute of Technology (AU), Wright-Patterson AFB OH, December 1990.
30. Probabilistic Models of Cumulative Damage. Edited by Bogdanoff, J. and Kozin, F., New York: John Wiley & Sons, 1985.
31. Reifsnider, K.L. and others. "Damage Mechanics and NDE of Composite Laminates," Mechanics of Composite Materials, Recent Advances, Z. Hashin and C.T. Herakovich, eds., Pergamon, New York, 1983.
32. Rogacki, J. and Tuttle M. "Thermoviscoplastic Behavior of SCS<sub>6</sub>/Ti Metal Matrix Composites," Department of Mechanical Engineering, FU-10, University of Washington.
33. Series 632 High Temperature Extensometers. MTS Systems Corporation, Minneapolis, MN, Undated.
34. SDRC-IDEAS Level 4 (Integrated Design Engineering Analysis Software) User's Guide, 1988.

Vita

**Captain Joel J. Schubbe**

In 1982 he graduated from R. Nelson Snider High School in Fort Wayne, Indiana and received an appointment to the United States Air Force Academy in Colorado Springs, Colorado. He received the degree of Bachelor of Science in Engineering Sciences and his commission in the USAF in May 1986. He then served as an Armament Systems Analyst at the Air Force Foreign Technology Division, Wright-Patterson AFB, OH until entering the School of Engineering, Air Force Institute of Technology, in May 1989.

# REPORT DOCUMENTATION PAGE

Form Approved  
OMB No. 0704-0188

Public report burden (in hours) is estimated to be 1.0 hour per report. Including the time for reviewing instructions, searching existing data sources, gathering and maintaining the data needed, and completing and reviewing the collection of information. Pending comments regarding this burden estimate from the public, the burden estimate is 1.0 hour per report. This report burden estimate is based on the following: (a) 1 hour for reading instructions, (b) 0.5 hours for searching existing data sources, (c) 0.5 hours for gathering and maintaining the data needed, and (d) 0.5 hours for completing and reviewing the collection of information. Pending comments regarding this burden estimate from the public, the burden estimate is 1.0 hour per report. This report burden estimate is based on the following: (a) 1 hour for reading instructions, (b) 0.5 hours for searching existing data sources, (c) 0.5 hours for gathering and maintaining the data needed, and (d) 0.5 hours for completing and reviewing the collection of information.

1. AGENCY USE ONLY (Leave Blank)	2. REPORT DATE	3. REPORT TYPE AND DATES COVERED
	DEC 90	Master's Thesis
4. TITLE AND SUBTITLE <b>Investigation of Damage Mechanisms in a Cross-Ply Metal Matrix Composite under Thermo-Mechanical Loading</b>		5. FUNDING NUMBERS
6. AUTHOR(S) Joel J. Schubbe, Captain, USAF		
7. PERFORMING ORGANIZATION NAME(S) AND ADDRESS(ES) Air Force Institute of Technology, WPAFB OH 45433-6583		8. PERFORMING ORGANIZATION REPORT NUMBER AFIT/GAE/ENY/90D-26
9. SPONSORING MONITORING AGENCY NAME(S) AND ADDRESS(ES) Ted Fecke WRDC/POTC Wright-Patterson AFB OH 45433		10. SPONSORING MONITORING AGENCY REPORT NUMBER
11. SUPPLEMENTARY NOTES		
12a. DISTRIBUTION AVAILABILITY STATEMENT <b>APPROVED FOR PUBLIC RELEASE; DISTRIBUTION UNLIMITED</b>		12b. DISTRIBUTION CODE
13. ABSTRACT (Maximum 200 words) <b>Metal matrix composites (MMCs) are rapidly becoming strong candidates for high temperature and high stiffness structural applications such as the Advanced Tactical Fighter (ATF). This study systematically investigated the failure modes and associated damage in a cross-ply, [0/90]<sub>2s</sub> SCS6/Ti-15-3 metal matrix composite under in-phase and out-of-phase thermomechanical fatigue. Initiation and progression of fatigue damage were recorded and correlated to changes in Young's Modulus of the composite material. Experimental results show an internal stabilization of reaction zone size but degradation and separation from constituent materials under extended cyclic thermal loading. Critical to damage were transverse cracks initiating in the 90° plies, growing and coalescing from fiber/matrix interfaces internal to the specimen, progressing outward through the 0° plies before failure. Maximum mechanical strain at failure was determined to be approximately 0.0075 mm/mm. A correlation was made relating maximum matrix stress to failure life, resulting in a fatigue threshold limit of 280 MPa. An attempt was made to correlate the degradation in Young's Modulus (Damage=1-E/E<sub>0</sub>) with the applied life cycles from different TMF tests.</b>		
14. SUBJECT TERMS <b>Metal Matrix Composites, Fiber-Reinforced Composites, SCS6/Ti-15-3, Silicon Carbide, Titanium, Thermomechanical, Fatigue, Heat Resistant Materials, Composite Materials</b>		15. NUMBER OF PAGES 161
16. PRICE CODE		
17. SECURITY CLASSIFICATION OF REPORT <b>Unclassified</b>	18. SECURITY CLASSIFICATION OF THIS PAGE <b>Unclassified</b>	19. SECURITY CLASSIFICATION OF ABSTRACT <b>Unclassified</b>
		20. LIMITATION OF ABSTRACT <b>III</b>

## GENERAL INSTRUCTIONS FOR COMPLETING SF 298

The Report Documentation Page (RDP) is used in announcing and cataloging reports. It is important that this information be consistent with the rest of the report, particularly the cover and title page. Instructions for filling in each block of the form follow. It is important to **stay within the lines to meet optical scanning requirements.**

**Block 1. Agency Use Only (Leave Blank)**

**Block 2. Report Date.** Full publication date including day, month, and year, if available (e.g. 1 Jan 88). Must cite at least the year.

**Block 3. Type of Report and Dates Covered.**

State whether report is interim, final, etc. If applicable, enter inclusive report dates (e.g. 10 Jun 87 - 30 Jun 88).

**Block 4. Title and Subtitle.** A title is taken from the part of the report that provides the most meaningful and complete information. When a report is prepared in more than one volume, repeat the primary title, add volume number, and include subtitle for the specific volume. On classified documents enter the title classification in parentheses.

**Block 5. Funding Numbers.** To include contract and grant numbers; may include program element number(s), project number(s), task number(s), and work unit number(s). Use the following labels:

C - Contract	PR - Project
G - Grant	TA - Task
PE - Program Element	WU - Work Unit
	Accession No.

**Block 6. Author(s).** Name(s) of person(s) responsible for writing the report, performing the research, or credited with the content of the report. If editor or compiler, this should follow the name(s).

**Block 7. Performing Organization Name(s) and Address(es).** Self-explanatory.

**Block 8. Performing Organization Report Number.** Enter the unique alphanumeric report number(s) assigned by the organization performing the report.

**Block 9. Sponsoring/Monitoring Agency Name(s) and Address(es).** Self-explanatory.

**Block 10. Sponsoring/Monitoring Agency Report Number.** (If known)

**Block 11. Supplementary Notes.** Enter information not included elsewhere such as: Prepared in cooperation with...; Trans. of ..., To be published in .... When a report is revised, include a statement whether the new report supersedes or supplements the older report.

**Block 12a. Distribution/Availability Statement.**

Denote public availability or limitation. Cite any availability to the public. Enter additional limitations or special markings in all capitals (e.g. NOFORN, REL, ITAR)

DOD - See DoDD 5230.24, "Distribution Statements on Technical Documents."

DOE - See authorities

NASA - See Handbook NHB 2200.2.

NTIS - Leave blank.

**Block 12b. Distribution Code.**

DOD - DOD - Leave blank

DOE - DOE - Enter DOE distribution categories from the Standard Distribution for Unclassified Scientific and Technical Reports

NASA - NASA - Leave blank

NTIS - NTIS - Leave blank.

**Block 13. Abstract.** Include a brief (Maximum 200 words) factual summary of the most significant information contained in the report.

**Block 14. Subject Terms.** Keywords or phrases identifying major subjects in the report.

**Block 15. Number of Pages.** Enter the total number of pages.

**Block 16. Price Code.** Enter appropriate price code (NTIS only).

**Blocks 17. - 19. Security Classifications.**

Self-explanatory. Enter U.S. Security Classification in accordance with U.S. Security Regulations (i.e., UNCLASSIFIED). If form contains classified information, stamp classification on the top and bottom of the page.

**Block 20. Limitation of Abstract.** This block must be completed to assign a limitation to the abstract. Enter either UL (unlimited) or SAR (same as report). An entry in this block is necessary if the abstract is to be limited. If blank, the abstract is assumed to be unlimited.